國 立 交 通 大 學

機械工程學系

碩士論文

改善 EWOD 元件於產生奈升級液滴之研究

Development of Creating Nano-Liter Droplets using Novel Patterns of EWOD

研究生：許耀文

指導教授：陳俊勳　教授

中 華 民 國 九 十 六 年 六 月

改善 EWOD 元件於產生奈升級液滴之研究

Development of creating nano-liter droplets using novel patterns of EWOD

研究生　：許耀文　　Student：Yao-Wen Hsu

指導教授：陳俊勳　　Advisor：Chiun-Hsun Chen

國 立 交 通 大 學

機 械 工 程 學 系

碩 士 論 文

A Thesis

Submitted to Department of Mechanical Engineering

College of Engineering

National Chiao Tung University

In Partial Fulfiillment of the Requirements

For the Degree of

Master of Science

In Mechanical Engineering

June 2007

Hsinchu, Taiwan, Republic of China

中 華 民 國 九 十 六 年 六 月

改善 EWOD 元件於產生奈升級液滴之研究

學 生：許 耀 文　　指導教授：陳俊勳

國立交通大學機械工程學系

摘要

電濕潤是藉由氣液介面的表面張力影響來液珠，而使液珠移動，其中優點包含，製造過程簡單、可控制定量的液珠、價格較低可取代微制動器與微混合器等。 本研究先簡化質量守恆方程式與動來守恒方程式來當作電濕潤的模擬模式，並利用商用軟體 CFD-ACE+來模擬液珠在電濕潤的情況。 而電濕潤元件的組成包含，8 個 0.48mm X 0.5mm 的底部電極（金/鉻）、介電層厚度為 3000Å 的氮化矽、厚度為 1000 Å 的鐵福龍層和旋塗厚度 1000 Å 鐵福龍的氧化銦錫玻璃為上電極。 其實驗量測系統包含，微流體元件、微處理器、控制電路、LCD 顯示器、4X4 小鍵盤、電源供應器和功率放大器。 幾種不同設計的電極形狀會先在模擬情況下互相比較，總共有 16 組，將常用的正方形電極改成指插電極，並改變流道高度(20 μm 、35 μm 和 70 μm)、指插電極角的數目與指插電極角的寬度，來探討液珠的壓力與平均速度之變化，其中，液珠的內壓與大氣壓的壓差會隨著流道高度的縮小而變大的情形亦被模擬，也於流道高度為 35 μm 的模擬，其結果可以發現指插電極所產生的壓差(240Pa~600Pa)都大於正方形電極(192Pa)。 由於驅動壓力大，有助於液珠的移動與分離，進而抽取出

奈升液珠，以便於在生醫上的應用。 最後根據模擬的預測，選取 3 種的電極設計，並利用微機電技術製造元件來證明模擬的趨勢，其中選取的電極分別為正方形電極,指插電極角數目為2323的排列與5656的排列順序。對於液珠在流道高度為 20 μm 的移動情況下分別作平均速度的比對，其中，在實驗上液珠的平均速度對於排列順序為 2323 的指插電極為 11.36 mm/s，而模擬的平均速度為 13.291 mm/s。 對於電極排列順序為 5656 在實驗與模擬的平均速度分別為 11.07 mm/s 和 11.542 mm/s。 而正方形分別為 10.49 mm/s 和 9.614 mm/s。 最後，在實驗上於應用電壓為 100V 的交流電下，也成功產生出 2.9～8.5nl 的奈升液珠。

關鍵字：電濕潤，指插電極，CFD-ACE+

Development of creating nano-liter droplets using novel patterns of EWOD

Student: Yao-Wen Hsu Advisor: Prof. Chiun-Hsun Chen

Institute of Mechanical Engineering

National Chiao Tung University

ABSTRACT

Electrowetting on dielectric (EWOD) moving fluid driven by surface tension offers some advantages, including simplicity of fabrication, control of minute volumes, low cost, substitution for micro-mixers and others. In this study, The EWOD model based on the reduced forms of the mass and momentum conservation equations is adopted to simulate the fluid dynamics of droplet, and its movement is simulated by a commercial software CFD-ACE+. The EWOD device consists of eight 0.5 x 0.48 mm bottom electrodes (Au/Cr), a dielectric layer of 3000 Å nitride, a Teflon layer of 1000 Å and a piece of indium tin oxide (ITO)-coated glass with 1000 Å Teflon as the top electrode. The measurement system consists of the microfluidic device, microprocessor, electric circuits, LCD module, keypad, power supply and power amplifier. Several simulations using different electrode designs were carried out in advance. The interdigitated electrodes were used to replace common-used square ones to investigate the changes of droplet pressure difference. The varying parameters include the channel height (20 μm, 35 μm and 70 μm), and the number and width of extended rectangle of interdigitated

electrodes. Sixteen simulations were carried out in this thesis. Under the same shape of interdigitated electrode, the phenomenon of increasing pressure difference due to decrease of channel height can be simulated. For simulations of 35 μm-channel height, the ones with interdigitated electrode can generate the larger pressure differences (310 Pa~680 Pa) than that of square electrode (300 Pa). The increment of pressure difference is helpful to move and cut droplets, and further to create a nano-liter droplet, which can be applied in biomedical applications. The following optimal designs of electrode were according to the best simulation results. Then, they were manufactured by MEMS processes and their performances were certified by EWOD device. Furthermore, the predictions of simulations for droplet of moving, in which the channel height was 20 μm were compared with experimental results for three designs of electrodes including square electrodes and interdigitated electrodes with arrangements of 2323 and 5656 extended rectangles. It is found that the mean velocity of droplet for interdigitated electrode (2323) was 11.36 mm/s, whereas the corresponding prediction was 13.291 mm/s. For 5656 arrangement, the mean experimental and numerical velocities were 11.07 and 11.542 mm/s, respectively. As to square electrode, they were 10.49 and 9.614 mm/s, separately. Finally, the 2.9nl~8.5nl droplets are successfully created at 100 V_{Ac} experimentally.

Keyword: CFD-ACE+, Electrowetting on dielectric (EWOD), interdigitated electrode

ACKNOWLEDGEMENT

回看兩年碩士生活自覺得有許多成長，其中最感謝陳俊勳老師，讓我有機會在成大電機系張凌昇老師的研究室學習不同的領域，並能在求學期間將所遇到的問題能一一克服，對於未來競爭力上學生覺得受益良多，在此對兩位老師獻上無限的感激與敬意。

其中在研究過程中，要特別感謝交大的文耀、國華、關恕、嘉鴻、靜慈、遠達、彥成、等學長姐在碩班生活上的指導，還有、迪翰、建宏、炳坤、等同學的幫忙與鼓勵。而在成大生涯中也特別感謝宜良、垣杰、敏峰、智淵、偉雄、浩凱、浩君、俊宏、信宏、俊慶、威宇、南江、鎵豪等人在台南的幫忙，讓我在成大做研究及生活上更加得心應手。當然也要特別感謝我的好朋友振華在成大的照顧。

最後感謝我的家人在我求學過程中的一路陪伴與鼓勵，謝謝。

CONTENTS

LIST OF TABLES

LIST OF FIRGURES

NOMENCLATURE

γ_0	Surface tension of solid-liquid interface without external potential
γ	Surface tension of solid-liquid interface with external potential
c	Capacitance per unit area
R	Radius of ideal sphere of droplet
V	Potential
E_{sys}	Total energy of the system
E_{int}	Interfacial potential energy of the droplet
E_{de}	Energy stored in the solid dielectric layer between the liquid and the counter electrode
E_{vs}	Potential energy
γ_{SL}	Interfacial tension between the solid-liquid
γ_{SV}	Interfacial tension between the solid-vapor
γ_{LV}	Interfacial tension between the liquid-vapor
A_{SL}	Area of the droplet on the solid surface
A_{LV}	Liquid-vapor interface area
$\mathcal{V}$	Volume of the dielectric layer
$\vec{E}$	Electric field
$\vec{D}$	Charge displacement
ε_0	permittivity of vacuum
ε_r	Dielectric constant of the solid

d	Dielectrics of thickness
θ_0	Contact angle without external voltage
θ	Contact angle with external voltage
C	Capacitance
Q	Charges in the capacitor.
C_{Top}	Capacitor on the top plate
C_{Botton}	Capacitor on the bottom plate
Δp	Pressure difference across an interface
P_a	Pressure of atmosphere
D	Distance of channel gap
R_1	Radius of curvature of the droplet curved surface
x	X direction
y	Y direction
z	Z direction
$\vec{V}$	Velocity vector
p	Pressure
ρ	Fluid density
μ	Viscosity coefficient
$\vec{F}^{\sigma}$	Surface tension on liquid-gas interface
$\rho\vec{g}$	Fluidic gravity
k	Mean interface curvature

σ Surface tension value

$\hat{n}$ Unit vector on interface

CHAPTER 1
INTRODUCTION

1.1 Motivation and background

As micro-electro-mechanical-systems (MEMS) technology requirement increases, microfluidics has become possible to be controlled. In the last several decades, there has been a tremendous of interests in the movement of bulk fluidic mass and in the path control of the embedded objects of interest (e.g., cell, protein, etc.) in the flow. The so-called biochips, which integrate microfluidic and microsensor devices, have potential application in chemical analysis, drug delivery, protein analysis, gene expression, biochemical analysis, detection, and so on [1]. Traditionally, chemical analyses have been performed in central laboratories by skilled personnel and specialized equipments. However, the trend is to push chemical analyses closer to ”customer.” To let it come true, handy and portable analytical equipments, such as biochips, are needed [2]. The major advantages of biochip are that it can minimize reagent consumption, reduce analysis time, increase sensitivity and improve accuracy. Therefore, biochip is currently one of the microsystem engineering fields with the largest market opportunities.

The developed biochips basically can be divided into two categories; one is the microarray chip and the other the lab-on-a-chip. Microarray chip has ripened into maturity, on the other hand, lab-on-a-chip is becoming the potential research topic in the near future. Lab-on-a-chip—well-known as micro-processor chip, microarray chip and micro total analysis system—is implied by the name that achieves biochemical analyses worked in a general

laboratory by a chip. It can push liquid in the order of microlilter or nanolilter into a chip, which is covered with micro fluidic channels fabricated by the semiconductor processing technology, and then there is the same response of liquid in the designed chip as required in lab.

During the last several decades, many microsystems have been investigated and developed to control liquid movement under the microscale. In those microfluidic systems, there exist many methods, such as electrowetting, electrostatics, electrophoretics, electroosmotics and thermopneumatics, to drive liquid. The traditional one has been using microfluidic channel to control continuous-flow. Until very recently, the actuation based on surface tension becomes a dominant mechanism on the microscale device. Fig. 1-1 illustrates the scaling of two forces for weight and surface tension, respectively [3]. The effect of surface tension is greater than that of weight when the system dimension is below the sub-microscale. Actuation of the droplet based on the change in surface tension can eliminate the need for moving parts and can be performed by programmed electric signals rather than physical structures. Droplet-based microfluidic systems differ from continuous flow ones because they manipulate discrete droplets rather than continuous flow. The electrical control of wettability of liquids on a dielectric material, called electrowetting- on-dielectric (EWOD), has drawn much attention as a promising microfluidic actuation mechanism in micro total analysis systems (μTAS). EWOD has an excellent reversibility and it possesses a number of advantages over continuous-flow systems, such as controlling each droplet independently, minimizing the usage of fluids, reducing the mixing time and having the comparable performance with the traditional methods. Due to the advantages mentioned above, EWOD technology has a great potential industrial market in the future.

1.2 Literature review

The mechanism of EWOD is that when an electric voltage is applied to the droplet, the electric charge changes free energy on the dielectric surface, inducing a change in wettability of the surface and resulting in the change in the droplet contact angle. The concept of electrowetting (EW) originates from the Lippman, who made an experiment about electrocapillarity in 1875 [4]. He recognized that the externally added electrostatic charge can change the capillary forces at an interface. Fair et al. [5] firstly proposed that using EW changes the liquid-to-liquid surface tension to move liquid metal (electrolyte) in the mercury and solution in silicon oil (Fig.1-2-a). Kim [5] was successfully to drive the solution in air by changing liquid-solid surface tension, as shown in Fig.1-2-b.

The continuous electrowetting (CEW) was developed by Fair et al. [5-6]. The electrowetting microactuator is presented schematically in Fig.1-3. A droplet of polarization and conductive liquid was sandwiched between two sets of planar electrodes. The upper plate consisted of a single continuous ground electrode, while the bottom one consisted of an array of independently addressable control electrodes. The control electrodes were then coated with 7000 Å of Parylene C followed by approximately 2000 Å of Teflon AF 1600. Both electrode surfaces were covered by a thin layer of hydrophobic insulation. Droplets of 100 mM KCl solution were successfully transferred between these two electrodes at the voltages of 40–80 V. Repeatable transports of droplets at electrode switching rates of up to 20 Hz with the averaged velocities of 30 mm/s were demonstrated.

EW and EWOD are made to use extra voltage to change liquid-solid

surface tension, a main driving force. As shown in Fig.1-4 [7], by turning electrodes on and off in prescribed sequences, it was possible to induce droplets to move to specific locations. By switching on the voltage at an electrode adjacent to the droplet, the surface tension was lowered locally, causing the droplet to move to the right. It returned to its original shape when the potential was switched off. The change of contact angle could be obtained from surface tension. It is easier to drive droplet, because the more contact angle changes, the more surface tension changes. Figures 1-5 and 1-6 illustrate that the contact angle of droplet is changed by the external voltage [7].

The contact angle decreases as the applied potential increases until the contact angle is saturated, and then it is called contact angle saturation, which the angle can no longer increase even by applying higher voltage. In order to understand the phenomenon of contact angle and contact angle saturation on the different material with different samples, it is completely relied on the design and control of microfluidic system. The reason of saturation at DC voltage and AC voltage are not exactly the same. For the AC signal, it creates ionization between sharp-pointed area of droplet and air, and then the droplet is surrounded by ions in a form of a hydrophilic ring, which can destroy the hydrophobia of dielectric layer. For the DC signal, the charges are trapped in the dielectric layer, after that they form the hydrophilic ring to destroy the hydrophobia of dielectric layer and make the electrowetting irreversible [8]. The electrowetting irreversibility can be improved by suitable dielectric material. Besides saturated phenomenon, it has a little difference to the change of contact angle as increasing and decreasing voltage, which is called hysteresis. These shortcomings can be improved better by applying suitable dielectric material and MEMS process.

In the microfluidic system, the control of digital microfluidics comprises four basic operations: (a) creating, (b) transporting, (c) merging and (d) cutting liquid droplets. The pioneer study was done by Kim et al. [9]. In addition to the four operations mentioned above, they designed the NxM grids, as shown in Figs.1-7 and 1-8, that various kinds of products can be produced in the NxM channels by the reservoir of X-direction and Y-direction.

It is often to see an experiment about the concentration control and the separation of cells, molecules and particles. Kim et al. [10] accomplished to separate two types of particle by property of electrophoresis and EWOD control, as shown in Fig. 1-9. The procedure consisted of four steps. The first one, a droplet containing mixed particles was placed between two parallel plates (Fig.1-9-a). The second one, separated (isolate) particles by electrophoresis within a droplet (Fig.1-9-b). An electric field was applied between two exposed electrodes on the top plate to isolate one type of particles on the left side and the other on the right side. The third one, cut the droplet by EWOD actuation after the particles were separated (Fig.1-9-c). The detailed design rules, mechanisms and experimental verifications for the cutting process of droplets were reported. A smaller channel height, a larger droplet size and a larger change in the contact angle enhance the necking of the droplet to help the completion of the cutting process. The last one, transported the produced droplets by EWOD to other locations for the next microfluidic operation (Fig. 1-9-d). To improve the precision of separation, multiple droplets with the same particle type can be re-joined and may go through further separation in the next stage. If there is only single type of particles in a droplet, a similar procedure can be used to control particle concentration as depicted in Fig.1-10.

The work of Fair et al. [11] was to determine the glucose concentration.

It was judged the percentage of glucose concentration with the changes of reagent colors detected by optics instrument, as illustrated in Figs.1-11 and 1-12. They found that the measurement of glucose concentration can be finished in less than one minute.

H.Ren et al. [12] was successful in producing droplet of nano-liter in silicon oil by using auto-control system and AC voltage, as shown in Fig.1-13.

Chatterjee et al. [13] firstly reported that organic solvents, aqueous surfactants and ionic liquids can be manipulated in air in EWOD. The method of actuation is to input AC with various frequencies to drive different liquids, as shown in Fig.1-14.

From the literatures given above, techniques for digital microfluidic devices tend to be mature, after that, it can be applied to bio-samples delivery and cell analyses in the near future. Of course, it is expected to reduce the amount of samples used, analyzing time and prime cost.

1.3 Scope of this study

In this laboratory, a method was developed to simulate EWOD phenomenon. The pictures obtained from the simulation were compared to experimental photos, as shown in Fig. 1-15, in which the applied voltage was 40V, dielectric thickness (nitride) $3000\,\mathring{A}$, channel height $70\mu m$, length of electrode $2mm$ and volume of droplet $0.3\mu l$. It can be seen that the results of simulation and experiment agree well, indicating that all of the simulation parameters are verified, and these can be used to simulate and design the new electrodes [14, 15].

The purpose of this study is to generate a nano-liter droplet by EWOD device. The micro-liter for a volume of cell is still too big if it wants to catch

cells and to analyze them. For cells in micro-liter liquid, the concentration of liquid (extracellular space) will be changed by its metabolism, however, the changed concentration is not obvious in micro-liter. If want to measure the concentration of liquid, it needs a high sensitive instrument. However, if the volume of droplet can be as small as possible, then, the changed concentration can be measured easily. Due to this reason, it needs to limit the range of cell movement and to be able to create nano-liter droplet. In this thesis, a commercial software CFD-ACE+ is adopted to simulate how to create a nano-liter droplet and then fabricate the corresponding device to prove it. It also will discuss the relationship between the shapes of electrode and EWOD driving forces.

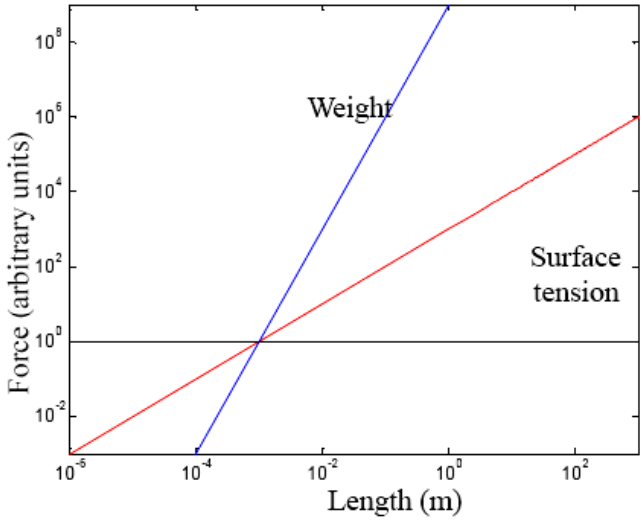

Fig. 1-1 Scaling of weight and surface tension [3]

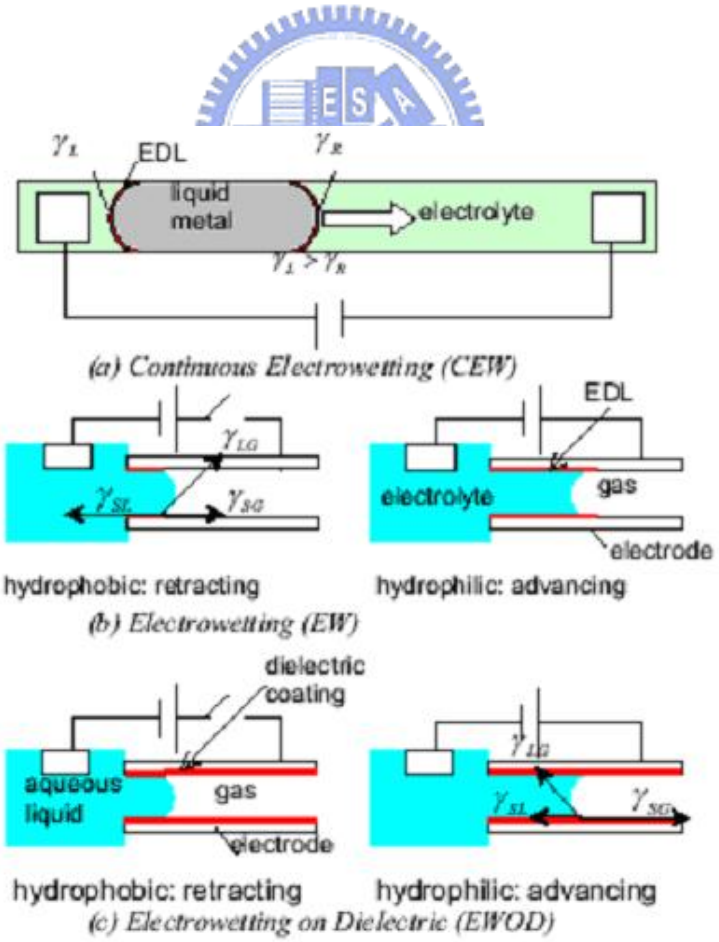

Fig. 1-2 Move liquid metal (mercury) in the electrolyte by CEW [5]

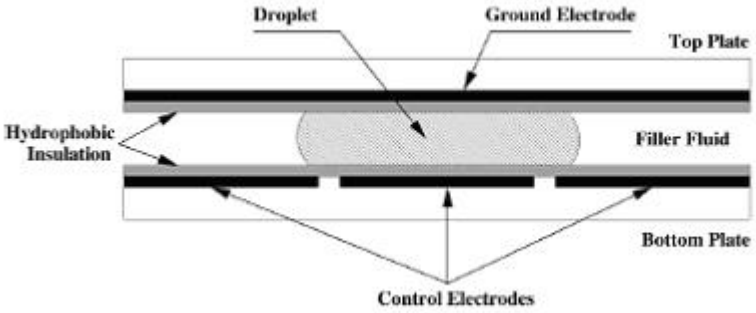

Fig. 1-3 Illustration of continuous electrowetting device [6]

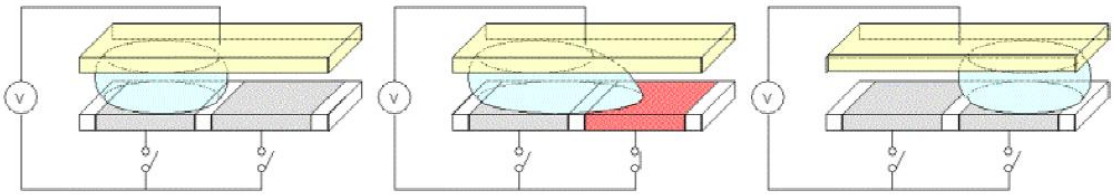

Fig. 1-4 Illustration of method to move droplet by EWOD [7]

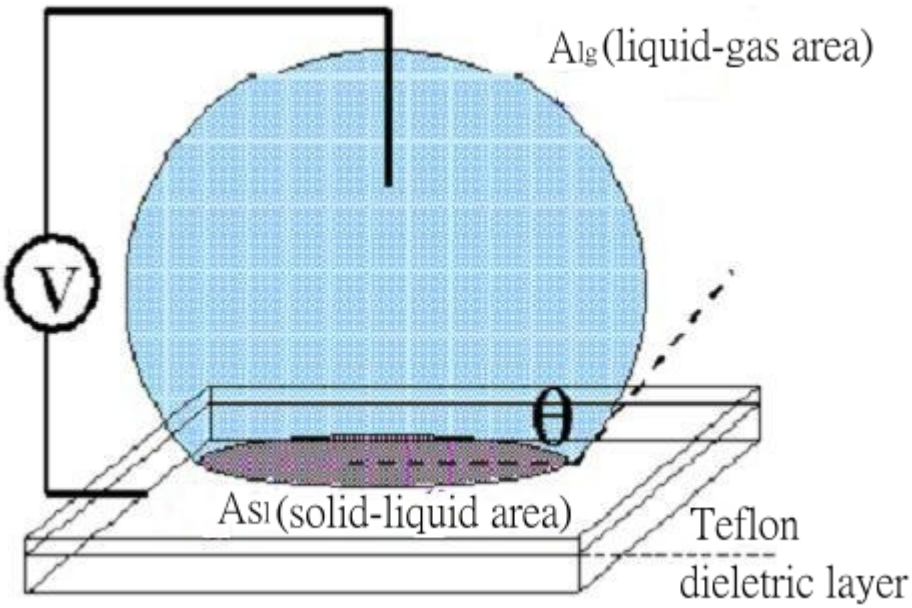

Fig. 1-5 Contact angle and its surface tension [7]

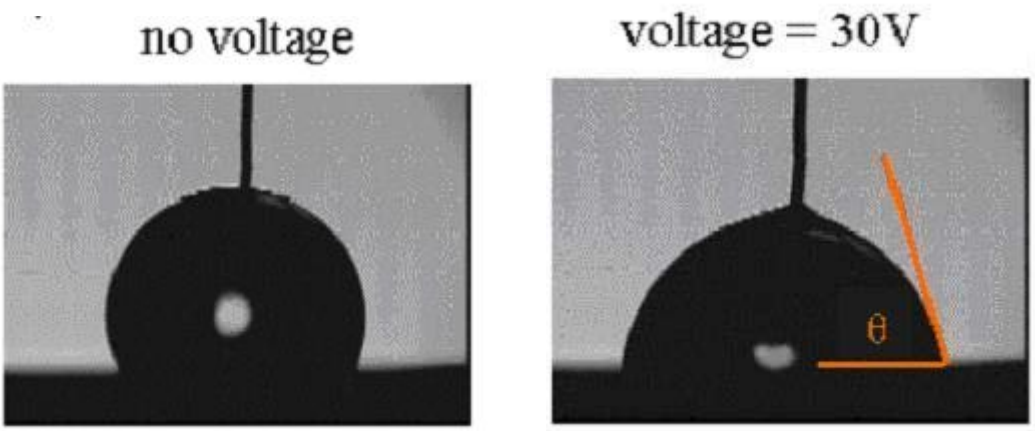

Fig. 1-6 The field applied changes the surface tension at the liquid-solid and liquid-vapor interfaces, causing the droplet to flatten [7]

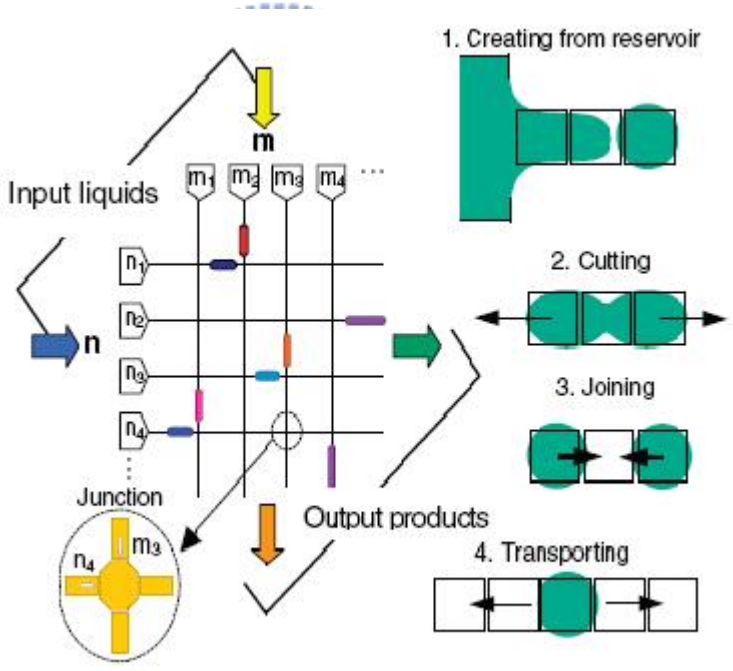

Fig. 1-7 Digital and addressable microfludic circuit [9]

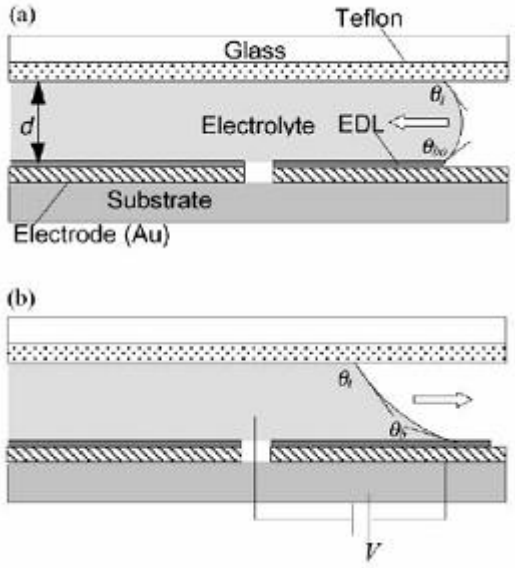

Fig. 1-8 Contact angle of droplet changed in the parallel plates [5]

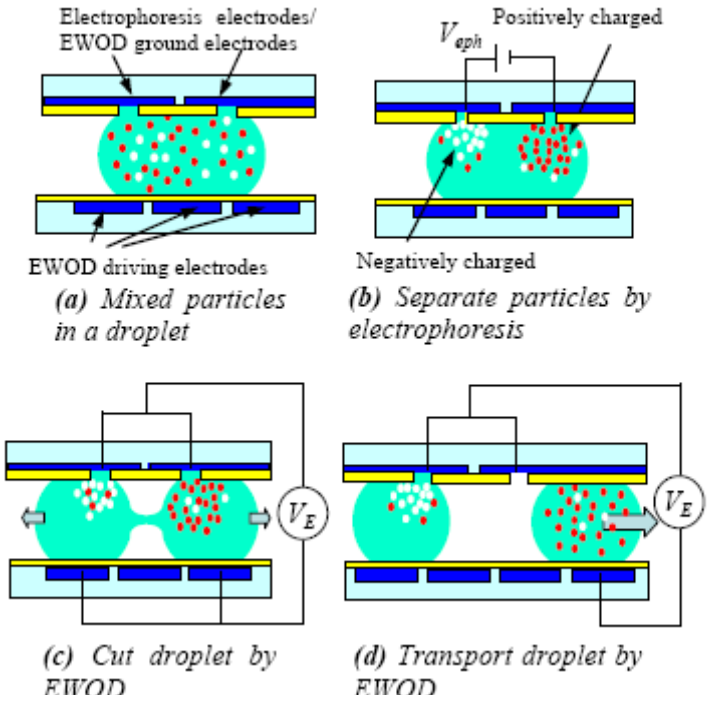

Fig. 1-9 Separation of two types of particle [10]

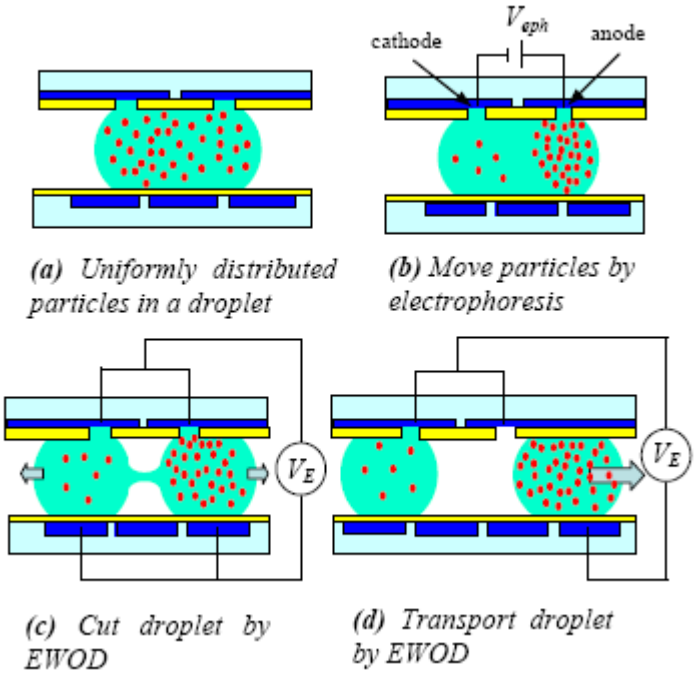

Fig. 1-10 Control particle concentration [10]

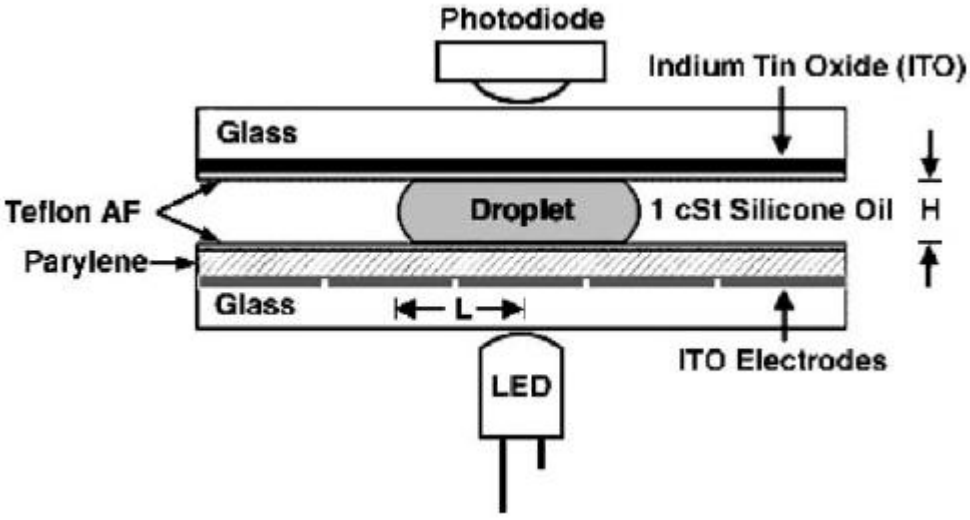

Fig. 1-11 The optical detection instrumentation [11]

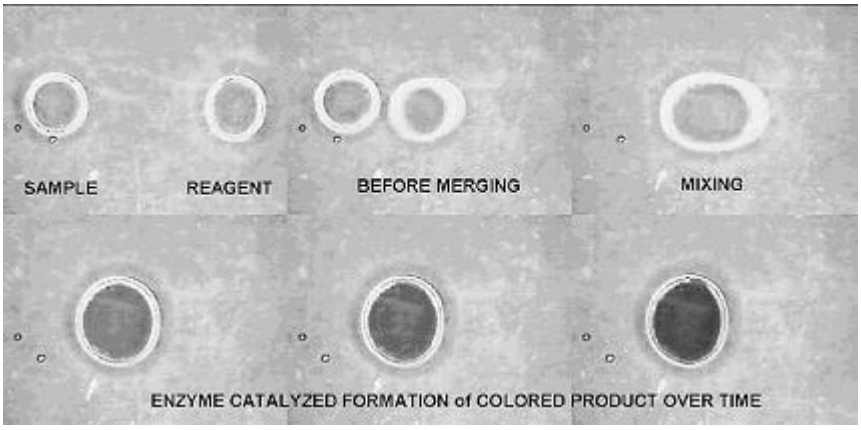

Fig. 1-12 The trinder reaction of glucose concentration [11]

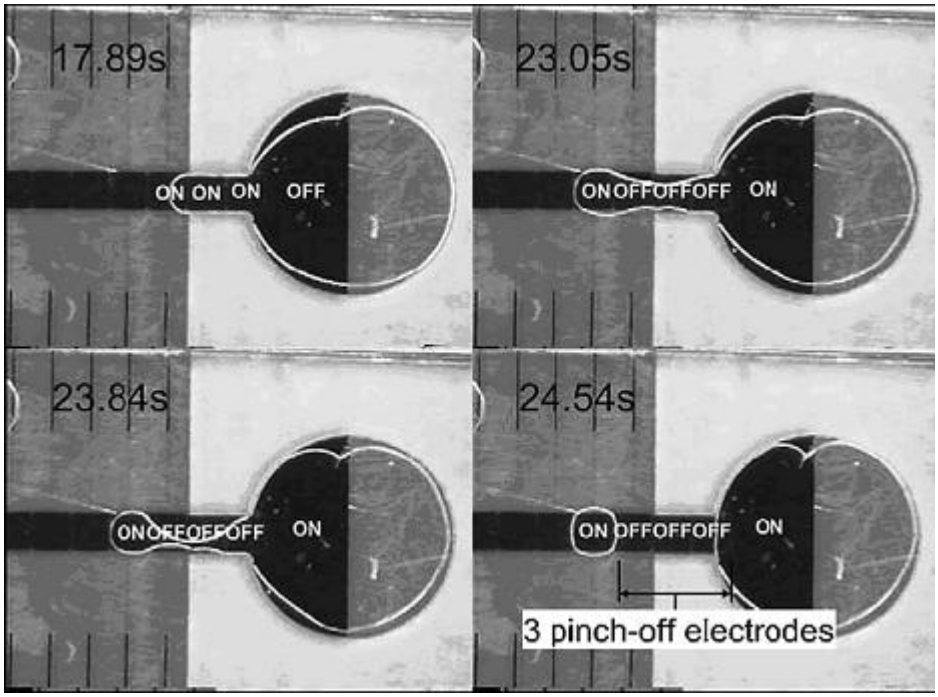

Fig. 1-13 Creating nano-liter by auto-control system [12]

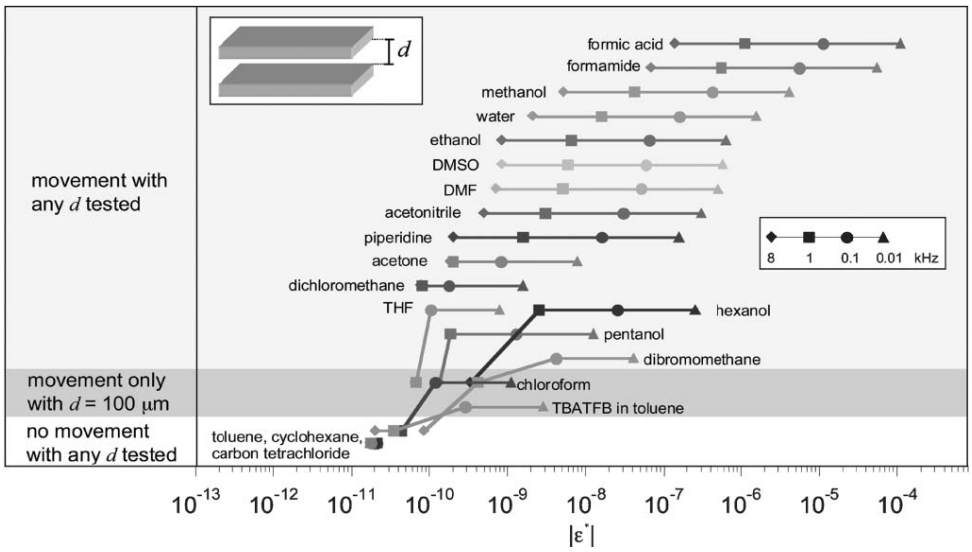

Fig. 1-14 The relative illustration of channel height and manipulative frequencies [13]

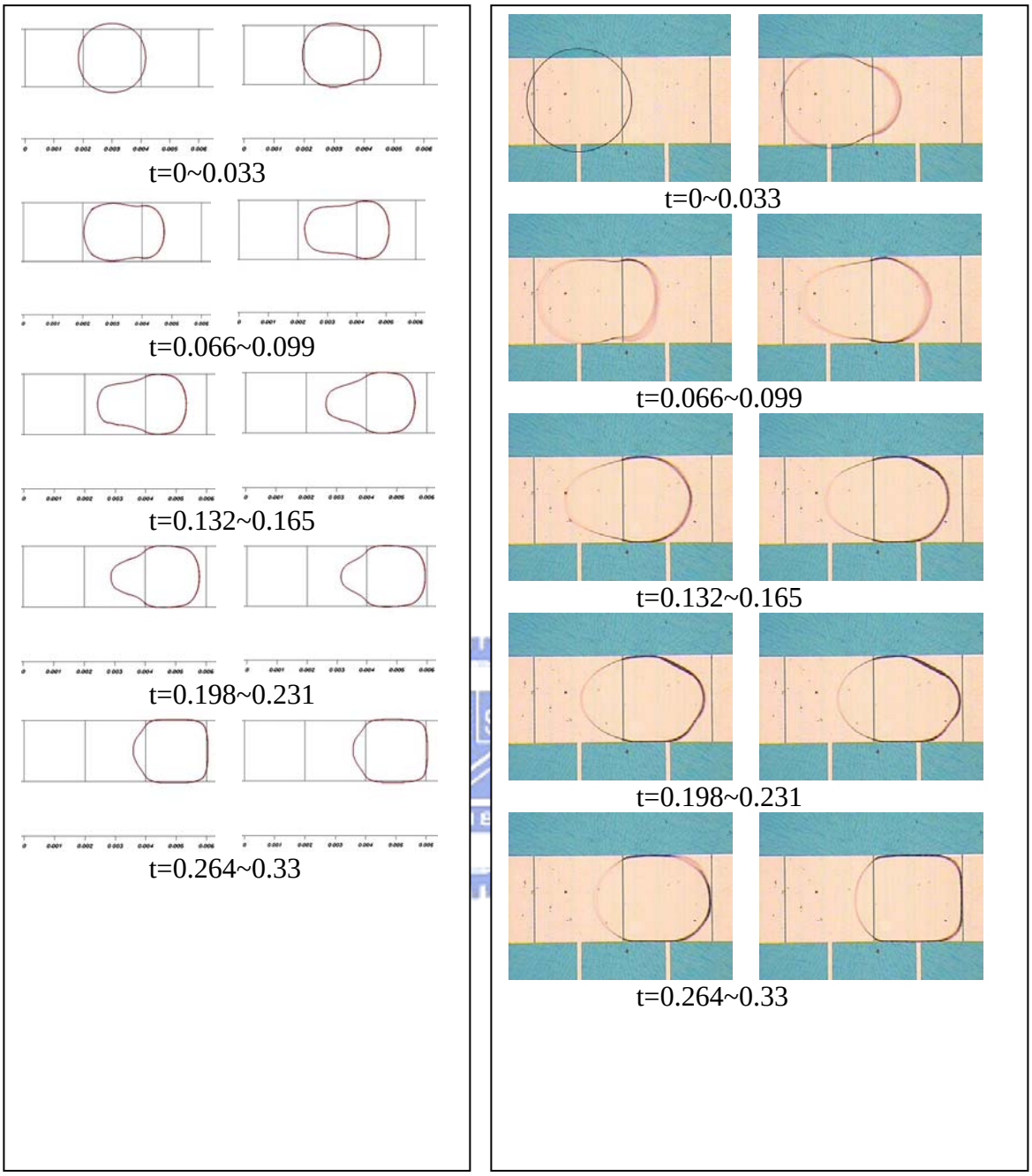

Fig. 1-15 Comparison between simulation and experiment [14][15]

CHAPTER 2
MATHEMATICAL MODEL AND NUMEICAL METHOD

2.1 Mathematical method

The actuation principle of EWOD is that a droplet is placed on an electrode covered first by a dielectric layer and then Teflon layer. Because the hydrophobic stuff makes contact area of liquid and solid decreasing, the droplet contact angle is larger than the one without coating of dielectric layer [1]. When the potential is applied, the altered stored electric charge density in the liquid-solid interface makes droplet contact angle becoming smaller. The main driving force is surface tension. It causes droplet contact angle to change after the potential is applied on adjacent electrodes, and the droplet is driven by the different pressure between the inside and outside of the droplet. The surface tension magnitude is obtained by the change of droplet contact angle. The knowledge of the contact angle and its corresponding saturation for different liquids on different materials can be used to design and control the microfluidic devices. The equations for EWOD are as follow:

2.1.1 Electric double layer

While liquid metal, as mercury, is immersed in electrolyte, the interface between two media becomes electrically charged owing to various electrochemical activities to cause adsorption of electrolyte ions on metal surface. This interface is named polarizable interface, electrified or electric double layer (EDL) [2]. The EDL thickness is around 10-100 $\mathring{A}$ depending

on the kind of electrolyte-metal pair, concentration of the electrolyte, electrical condition and temperature. In Fig. 2-1, the charged density is originally distributed uniformly along the X-direction while no external potential. The liquid-metal containing the EDL is positive charged and the electrolyte is negative charged. If a potential is applied between the two electrodes in the electrolyte, a low current flows across the electrolyte between the liquid metal and the channel wall resulting in a decrease in voltage along the X-direction, as shown in Fig.2-2 [2]. The potential difference across the EDL produces a surface tension gradient to move liquid metal from left to right. It has been found that a thin dielectric layer inserted between the electrode and droplet can emulate in EWOD.

2.1.2 Lippman's equation

In 1875, Lippman made an electrocapillarity experiment, and found firstly that the capillarity force is changed by external electric charges on the interface between liquid metal and electrolyte. The Lippman's equation for the capillarity phenomenon is as follow:

$$\gamma = \gamma_0 - \frac{1}{2} c V^2, \tag{2.1}$$

where γ_0 is the surface tension of solid-liquid interface without external potential ($V = 0$), c the capacitance per unit area of EDL and V the applied voltage. In EWOD phenomenon, Lippman equation mainly discusses the relationship between external voltage and surface tension.

2.1.3 Young's equation and Lippmann-Young equation

For the theoretical model, the droplet is assumed as an ideal sphere with a

radius R and the contact angle θ (see Fig. 2-3). Moreover, the system is in equilibrium at constant potential V. Any effects of the droplet edge like stray capacitance are neglected. The contact angle hysteresis for increasing and decreasing voltage is not considered and the droplet volume v is considered to be constant, *i.e.*, $dv = 0$. The contact angle θ is the angle between the liquid-vapor and the solid-liquid interface at the triple phase point. θ varies with the applied voltage and hence the droplet shape changes. The total energy of the system, E_{sys}, is expressed as [16]:

$$E_{sys} = E_{\text{int}} + E_{de} + E_{vs}, \tag{2.2}$$

where E_{int} is the interfacial potential energy of the droplet, E_{de} is the energy stored in the solid dielectric layer between the liquid and the counter electrode, and E_{vs} is the potential energy, performed by an external voltage source to redistribute the charges when the shape of the droplet changes. E_{sys} is minimum at equilibrium so that the total differential of the energy, dE_{sys}, is equal zero. As the functions of R and θ, dE_{sys} is given by:

$$dE_{sys} = [\frac{\partial E(R,\theta)_{sys}}{\partial R}]dR + [\frac{\partial E(R,\theta)_{sys}}{\partial \theta}]d\theta. \tag{2.3}$$

Equation (2.3) expresses that at equilibrium of the system, any infinitesimal change in energy due to shape variations of the droplet must be zero. With the restriction of a constant droplet volume ($dv = 0$), Shapiro et al. rewrites Eq. (2.3) as

$$(-\frac{2+\cos\theta}{2\pi R^2 \sin\theta})\{[\frac{\partial E(R,\theta)_{sys}}{\partial R}]\cdot R\cdot(-\frac{2\cos^2(\theta/2)\cdot\cot(\theta/2)}{2+\cos\theta}) + [\frac{\partial E(R,\theta)_{sys}}{\partial \theta}]\} = 0. \tag{2.4}$$

It firstly considers a droplet on the dielectric layer while no external voltage is applied to the system (E_{de} = 0 and E_{vs} = 0). The system energy is defined

as the interfacial potential energy of the droplet (E_{int}).

$$E_{\text{int}} = (\gamma_{SL} - \gamma_{SV}) \cdot A_{SL} + \gamma_{LV} \cdot A_{LV} . \tag{2.5}$$

The energy of a liquid on a solid surface depends on the interfacial tension between the solid-liquid γ_{SL}, the solid-vapor γ_{SV} and the liquid-vapor γ_{LV} interface. The subscript *L, V* and *S* denote liquid, vapor and solid phases, respectively. A_{SL} is the base area of the droplet on the solid surface and A_{LV} is the liquid-vapor interface area. Both are defined by R and θ as:

$$A_{SL}(R,\theta) = \pi R^2 \sin^2 \theta . \tag{2.6}$$

$$A_{LV}(R,\theta) = 2\pi R^2 (1-\cos\theta) . \tag{2.7}$$

Using Eqs. (2.5), (2.6) and (2.7), the system energy is expressed as

$$E_{sys}(R,\theta) = R^2[(\gamma_{SL} - \gamma_{SV}) \cdot \pi \cdot \sin^2 \theta + \gamma_{LV} \cdot 2\pi \cdot (1-\cos\theta)] . \tag{2.8}$$

Combine Eqs. (2.4) and (2.8), the Young equation can be derived as

$$\cos\theta = \frac{\gamma_{SV} - \gamma_{SL}}{\gamma_{LV}} . \tag{2.9}$$

It considers the case, which an external voltage *V* is applied to the system. Besides, in the previous case the potential energy, E_{de}, stored in the dielectric layer between the liquid and electrode counter contributes to the total energy

$$E_{de}(R,\theta) = \frac{1}{2}\varepsilon_0 \int_v \vec{E}\vec{D} dv , \tag{2.10}$$

where v is the volume of the dielectric layer, $\vec{E}$ the electric field and $\vec{D}$ the charge displacement. Note that $\vec{D} = \varepsilon_0 \varepsilon_r \vec{E}$, in which ε_0 is the permittivity of vacuum and ε_r the dielectric constant of the solid. By

integrating Eq. (2.10), E_{de} can be written as:

$$E_{de}(R,\theta) = \frac{1}{2}\varepsilon_0\varepsilon_r \frac{V^2}{d} A_{SL} . \tag{2.11}$$

E_{de} is equivalent to the energy stored in a plate capacitor filled with a dielectrics of thickness d. The base of the droplet A_{SL} defines the size of one electrode. Any change in the droplet shape appears as a change in the capacity and requires a redistribution of the charge. The necessary work performed by the external electrical source is twice the potential energy stored in the dielectric layer. The negative sign for the electrical energy E_{vs} in Eq. (2.12) corresponds to this fact:

$$E_{de}(R,\theta) = -\varepsilon_0\varepsilon_r \frac{V^2}{d} A_{SL} . \tag{2.12}$$

Combining Eq. (2.5), (2.11) and (2.12), the system energy is given by:

$$E_{sys}(R,\theta) = R^2[(\gamma_{SL} - \gamma_{SV} - \frac{\varepsilon_0\varepsilon_r V^2}{2d}) \cdot \pi \cdot \sin^2\theta + \gamma_{LV} \cdot 2\pi \cdot (1-\cos\theta)], \tag{2.13}$$

and together with Eq. (3), the Young-Lippman equation is recovered as:

$$\cos\theta - \cos\theta_0 = \frac{1}{2}\frac{\varepsilon_0\varepsilon_r V^2}{d}, \tag{2.14}$$

Where θ_0 is the contact angle without an external voltage and θ is the one with an external voltage. The Lippman-Young equation yields the influence on the contact angle when a potential is applied to the dielectric layer.

2.1.4 EWOD in parallel plates

In the EWOD device, a droplet is placed between two parallel plates. To

understand EWOD actuation of a droplet in parallel plates, it can be equivalent to an electrical circuit model of the device as shown in Fig.2-4. When DC voltage is applied, the droplet has a relationship between voltage and capacitor in parallel, as follows:

$$C = \frac{Q}{V}$$

$$Q_{Top} = Q_{Bottoms}$$

$$V_{DC} = V_{Top,DC} + V_{Bottom,DC} \tag{2.15}$$

The voltage across the top plate, $V_{Top,DC}$, can be expressed as

$$V_{Top,DC} = \frac{C_{Bottom,DC}}{C_{Bottom,DC} + C_{Top,DC}} V_{DC} \tag{2.16}$$

and the voltage across the bottom plate, $V_{Bottom,DC}$, is:

$$V_{Bottom,DC} = \frac{C_{Top,DC}}{C_{Bottom,DC} + C_{Top,DC}} V_{DC} \tag{2.17}$$

Q : Charges in the capacitor.

C_{Top} : Capacitor on the top plate.

C_{Bottom} : Capacitor on the bottom plate.

It can be known that U, the electrical energy in the capacitor, becomes larger as d becomes smaller from the equation of parallel-plate capacitor ($U = QV = \frac{1}{2}cV^2 = \frac{1}{2}\frac{\varepsilon_0 \varepsilon_r}{d}V^2$). Comparing with the electrode on the top plate, whose thickness is smaller than the bottom one, the electrode has a tiny

hydrophobic layer, so that C_{Top} is much higher than C_{Bottom}. By the theory of electrical circuits, the voltage drop is almost on bottom plate because of $V_{Bottom,DC} >> V_{Top,DC}$; the droplet contact angle on top plate is changed insignificantly while the DC potential is applied on top plate.

2.1.5 Actuation force

A droplet produces a driving force on different hydrophobic surfaces, induced by the gradient of surface tension. According to the conservation of thermodynamics, it is must obey Laplace-Young equation on the interface of droplet and surrounding air. As shown in Fig. 2-5, it can deduce the equations as:

$$dA = (x+dx)(y+dy) - xy = xdx + ydy$$

$$dw = \gamma dA = \gamma(xdx + ydy)$$

$$dw = \Delta pxydz$$

$$\frac{x+dx}{R_1+dz} = \frac{x}{R_1} \rightarrow dx = \frac{xdz}{R_1}$$

$$\frac{y+dx}{R_2+dz} = \frac{y}{R_2} \rightarrow dx = \frac{ydz}{R_2}$$

$$\Delta pxydz = \gamma(xdx + ydy) = \gamma(xy\frac{dz}{R_2} + xy\frac{dz}{R_1})$$

$$\Delta p = \gamma(\frac{1}{R_1} + \frac{1}{R_2}) \qquad (2.18)$$

where Δp is the pressure difference across an interface and R_1 and R_2

are the two radii of curvature of the droplet curved surface. In order for a droplet to produce the gradient of surface tension, it must have two dissimilar wettability contact surfaces. The pressure difference Δp_1 is the droplet at the interface between the strong hydrophobic surface and surrounding air and Δp_2 is the droplet at the interface of the weak hydrophobic surface and surrounding air. Because of $\Delta p_1 > \Delta p_2$, the droplet has a net pressure difference that can drive the droplet, consequently, the droplet automatically moves from the strong to weak hydrophobic surfaces.

Fig. 2-6 shows that a droplet is placed between two parallel plates with a channel height h. The contact angle on the top plate is $\cos\theta_{Top}$ and the bottom one is $\cos\theta_{Bottom}$. When DC voltage is applied on the right electrode, the surface tension (γ_{sl}) and θ_b on the right electrode are changed slightly and then the net difference pressure drives the droplet to move toward direction with less contact angle. The pressure difference at the left droplet can be expressed as [17]:

$$\Delta P_L = P_a - \frac{\gamma_{LG}}{D}(\cos\theta_T + \cos\theta_{b0}), \tag{2.19}$$

and the pressure difference at the right droplet is

$$\Delta P_R = P_a - \frac{\gamma_{LG}}{D}(\cos\theta_T + \cos\theta_b). \tag{2.20}$$

Combining Eqs. (2.19) and (2.20), the net pressure difference is:

$$\Delta P = \Delta P_L - \Delta P_R = \frac{\gamma_{LG}}{D}(\cos\theta_b - \cos\theta_{b0}). \tag{2.21}$$

Substituting Eq. (2.14) into Eq. (2.21), it obtains

$$\Delta P = \Delta P_L - \Delta P_R = \frac{1}{2}\frac{cV^2}{D} = \frac{1}{2}\frac{\varepsilon_0\varepsilon_r V^2}{D} \tag{2.22}$$

From Eq. (2.22), it can be seen that the pressure difference is influenced by the channel height, dielectric coefficient and applied potential, in addition to the change of contact angle. In a controllable system, the droplet is easier to drive as ΔP becomes larger.

2.1.6 Droplet cutting

Initially, a droplet occupies the entire middle electrode as well as the portions of left and right electrodes. When DC voltage is applied at the ends but not middle, it results in making the two ends wetting and keeping the middle non-wetting. A pressure difference in the droplet drives the droplet to move toward both the left and right electrodes and causes necking in the middle electrode. This situation makes the radius of droplet necking and cuts the droplet into two parts.

According to Fig. 2-7 [9], the channel height is related to the contact angle difference and radii of curvature [9] as

$$\frac{R_2}{R_1} = 1 - \frac{R_2}{D}(\cos\theta_2 - \cos\theta_1). \tag{2.23}$$

Equation (2.23) provides an important criterion for cutting a droplet. The cutting is initiated by necking the middle of the droplet, which means the radius R_1 becomes negative (i.e. $\frac{R_2}{R_1} < 0$). Based on the literature [9], Kim et al. explained that the two necking menisci meet and pinch off the droplet, R_2 should be roughly a half length of the control electrode side and R_1 should also be about the same length but with the opposite sign. When $\frac{R_2}{R_1}$ is -1, the radius ratio is just making droplet cutting. From Eq. (2.23), it can

deduce the channel height limitation that needs to cut droplet as:

$$\frac{R_2}{h}(\cos\theta_{b2} - \cos\theta_{b1}) = 2$$

$$h = \frac{R_2}{2}(\cos\theta_{b2} - \cos\theta_{b1}), \tag{2.24}$$

where $\cos\theta_{b1}$ is the contact angle without an external applied voltage and $\cos\theta_{b2}$ is the one with an external applied voltage, d is channel height, R is the principal radius of curvature, as shown in Fig. 2-7. Because R_2 equals roughly a half length of the control electrode side, $\cos\theta_{b1}$ is known and $\cos\theta_{b2}$ can be obtained from Eq. (2.24), h can be determined as well. In this study, the channel height limitation is an important parameter used in our simulation.

2.2 Numerical Method

In this work, the simulation of EWOD was carried out by using the commercial software CFD-ACE+. In order to avoid wasting time and reduce experiment cost, a new design of electrode shape was done to simulate a droplet in AC condition and to investigate its features. The results are discussed in chapter 4.

2.2.1 Numerical method

The droplet simulated in this study is based on Continuity Equation, Momentum Equation, SIMPLEC Method [18] and CFS Model [19]. The SIMPLEC (Semi-Implicit Method for Pressure-Linked Equations Consistent)

Method is used to compute the properties of velocity and pressure in the grids. The liquid-gas interface is using CFS (Continuum Surface Force) Method to simulate the surface tension influencing interface. Eventually, it can accurately calculate the interface location and moving direction in the grids.

2.2.2 Governing equations

In this simulation, the model is using Continuity and Momentum Equations to compute velocity and pressure in fluid field. The basic assumptions of fluid field are:

1. The fluid is Newtonian fluid.
2. The flow is incompressible and laminar without consideration of body force.

From above assumptions, the governing equations are:

Continuity Equation:

$$\frac{\partial \rho}{\partial t} + \nabla \bullet \left(\rho \vec{V} \right) = 0 \tag{2.25}$$

Momentum Equations:

$$\frac{\partial u}{\partial t}(\rho u) + \nabla \cdot \rho \vec{V} u = -\frac{\partial p}{\partial x} + \frac{\partial}{\partial x}\left[2\mu \frac{\partial u}{\partial x} \right] + \frac{\partial}{\partial y}\left[\mu \left(\frac{\partial v}{\partial x} + \frac{\partial u}{\partial y} \right) \right] + \frac{\partial}{\partial z}\left[\mu \left(\frac{\partial u}{\partial z} + \frac{\partial w}{\partial x} \right) \right] + F_x^{\sigma} + \rho g_x \tag{2.26}$$

$$\frac{\partial v}{\partial t}(\rho v) + \nabla \cdot \rho \vec{V} v = -\frac{\partial p}{\partial y} + \frac{\partial}{\partial x}\left[\mu \left(\frac{\partial v}{\partial x} + \frac{\partial u}{\partial x} \right) \right] + \frac{\partial}{\partial y}\left[2\mu \frac{\partial v}{\partial x} \right]$$

$$+\frac{\partial}{\partial z}\left[\mu\left(\frac{\partial v}{\partial z}+\frac{\partial w}{\partial y}\right)\right]+F_y^{\sigma}+\rho g_y \qquad (2.27)$$

$$\frac{\partial w}{\partial t}(\rho w)+\nabla\cdot\rho\vec{V}w=-\frac{\partial p}{\partial y}+\frac{\partial}{\partial x}\left[\mu\left(\frac{\partial u}{\partial z}+\frac{\partial w}{\partial x}\right)\right]+\frac{\partial}{\partial y}\left[\mu\left(\frac{\partial v}{\partial z}+\frac{\partial w}{\partial y}\right)\right]$$
$$+\frac{\partial}{\partial z}\left[2\mu\frac{\partial w}{\partial z}\right]+F_z^{\sigma}+\rho g_z \qquad (2.28)$$

where $\vec{V}$ is the velocity vector, p the pressure, ρ the fluid density, μ the viscosity coefficient, $\vec{F}^{\sigma}$ the surface tension on liquid-gas interface and $\rho\vec{g}$ the fluidic gravity.

In the above Momentum Equations, surface tension is composed of continuous surface-tension model [19]:

$$\mathbf{F}_s^{\sigma}=\sigma k\hat{n} \qquad (2.29)$$

where F_s^{σ} is the micro surface tension, composed of the normal and tangent directions on interface , σ the surface tension value, $k=-\nabla\bullet\hat{n}$ the mean interface curvature and $\hat{n}$ the unit vector on interface [20]. Through the continuous surface-tension model, the surface tension is able to be shown completely in Momentum Equation.

2.2.3 Free surface module

The basis of the approach employed by the free surface module is volume-of-fluid (VOF), published in an earlier form elsewhere [21], and is recently extended [22]. The model can accommodate any two fluids that are incompressible and immiscible and between which localized slip is negligible. Water and air (when compressibility is insignificant) are good examples. In

this study, a VOF interface tracking method proposed by Hirt and Nichols [] is adopted to represent the fluid domain and track the evolution of the domain's free boundaries.

The defined characteristics of the VOF methodology is that the distribution of the second fluid (such as water) in the computational grid is described by a single scalar field variable, F, which specifies the fraction of the volume of each computational cell in the grid that is occupied by the second fluid (water). Thus, F takes the value of one in cells that contain only fluid 2 (water) and the value of zero in cells that contain only fluid 1 (air). A cell that contains an interface would have an F value between zero and one. The manner in which the volume fraction distribution F (and hence the distribution of fluid 2) evolves is determined by solving the passive transport equation.

$$\frac{\partial F}{\partial t} + \nabla \cdot \vec{v}F = 0 \quad , \tag{12}$$

where F is the liquid volume fraction, t the time, ∇ the standard spatial grad operator, and $\vec{v}$ the velocity vector. This equation must be solved together with the fundamental conservation equations of mass and momentum in CFD-ACE+ to achieve computational coupling between the velocity field solution and the liquid distribution.

In CFD-ACE+ code, surface reconstruction is a prerequisite for determining the flux of fluid 2 from one cell to the next, and for determining surface curvatures when the surface tension model is activated. The following two approaches to surface reconstruction are currently available.

- Single Line Interface Construction (SLIC) Method [23]
- Piecewise Linear Interface Construction (PLIC) Method [24]

The original SLIC method approximates the interface in each mesh cell as a line that is parallel to one of the coordinate axes in a two-dimensional analysis, as shown in Fig. 2-8(b). However, the representation of the interface using SLIC is rough. The piecewise-linear interface calculation (PLIC) technique proposed by Youngs represents a useful refinement to the SLIC method using a straight line to approximate the interface in each computational cell, as displayed in Fig. 2-8(c). The PLIC method [25][26] is adopted and then coupled to the VOF method in this work.

2.2.4 SIMPLEC algorithm

Solutions to the three momentum equations yield the three Cartesian components of velocity. Pressure-based approaches use the continuity equation to formulate an equation for pressure. In CFD-ACE+ code, SIMPLEC scheme is adopted. SIMPLEC stands for Semi-Implicit Method for Pressure-Linked Equations Consistent, and represents an enhancement of the well known SIMPLEC algorithm. SIMPLEC originally was proposed by Doormaal et al. in 1984 [27], an equation for pressure-correction is derived from the continuity equation. It is an inherently iterative method. Fig. 2-9 summarizes the SIMPLEC procedure.

2.3 Grid density

The meshing elements and accuracy of the numerical model was determined by the testing of grid density. The convergence criteria of simulation is 0.0001 (four orders of magnitude) which is the minimum reduction in residuals for each variable. Fig. 2-10 presents the grid density of the numerical model versus the pressure difference in the liquid between

the left and right interfaces, which is the pumping pressure for the motion of the liquid droplet. According to Fig. 2-9, the pressure difference reached a stable value, 650 N/m^2, at a grid density of 150,000 cells/mm^3, which was used in the simulation.

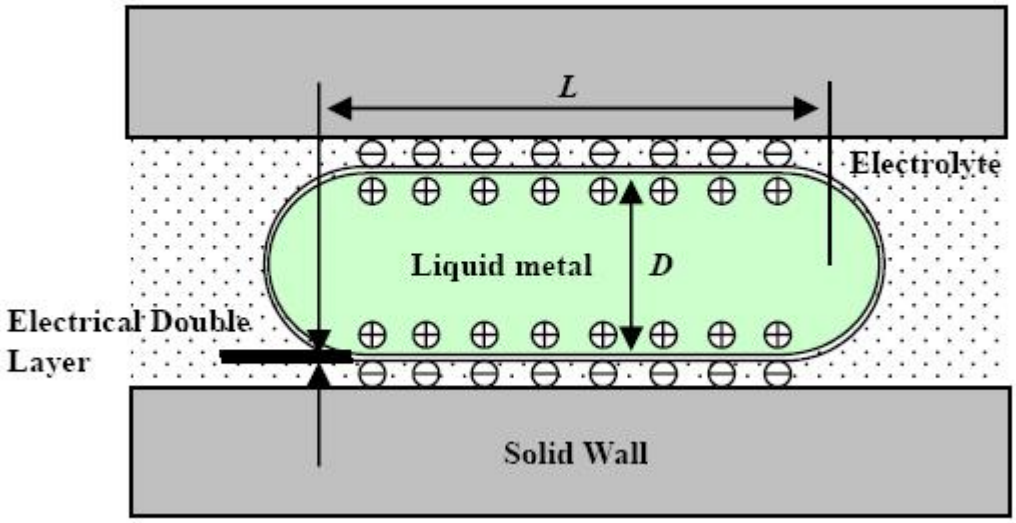

Fig. 2-1 Illustration of Electrical Double Layer [2]

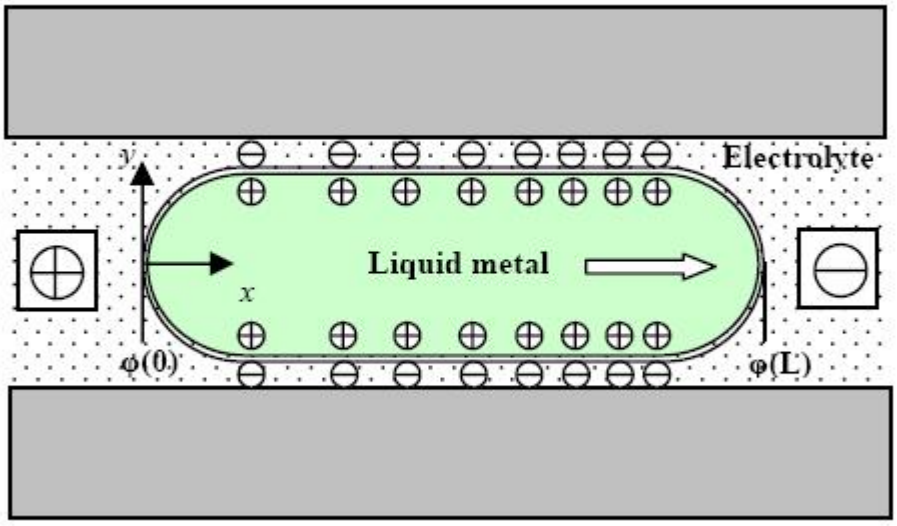

Fig. 2-2 Surface tension changed by Electrical Double Layer [2]

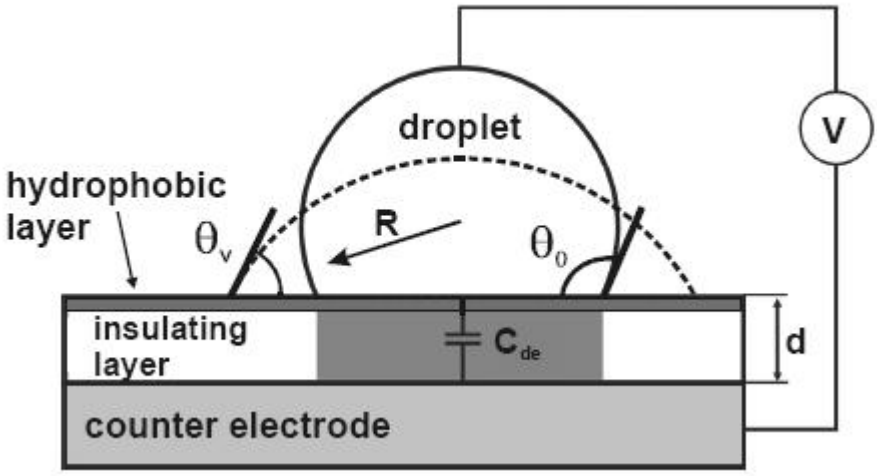

Fig. 2-3 Illustration of basic model used to deduce equations [14]

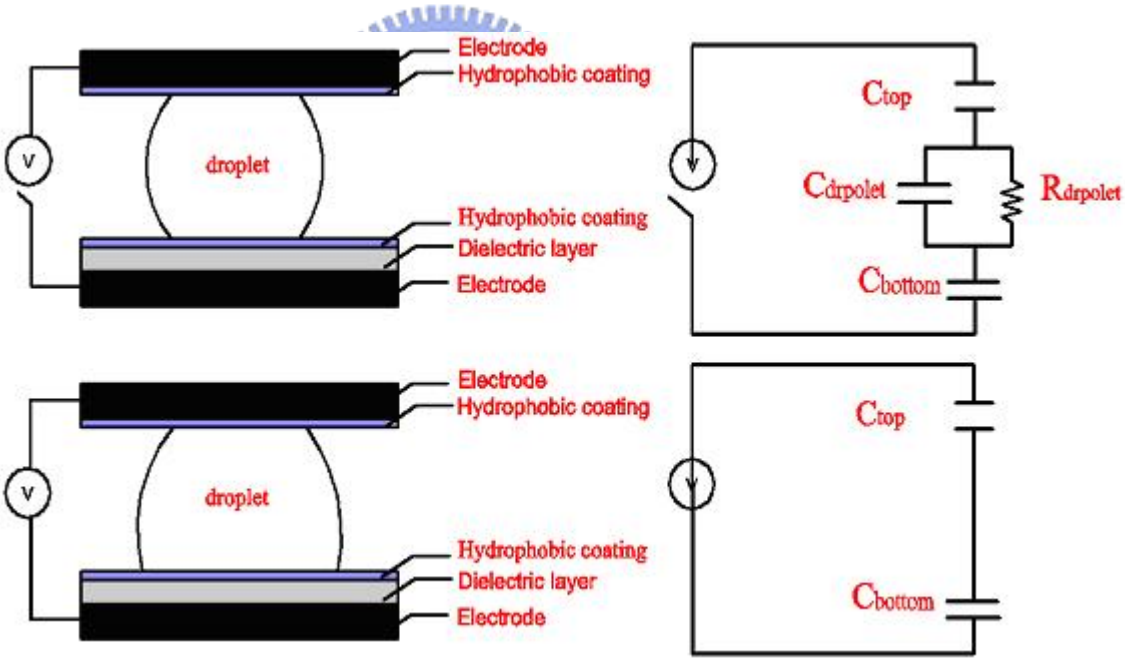

Fig. 2-4 Equivalent circuit of EWOD in the parallel plates [1]

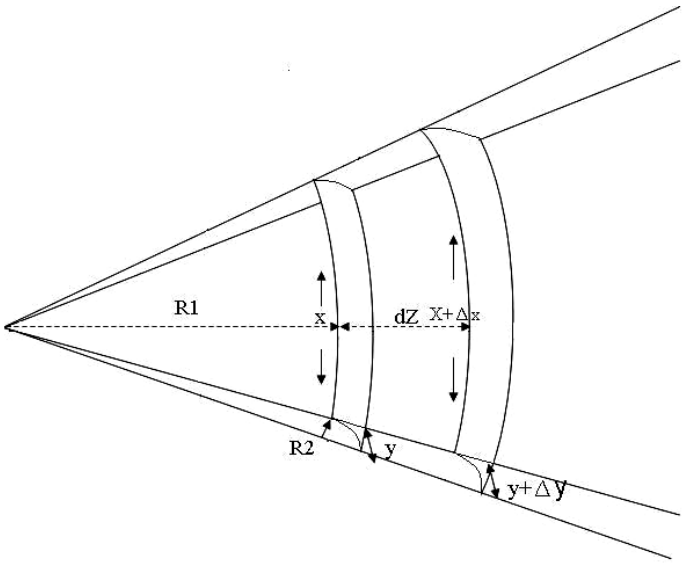

Fig. 2-5 Illustration of deducing pressure difference

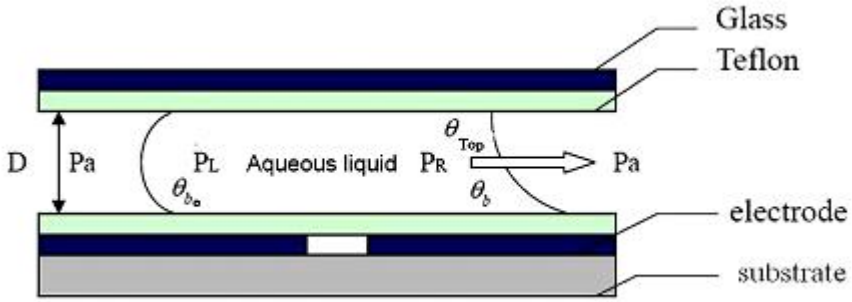

Fig. 2-6 Illustration of droplet moved by different pressure

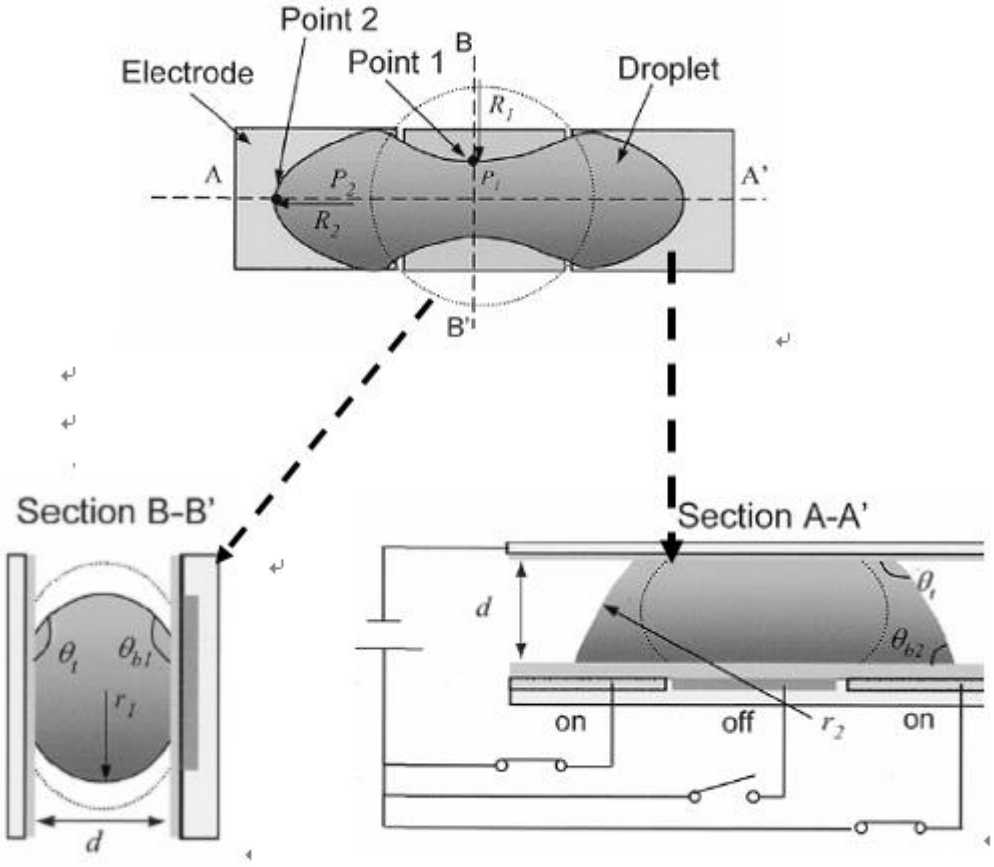

Fig. 2-7 Views of X, Y and Z directions of droplet cutting [9]

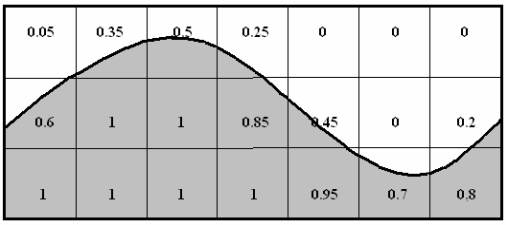

(a) Actual interface

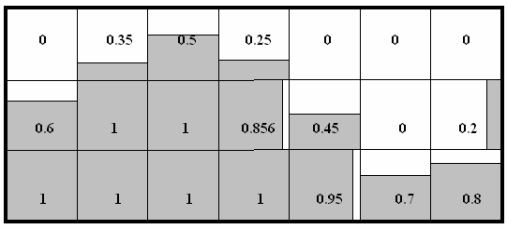

(b) SLIC

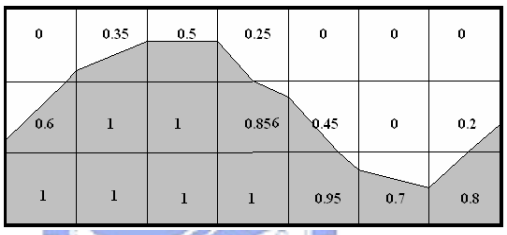

(c) PLIC

Fig. 2-8 Schematic diagram of free surface reconstructions: (a) actual interface; (b) SLIC approximation; (c) PLIC approximation

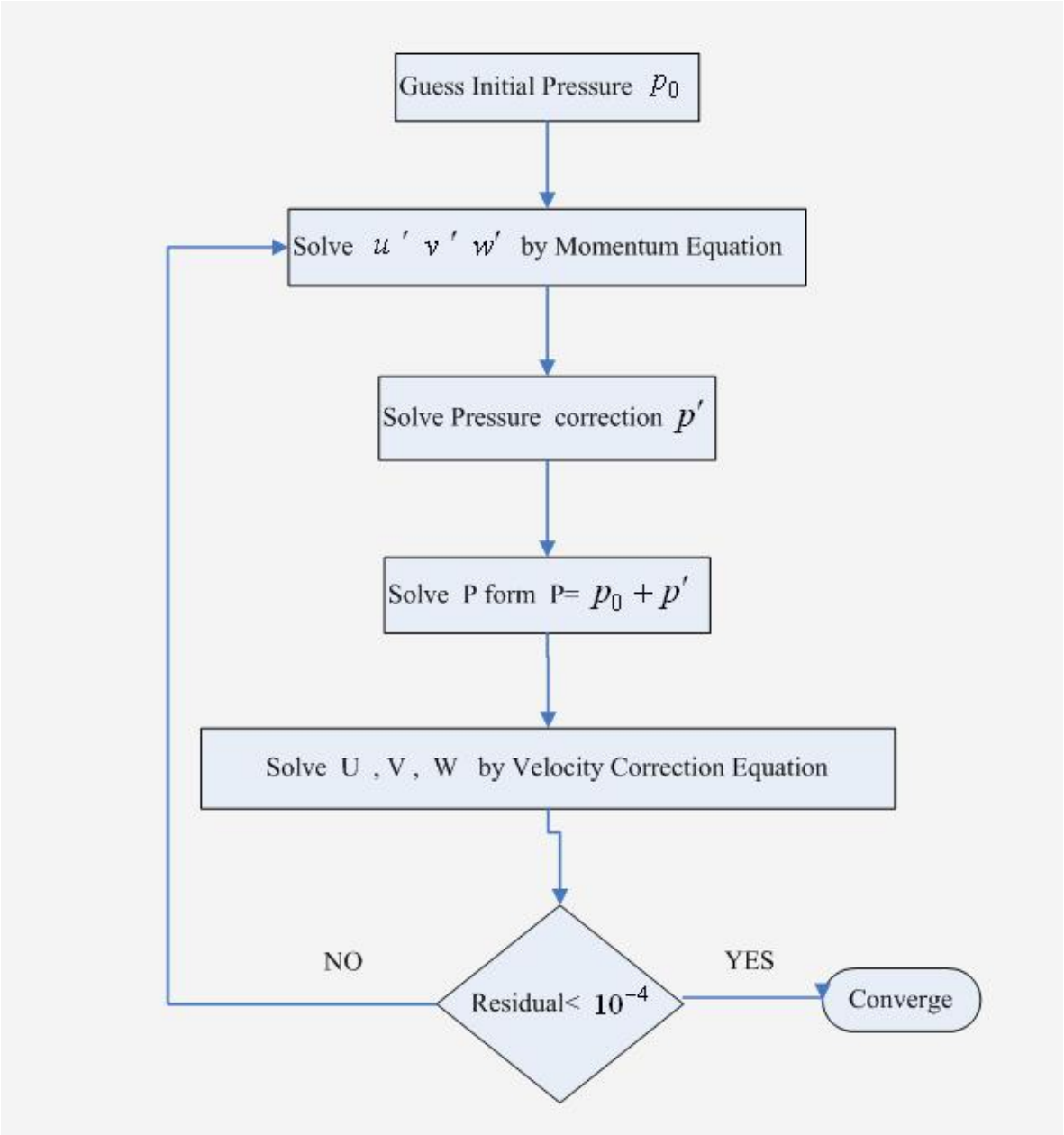

Fig. 2-9 SIMPLEC algorithms

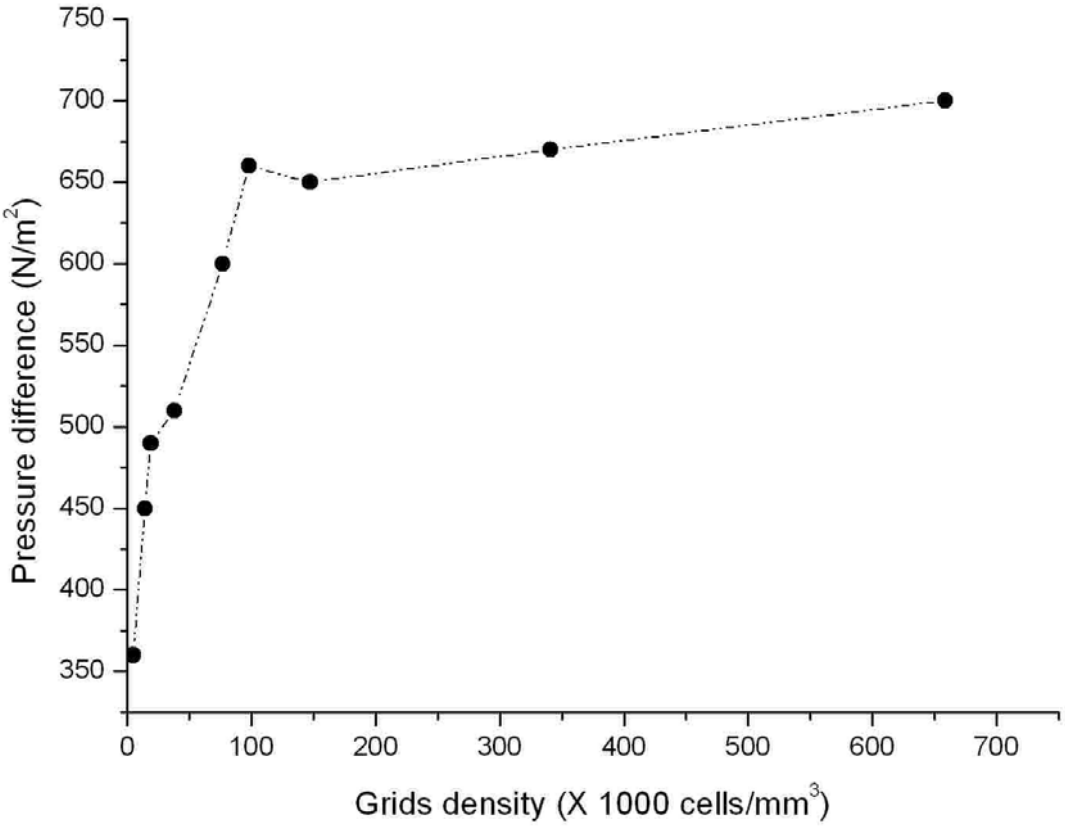

Fig. 2-10 Evolution of the pressure difference against grid density (case 05)

CHAPTER 3
ELECTRODE DESIGNS AND DEVICE PROCESS

It is well-known that for EWOD, the drag of droplet is greater when the channel height becomes smaller. In order to solve this problem, a set of new shape of electrodes with extended rectangles was designed. The difference between the new and original electrodes can be seen in Fig. 3-1, in which the original one is square, whereas the new one is interdigitated with an “extended rectangle”. According to Eq. (2.22), the large pressure difference can move the droplet fancily. So the first step is to design the electrode that can generate large pressure difference. Consequently, the electrode shape and channel height are also needed to take into consideration. The comparison of the original electrodes with new ones will be discussed in next chapter.

3.1 Designs of electrode arrangements

All designed types of electrodes are illustrated in Fig. 3-2. There are nine types of electrodes with different widths of extended electrode, various areas of extended electrode and specific numbers of extended electrode. All of them are summarized in Table 3-1. Fig. 3-3 shows the arrangements of different electrodes, in which the first group is A1and A2, the second group is A3 and A4, the third group is A5 and A6, and the forth group is A7 and A8. For instance, the first group stands for the kind of electrode array in one-dimension, such as A1A2A1A2⋯. Similarly, the other three groups have the same meaning of first group, such as A3A4A3A4⋯, A5A6A5A6⋯ , A7A8A7A8⋯, etc..

Table 3-1 Electrode shapes

Type	Area of main electrode	Area of extended electrode	Width of extended electrode	Number of extended electrode
A1	0.3mm X 0.48mm	0.1mm X 0.08mm	0.08mm	2
A2	0.3mm X 0.48mm	0.1mm X 0.08mm	0.08mm	3
A3	0.3mm X 0.48mm	0.1mm X 0.02mm	0.02mm	2
A4	0.3mm X 0.48mm	0.1mm X 0.02mm	0.02mm	3
A5	0.3mm X 0.48mm	0.1mm X 0.05mm	0.05mm	2
A6	0.3mm X 0.48mm	0.1mm X 0.05mm	0.05mm	3
A7	0.3mm X 0.475mm	0.1mm X 0.025mm	0.025mm	5
A8	0.3mm X 0.475mm	0.1mm X 0.025mm	0.025mm	6

3.2 Experiment Setup

The experimental equipments consist of the contact angle goniometer, microscope, CCD camera and controlled circuit (microcontroller). The schematic configurations are shown in Fig. 3-4. The contact angle goniometer, whose base is on a XYZ platform, is used to measure contact angle on the hydrophobic layer (Teflon layer). The microscope is used to observe droplet motion, such as droplet moving, cutting, velocity and so on, recorded by CCD camera (30 frames/second) and subsequently transferred to the computer. The controlled circuit uses the input of digital signal to control electrodes, switching on or off on the EWOD device, which will be illustrated as follows. The photolithographic mask for EWOD device is shown in Fig.3-5.

3.2.1 Process of EWOD device

A metal layer of 200/800 $\mathring{A}$ Cr/Au was evaporated on glass substrate by E-beam Evaporator. After etching process and re-clean step of glass, SiNx thin film 3000 $\mathring{A}$ is deposited as the dielectric layer of EWOD by PECVD. The next step, photolithography is used to open the bonding pads, and dielectric layer on the bonding pads is removed by dilute buffered oxide etchant (BOE). At last, Dupont Teflon, diluted with 3M FC-77, is spun on the glass by spin coater to complete the fabrication.

Followings are the detailed recipe for fabrication of the above process, which is shown in Fig. 3-6 as well. The top plate process is illustrated in Fig.3-7. Figure 3-8 shows the SEM photo of EWOD device.

(I) Glass substrate process

1. Clean substrate in Caro acid (H_2SO_4 : H_2O_2 = 3 : 1) at 120 $^{\circ}C$ for 600 secs → Immerse the substrate in the deionized (D.I.) water for 60 secs → Blow and dry the substrate by N_2 gun → Put soft bake on hot plate at 100 $^{\circ}C$ for 180 sec.
2. Metal evaporation, E-beam Evaporator, Cr/Au 200/800 $\mathring{A}$.
3. Clean the glass in Acetone (ACE) with ultrasonic vibrator for 900 sec.
4. Soft bake on hot plate at 100 $^{\circ}C$ for 180 sec.
5. Spin coat HMDS, 4000 rpm for 40 sec.
6. Soft bake on hot plate at 100 $^{\circ}C$ for 180 sec.
7. Spin coat Shipley S1818 PR, 500 rpm for 15sec, 4000 rpm for 30sec.
8. Soft bake on hot plate at 100 $^{\circ}C$ for 180 sec.
9. Exposure, Single-Side Mask Aligner.
10. Develop with Shipley MF 315 developer around 20 sec to window above bonding pads.

11. Hard bake on hot plate at 120 $^{\circ}C$ for 600 sec.
12. Wet etching in potassium iodine solution to remove the Au for 4~8 sec.
13. Wet etching in Chromium Photomask Etchant to remove the Cr for 5 sec.
14. Clean the glass in Acetone (ACE) with ultrasonic vibrator for 300 sec, remove the photoresist.
15. Soft bake on hot plate at 100 $^{\circ}C$ for 180 sec.
16. Deposit the Si3N4 by PECVD.
17. Spin coat diluted Teflon AF on the EWOD devices, 500 rpm for 15 sec, 3000 rpm for 30 sec.
18. Hard bake on hot plate, 110 $^{\circ}C$ for 600 sec, 160 $^{\circ}C$ for 1200 sec, and 260 $^{\circ}C$ for 1800 sec.

(II) Silicon wafer substrate process

1. Clean substrate in Caro acid (H2SO4 : H2O2 = 3 : 1) at 120$^{\circ}C$ for 600 sec → Immerse the substrate in the deionized (D.I.) water for 60 sec → Blow the substrate dry by N2 gun → Soft bake on hot plate at 100$^{\circ}C$ for 180 sec.
2. Deposit SiO2 (3000$\mathring{A}$) and SiNx (3000$\mathring{A}$) on the Si-wafer by PECVD.
3. Metal evaporation, E-beam Evaporator, Cr/Au 200/800$\mathring{A}$.
4. Clean the glass in Acetone (ACE) with ultrasonic vibrator for 900 sec.
5. Soft bake on hot plate at 100$^{\circ}C$ for 180 sec.
6. Spin coat HMDS, 4000 rpm for 40 sec.
7. Soft bake on hot plate at 100$^{\circ}C$ for 180 sec.
8. Spin coat Shipley S1818 PR, 500 rpm for 15sec, 4000 rpm for 30sec.
9. Soft bake on hot plate at 100$^{\circ}C$ for 180 sec.
10. Exposure, Single-Side Mask Aligner.
11. Develop with Shipley MF 315 developer around 20 sec to window above bonding pads.
12. Hard bake on hot plate at 120$^{\circ}C$ for 600 sec.
13. Wet etching in potassium iodine solution to remove the Au for 4~8 sec.
14. Wet etching in Chromium Photomask Etchant to remove the Cr for 5 sec.
15. Clean the glass in Acetone (ACE) with ultrasonic vibrator for 300 sec, remove the photoresist.
16. Soft bake on hot plate at 100$^{\circ}C$ for 180 sec.
17. Deposit the Si3N4 by PECVD.
18. Spin coat diluted Teflon AF on the EWOD devices, 500 rpm for 15 sec, 3000 rpm for 30 sec.

19. Hard bake on hot plate, 110 $^{\circ}C$ for 600 sec, 160 $^{\circ}C$ for 1200 sec, and 260 $^{\circ}C$ for 1800 sec.

(III) Top plate process

1. Clean the ITO glass in Acetone (ACE) with ultrasonic vibrator for 600 sec.
2. Spin coat diluted Teflon AF ($1000\,\mathring{A}$) on the ITO glass, 500 rpm for 5 sec, 500 rpm for 15 sec, 3000rpm for 5sec and 3000 for 40sec.
3. Hard bake on hot plate, 110 $^{\circ}C$ for 600 sec, 160 $^{\circ}C$ for 1200 sec, and 260 $^{\circ}C$ for 1800 sec.

3.2.2 Measurement of contact angles

Measurements of the contact angle change by EWOD were made in a DI water droplet using Contact Angle Goniometer (MagicDrop, USA). The 10ul droplet was placed on a 3000 Å dielectric layer of silicon nitride coated with 1000 Å Teflon. A wire was penetrated into the droplet from the top, and the ac potentials with 1 K, 3K, 5K, 7K and 9K Hz, were applied between the liquid and the electrode underneath the dielectric layers. The contact angle was changed from 116° to 76°. The dielectric layers of nitride and Teflon formed two plate capacitors in series. The capacitance of a single capacitor is given by,

$$c = \frac{\varepsilon_r \varepsilon_0}{d} \tag{3.1}$$

where c is the capacitance per unit area. The equivalent capacitance of two capacitors in series can be obtained from the following.

$$\frac{1}{c} = \frac{1}{c_1} + \frac{1}{c_2} \tag{3.2}$$

The dielectric constant (ε_r) of 3000 Å nitride and 1000 Å Teflon is 7.8 and 2, respectively. The equivalent capacitance of the nitride and Teflon layers can be obtained by Eq. (3.1) and (3.2). Fig. 3-9 shows the comparison of the experimental and theoretical contact angles based on Eq. (2.14). The contact angle parabolically decreases as the applied potential increases until it is saturated between 65° and 80°. The reason for the saturation is not clearly understood as of today. In any case, there exists a limitation in the contact angle change by EWOD, beyond which the higher potential can no longer decrease the contact angle any further. In addition, the Lippmann-Young's equation does not consider the proceeding of the droplet. However, the droplet is advancing by the applied voltage. In order to produce larger pressure difference and to fit the simulation conditions, the voltage 100 AC with 3K or 5K Hz is used in the experiments. If a large voltage (> 110V) is applied to droplet, it will cause hydrolysis easier. Due to the limitation of microcontroller, the offset of voltage is set to 50V.

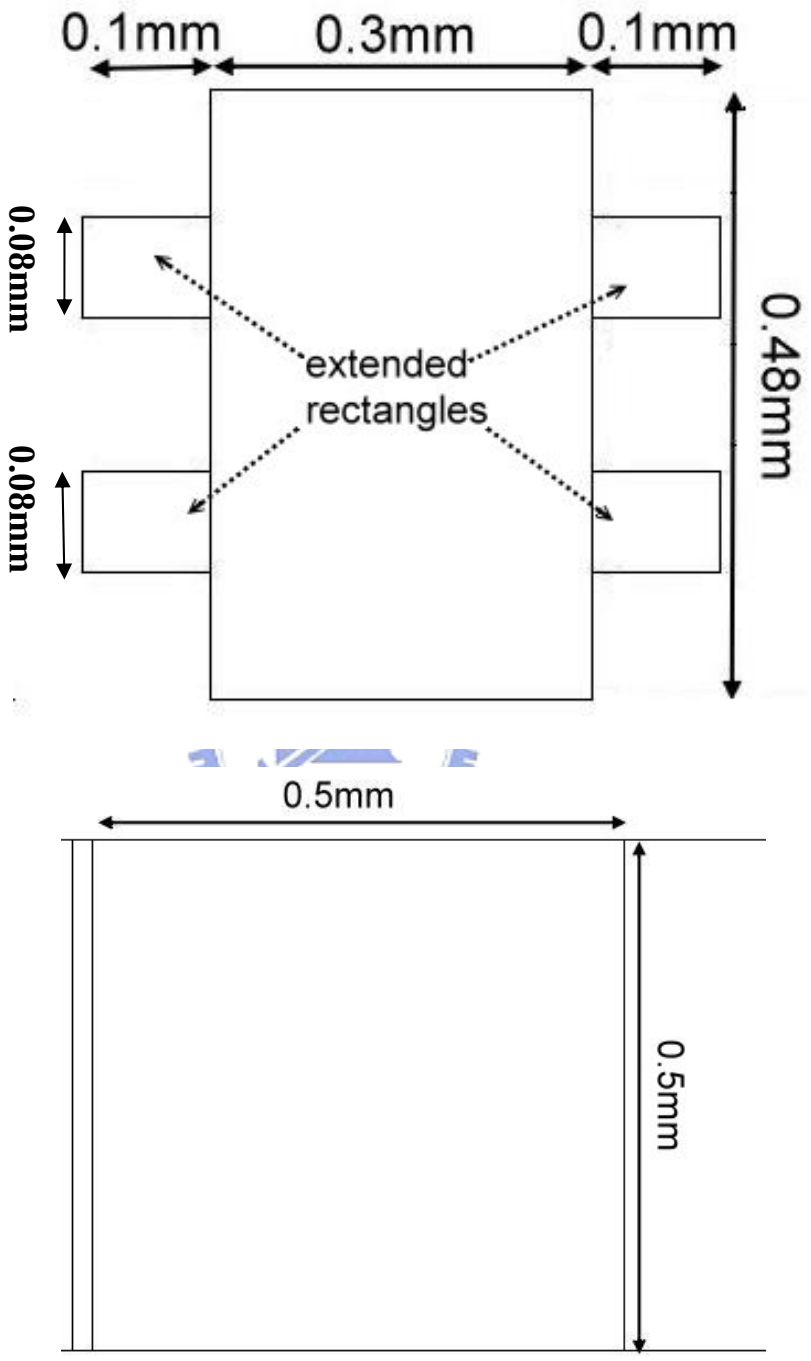

Fig. 3-1 Difference between interdigitated and square electrodes

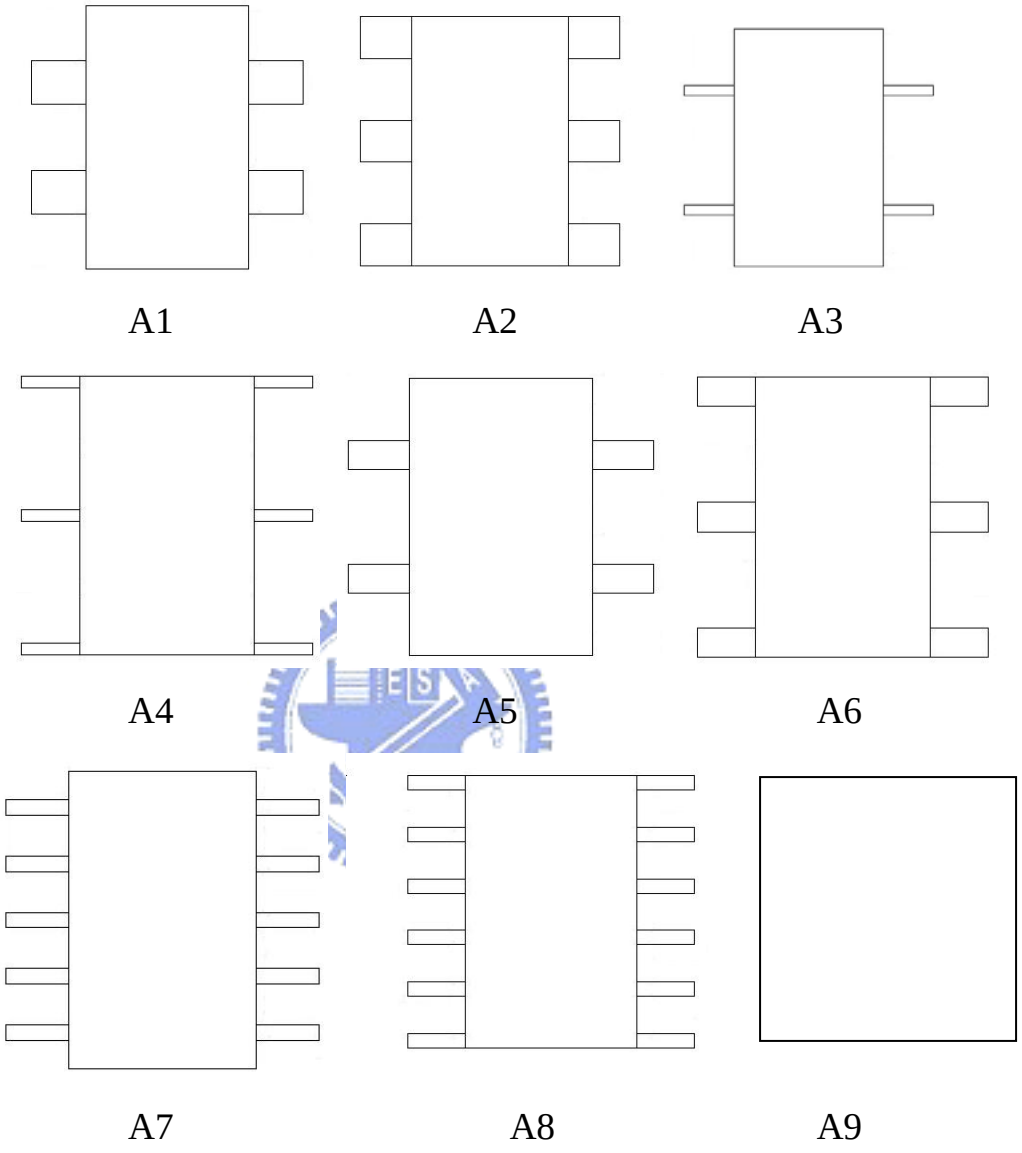

Fig. 3-2 Different shapes of electrode

Fig. 3-3 Array of different electrodes for one-dimension

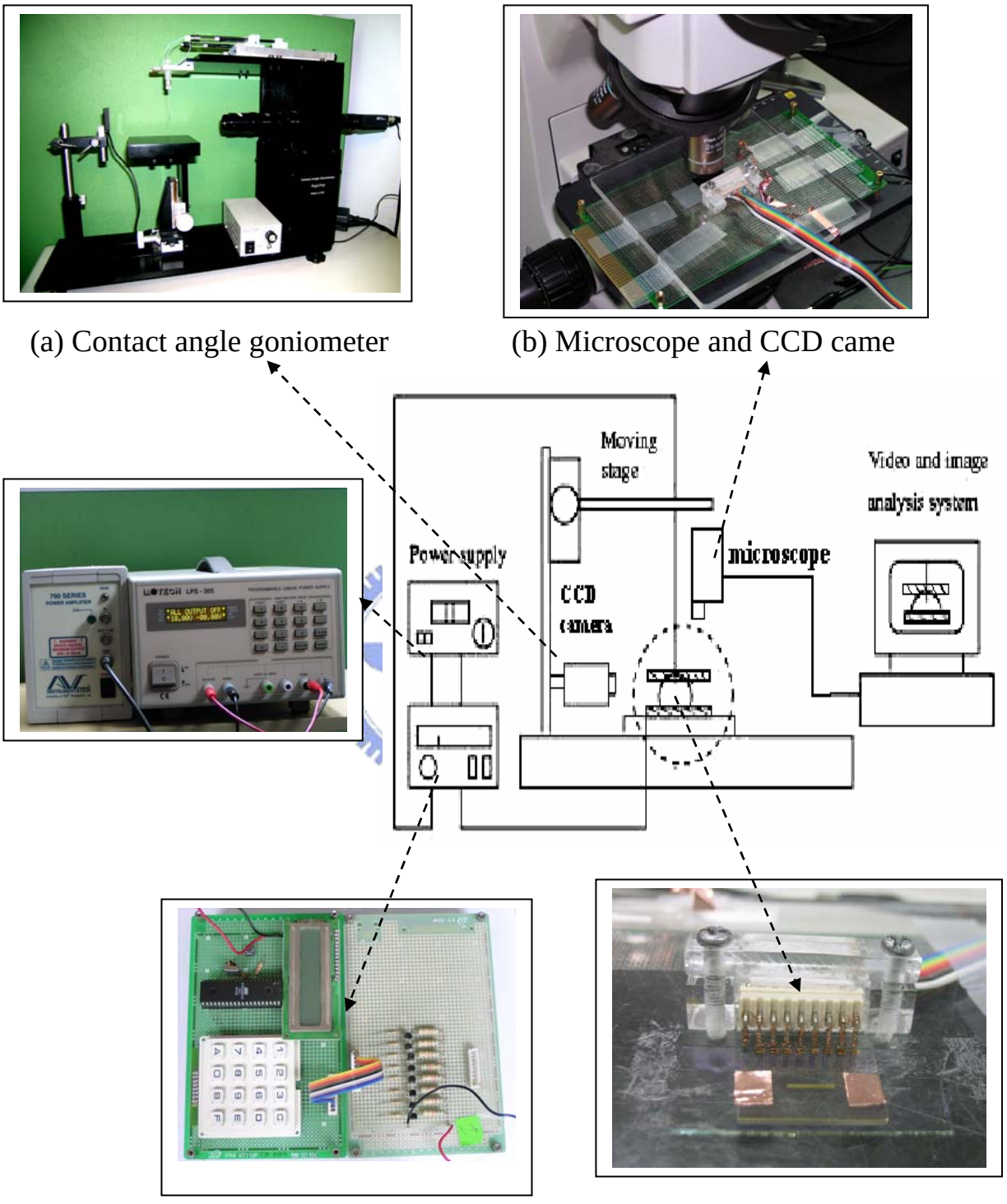

(a) Contact angle goniometer (b) Microscope and CCD came

(c) Controlled circuit (d) EWOD device

Fig. 3-4 Illustration of experiment equipments

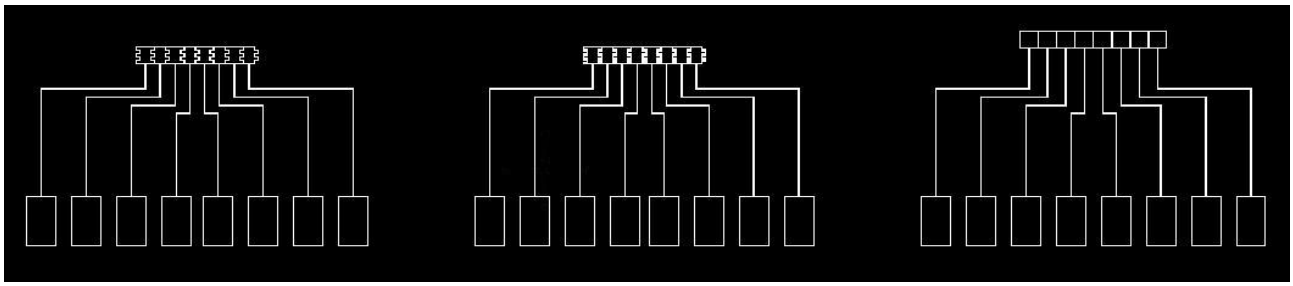

(a)

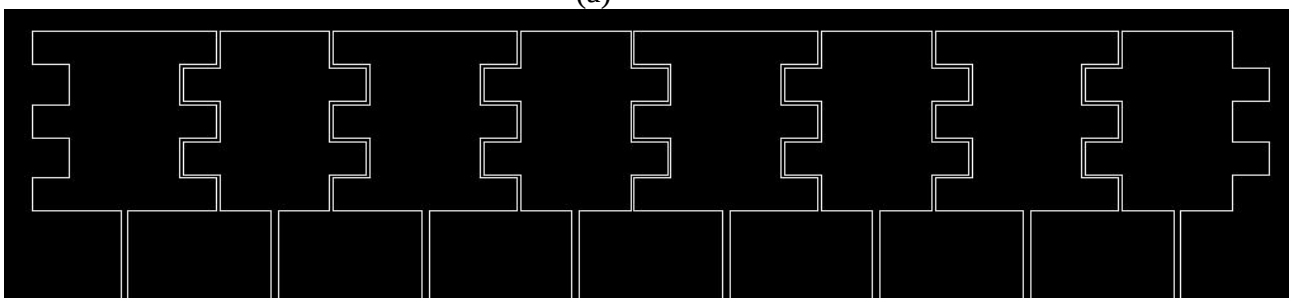

(b)

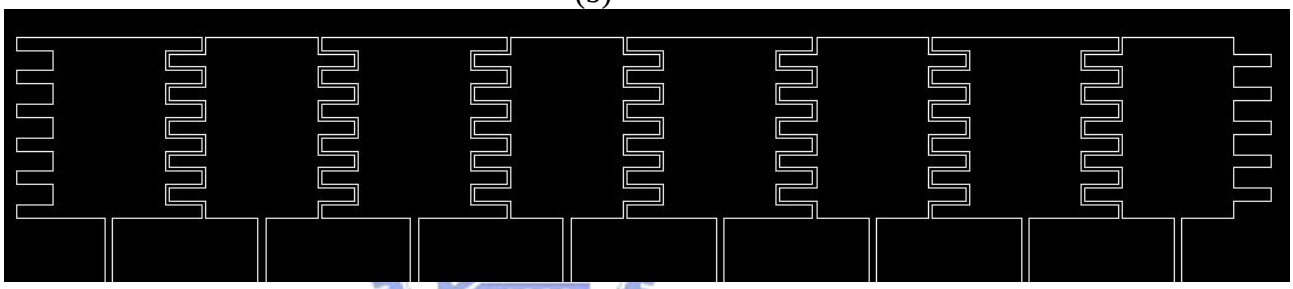

(c)

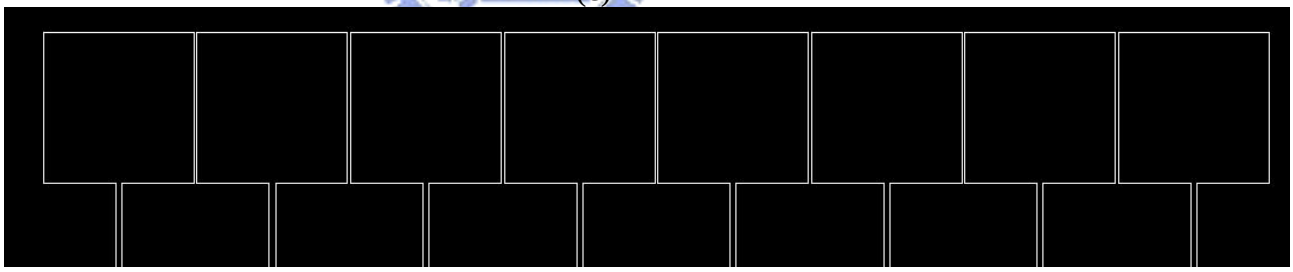

(d)

Fig. 3-5 (a) The pattern of 1-D photolithographic mask; (b)(c)(d) The pattern of pictures of EWOD control electrodes

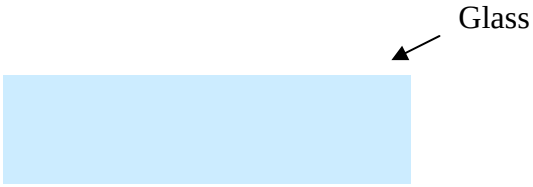

（a）Acid washing

（b）Metal deposition (Cr/Au)

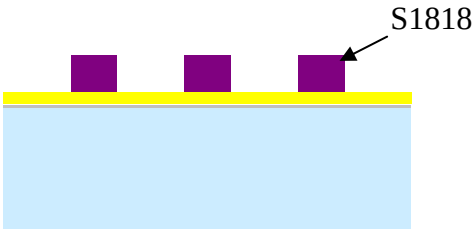

(c) Photolithography (EWOD pattern)

(d) Ache-down (Au/Cr)

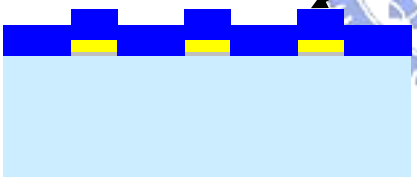

(e) Nitride deposition

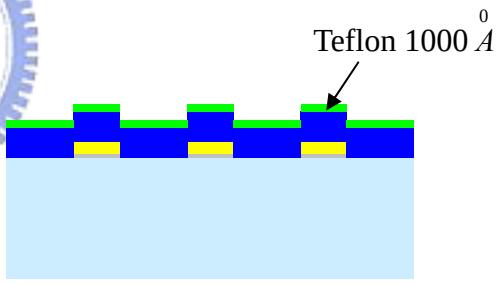

(f) Spin coat Teflon

(Ⅰ) Glass substrate process

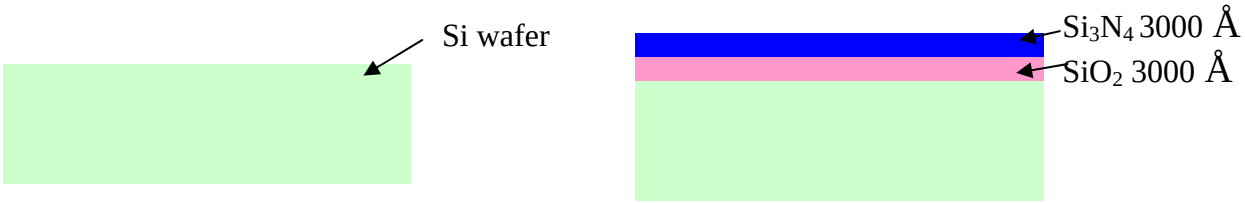

（a）MRCA (Modified RCA Clean)　　（b）SiO_2 and SiNx deposition

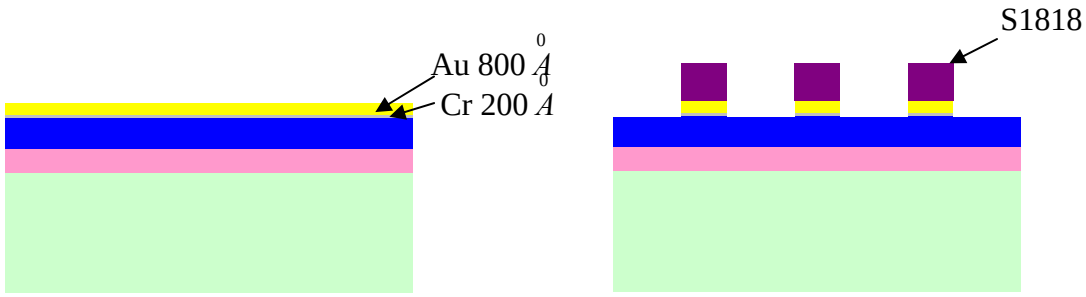

（c）Metal deposition (Cr/Au)　　(d) Photolithography (EWOD pattern)

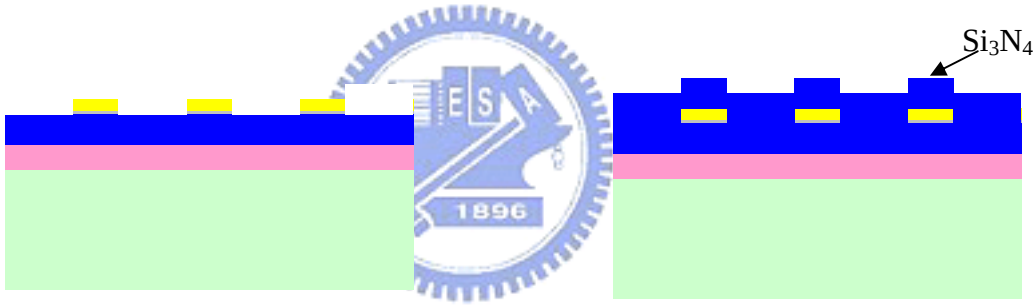

(e)　Ache-down (Au/Cr)　　(f) Nitride deposition

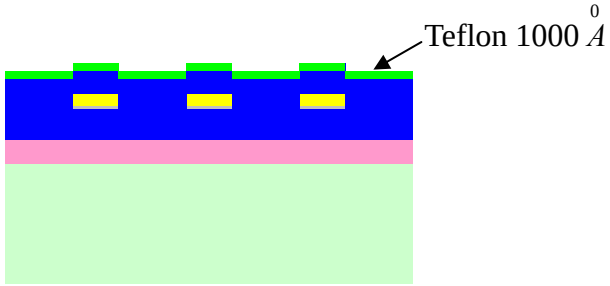

(g)　Spin coat Teflon

（Ⅱ）Silicon wafer substrate process

Fig. 3-6 Illustration of EWOD process

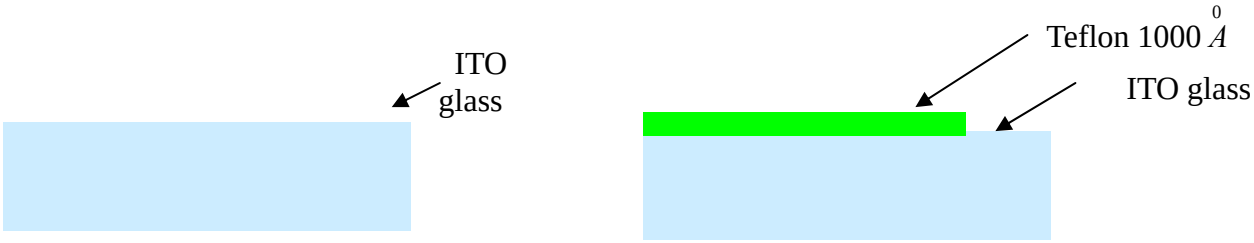

(a) ITO glass (b) Spin coat Teflon

Fig. 3-7 Illustration of top plate process

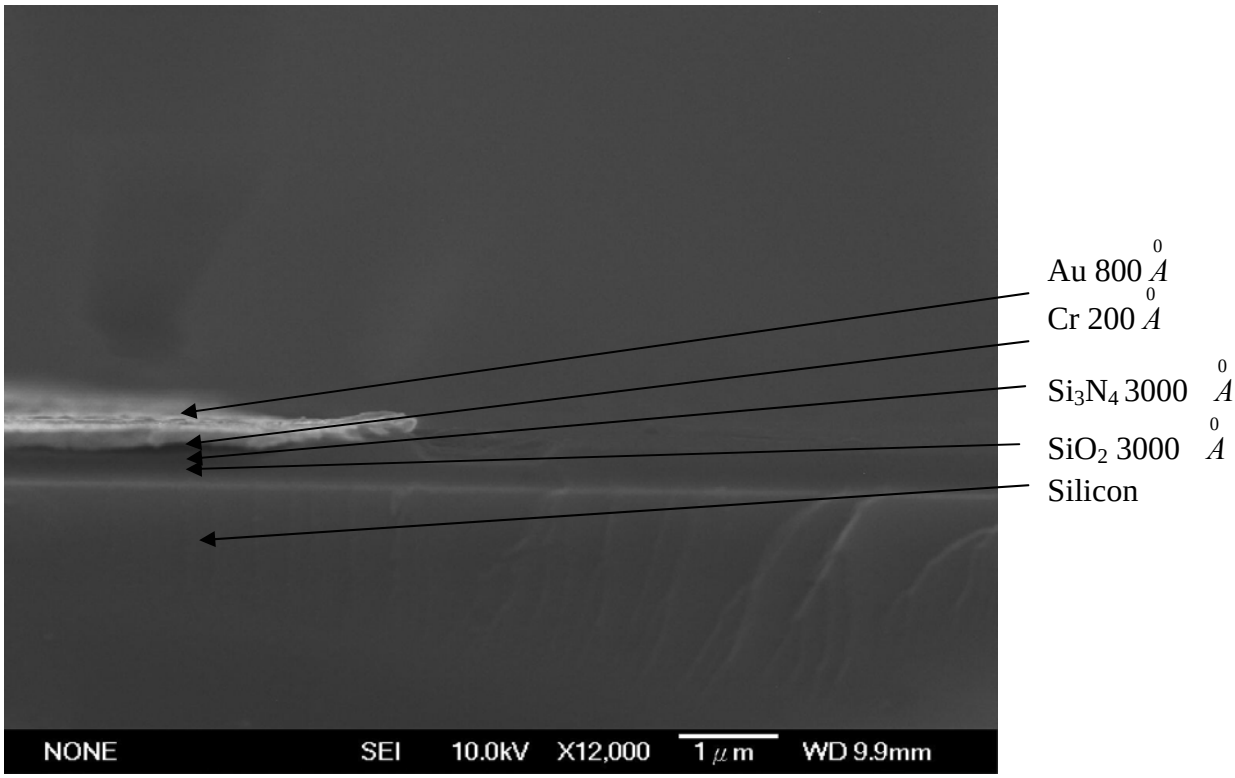

Fig. 3-8 The SEM photo of EWOD device

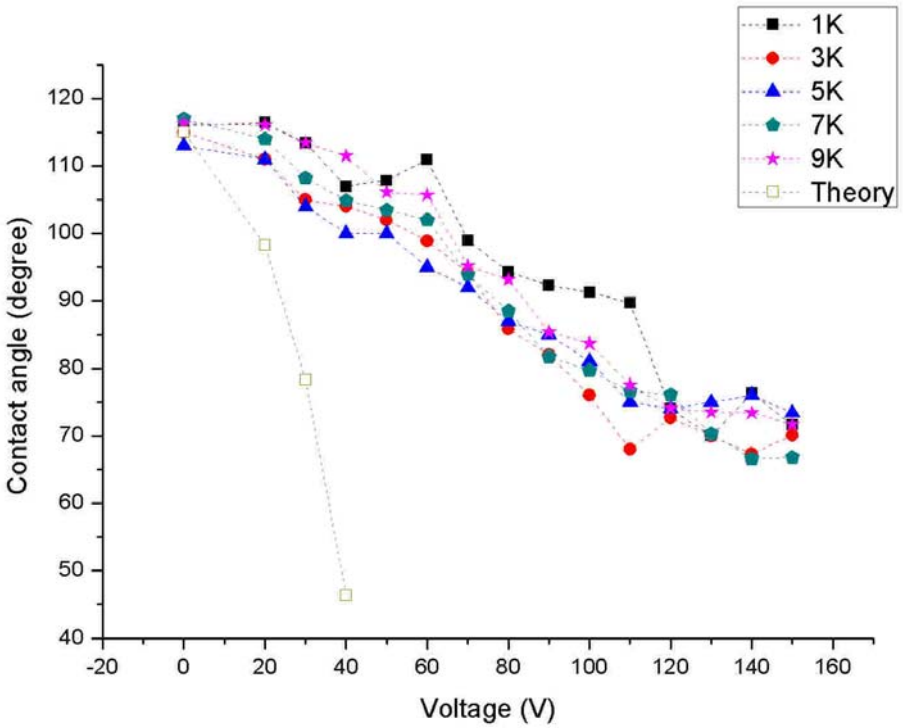

Fig. 3-9 Measurement of contact angle

CHPATER 4

RESULTS AND DISCUSSION

In this chapter, it will firstly present the simulation results that show the variations of droplet shapes under different pressure due to the electrode arrangement, the mean moving velocity of droplet and the time needed from one pattern to another while droplet is in the moving or cutting state. For experiments, it presents that a nano-liter droplets is created by different designs of square-, interdigiated- (2323) and interdigitated-electrode (5656). Finally, a comparison between numerical and experimental results for moving droplet is given.

4.1 Simulation

4.1.1 Simulation parameters

The initial conditions are the droplet location, droplet volume (radius of droplet) and initial velocity of droplet. In order to further simplify the problem, it assumes that the droplet radius is fixed at 0.3 mm for each simulation case. Because the channel height is one of the varying parameters, the resultant droplet volume ($\pi r^2 \times h$) is also changed. The corresponding values are list in Table 4-1.

Table 4-1 Volume of droplet (radius is 0.3 mm)

Channel height (h; μm)	20	35	70
Volume (nl)	5.655	9.896	19.792

Boundary conditions are the contact angles, which were obtained by experimental measurements under applied voltage. Other properties, which

are listed in Table 4-2, are composed of the gap between adjacent patterns, surface tension, gas viscosity, gas density, liquid viscosity and liquid density. In this study, the varying parameters are the channel height and the arrangement of electrodes, which were discussed briefly in the previous section. Consequently, the droplet location in Z direction in Table 4-2 is a function of channel height. The arrangement of electrodes was described in last chapter.

Table 4-2 Simulation properties

droplet location (m)	X=1.5E-4, Y=2.4E-4, Z=variable, 1E-5, 1.75E-5 and 3.5E-5
radius of droplet (m)	3E-4
initial velocity of droplet (m/s)	Vx=0, Vy=0 and Vz=0
contact angle	$80°$ (wettability); $115°$ (non wettability)
electrode size (mm^2)	0.5 X 0.48 (2323) 0.5 X 0.475 (5656) 0.5 X 0.5 (square)
main electrode area (mm^2)	0.144
channel height (μm)	Variable (20, 35 and 70)
gap of adjacent patterns (μm)	20
surface tension (N/m)	0.719
gas viscosity (air) ($Kg/m \cdot s$)	1.846E-5
gas density (air) (Kg/m^3)	1.1614
liquid viscosity (DI water) ($Kg/m \cdot s$)	8.9E-4
liquid density (DI water) (Kg/m^3)	998

In this work, 16 simulation cases, which are based on the combinations of newly designed electrodes mentioned in Section 3-1, for both droplet moving and cutting. They are discussed as follows.

4.1.2 Droplet moving

In this section, the resultant mean velocities ($\overline{V_1}$) and pressure differences (ΔP_1) for each case are presented in Table 4-3 while the droplet moves among adjacent electrodes. In this table, “a” represents the area sum of the extended rectangles and “A” total electrode area, whose representations can be seen graphically in Fig. 4-1. P1 is the initial pressure, P2 the instantaneous pressure as droplet starts to move and P3 the steady pressure as the droplet finish the movement. T and W are the time of moving among adjacent electrodes and the width of extended rectangle, respectively.

Table 4-3 16 cases of droplet moving simulations

Case	Arrangement	Channel Height(μm)	a (mm^2)	A (mm^2)	$\overline{V_1}$ (mm/s)	T (s)	P_1 (pa)	P_2 (pa)	P_3 (pa)	ΔP_1 (pa)
1	A2A1A2 W= 80 μm (323)	20	a1=0.016	A1=0.176	13.291	0.0316	1896	1023	1755	873
2		35	0.016	0.176	21.032	0.01997	1145	695	1063	450
3		70	0.016	0.176	29.207	0.01438	638	332	660	306
4	A1A2A1 W= 80 μm (232)	20	a2=0.024	A2=0.192	10.574	0.03972	1938	1220	2325	718
5		35	0.024	0.192	23.783	0.01766	1261	661	996	600
6		70	0.024	0.192	31.297	0.01342	706	451	615	255
7	A4A3A4 W=20 μm (323)	35	a3=0.004	A3=0.152	12.675	0.03314	802	660	1007	142
8	A3A4A3 W=20 μm (232)	35	a4=0.006	A4=0.156	12.939	0.03246	969	729	1017	240
9	A6A5A6 W= 50 μm (323)	35	a5=0.01	A5=0.154	18.111	0.02319	793	508	1067	285
10	A5A6A5 W= 50 μm (232)	35	a6=0.015	A6=0.174	22.913	0.01833	788	502	937	286
11	A8A7A8 W= 25 μm (656)	20	a7=0.0125	A7=0.1675	15.453	0.02718	1314	587	1758	650
12		35	0.0125	0.1675	18.182	0.02310	791	345	1049	446
13	A7A8A7 W= 25 μm (565)	20	a8=0.015	A8=0.1725	11.542	0.03639	1319	675	1720	644
14		35	0.015	0.1725	21.000	0.0200	794	341	1900	453
15	A9A9A9 (square)	20	0	A9=0.2500	9.614	0.05409	1718	1162	1339	556
16		35	0	0.2500	11.361	0.04577	894	702	1057	192

Figure 4-2 shows moving droplet shape at 0.0076805s from the top view for case 1 (channel height = 20 μm) together with the instantaneous velocity and pressure distributions at the middle plane. Note that the colored part is the wetting area, where the voltage is applied by electrode to generate the driving force for droplet moving. The dash lines represent the locations of head and tail interface (between liquid and gas), respectively. It can be seen that the minimum droplet velocity occurs at the tail interface whereas the maximum one is in the middle part, where an electrode wetting is under the way, instead of the head interface. It indicates that the front part of droplet is decelerated because the droplet head is going to stop due to no wetting as the next electrode is shut down at that instant. On the other hand, the rear part is accelerated since this part is subjecting to an electrode wetting.

The two concave gas velocity profiles just ahead of the head interface and behind the tail interface are resulted from the continuity condition with a sudden density change between two phases. The phenomenon implies that the droplet head pushes the air ahead of it and the tail drags the air behind it. Because the air is stagnant away from the droplet, this explains why air velocity profiles exhibit the concave shapes.

It can be seen that the largest pressure inside droplet occurs adjacent to the tail whereas the smallest one is at head. It indicates that the front part of droplet is in hydrophilic area and the rear one is in hydrophobic area (see Fig. 4-2). Because the front half part of droplet is in the hydrophilic area, the pressure between liquid and gas decreases. However, the droplet can move forward due to pressure gradient between head and tail.

Figure 4-3 shows head and tail pressures and velocities of droplet as a function of time for case 1. Remind that the head and tail are at the locations mentioned in Fig. 4-2. The time history is divided into three regimes, such

as I, II and III for interpretation. In regime I, it is from when the droplet starts to move to the instant when its head touches the electrode without voltage (no wetting; position 1). Regime II, the droplet head moves from the position 1 to position 2, where the droplet is moved due to the inertia from previous wetting area. Regime III, the droplet head moves from the position 2 to position 3, where the droplet stops to move completely.

It can be seen that the velocity of droplet head increases with a decrease of pressure from 0.000284s to 0.00386s, indicating that the droplet starts moving into the electrode with applied voltage. From 0.00386s to 0.006583s, it shows the opposite trend that the head velocity decreases with a rise of pressure, implying that the droplet tail is dragged by head to cause itself to slow down. However, the head pressure of droplet is smaller than that of tail in the regime I. A sudden peak occurs for tail velocity at 0.004967s, it is because that the resistance exerted by the plates initially retards the movement of droplet tail as the droplet head starts to move when electrode wetting is on. When the momentum of the front part of droplet is strong enough to overcome the drag force, it cause the tail to move forward suddenly then slow down by the hitting the front part of droplet that leads to velocity peak. At the 0.008074s, a peak of head velocity appears because the head arrives at electrode without voltage, making it hard to move forward. After that, the instantaneous head velocity increases acutely again because the interface in the neighborhood of head is still moving to squeeze it to move forward suddenly.

In the regime II, the pressures of head and tail oscillate very randomly. The reason is that the middle part of droplet is still in electrode with applied voltage, therefore, it pushes the head and drags the tail to move forward. The peristalsis behavior results in the unstable head pressure and velocity of

droplet. For the tail, its velocity pattern shows stable relatively.

In regime III, all the head pressure of droplet is smaller than that of tail one, implying that the droplet stops to move. Although the head droplet is not moving, the tail droplet still moves and compresses the head one, causing the head velocity to shake.

Figure 4-4 shows the moving droplet shape at 0.004412s from the top view for case 3 (channel height = 70 μm) together with the instantaneous velocity and pressure distributions at the middle plane. Comparing Fig. 4-4 with Fig. 4-2, both droplet heads are at the same position, however, the droplet length of Fig. 4-2 is longer. It is because that the smaller channel height possesses the greater flow resistance such that it causes the droplet to move more difficultly.

Figure 4-5 shows the variations of pressures and velocities for head and tail of droplet in case 3 with time. It also can divide into three regimes, which are similar to those in Fig. 4-3. The different between Fig. 4-3 and Fig. 4-5 is no sudden peaks for pressure and velocity in Fig. 4-5. The higher channel height has the lower flow resistance, so that the droplet can move more easily and the peristalsis behavior due to the middle part of droplet which pushes the head and drags the tail to move forward is not obvious. From the both figures, the influence of flow resistance on different channel heights for droplet can be checked.

The illustrations of droplet moving for interdigitated electrodes (2323), interdigitated electrodes (5656) and square electrodes at channel height 35 μm are shown in Fig. 4-6. It is can be seen that the shape of droplet moving is influenced by electrode design and that the interdigitated electrode (2323) has the longest wetting curve in the front part of droplet, so that it has the largest pressure difference to move droplet. The droplet shapes of interdigitated

electrode (5656) and square electrode are similar while droplet starts to move, because the numbers of extended rectangle for interdigitated electrode is too much and its form is like a square electrode. When droplet arrives at middle electrode, the designs of interdigitated electrode have longer wetting curve than that of square electrode. It proves that the design of interdigitated electrode brings function into full play.

4.1.2.1 Comparison between the interdigitated electrodes and square electrodes

Firstly, it needs to prove the interdigitated electrode can generate a greater pressure difference than square electrodes. Therefore, case-5, case-14 and case-16 in Table 4-3 are used to make a comparison. The curve of droplet touching the next electrode is shown in Fig. 4-7, which the touching length of interdigitated electrode (2323) is longer than others. These cases have the same channel height ($35\mu m$). The design of interdigitated electrodes has another advantage that the droplet can occupy the more area of adjacent electrode while moving to next electrode, as shown in Fig. 4-8. Observably, the pressure difference of case-05 and case-14 is larger than that of case-16. The same results are also found in the groups of (case-1, 15), (case-4, 15) (case-11, 15), (case-14, 15) (case-2, 5), (case-5, 7), (case-5, 8), (case-5, 10), and (case-5, 12), therefore, it can conclude that the new electrode is meaningful.

4.1.2.2 Same arrangement of electrode with different channel height

Case-4, -5 and -6 are in the same arrangement of electrode but with

different channel height. The gap of case-1 is $20\mu m$, case-2 $35\mu m$ and case-3 $70\mu m$, respectively. It can be seen that the pressure difference increases with the decrease of channel height, as shown in Table 4-4. The reason is that, the resultant droplet volume is decreased, the cohesion increased, consequently, and the drag of droplet is increased as the channel height becomes smaller. Therefore, it needs more pressure difference to drive the droplet. From Eq. (2.22), $\Delta P = \frac{1}{2}\frac{\varepsilon_0 \varepsilon_r V^2}{h}$, it can find that ΔP is proportional to $\frac{1}{h}$ if the shape of electrode and the voltage are kept the same. The relationship of $\Delta P \propto \frac{1}{h}$ can demonstrates that these simulation results are good enough, since the three cases (group (case-4, -5, -6), (case-11, -12), (case-13, -14) and (case-15, 16)) tend to exhibit the same phenomenon, which the pressure difference is increased as the channel height decreases. However, the droplet might stop moving in the experiment as the channel height so small that the drag is probably larger than the driving force. The drag is including particle, uneven surface of device, air drag and much more. But larger pressure difference can be generated by increasing voltage, which overcomes the drag force, causing the droplet to move. Therefore, it indicates that how to choose a suitable channel height is an important problem.

Table 4-4 Pressure difference vs. channel height

Channel height(μm)	20 (case-1)	35 (case-2)	70 (case-3)
ΔP (Pa)	654	345	127

4.1.2.3 Same number of extended rectangle with different width of extended rectangle

Case-5, -8 and -10 have the same number of electrode rectangle but with different width of extended rectangle. The purpose is to investigate whether the pressure difference is changed by the area of extended rectangle. The width of extended rectangle of case-8 is $20\mu m$, case-10 is $50\mu m$ and case-5 is $80\mu m$. The contact curve to adjacent electrode is shown in Fig. 4-9 and Fig. 4-10. From the Table 4-3, case-5, which has the biggest area of electrode, produces the greatest pressure difference. It can conclude that the more area of electrode is touched by droplet, the larger pressure difference is caused. Figure 4-11 demonstrates such trend; therefore, it is better to choose the big area of electrode in experiment.

4.1.2.4 Same total area of extended rectangle with different number of extended rectangles

To compare case-10 with case-14, they have the same total area of extended rectangle but the numbers of rectangles are different. Case-10 has six extended rectangles whereas case-14 has twelve. From the Table 4-3, the pressure differences for both cases are different. It proves that the pressure difference is changed by number of extended rectangles, even if both cases have the same area of electrode. The more numbers of extended rectangles has larger pressure difference, but it can make hydrolysis easily. However, we should select similar pattern of case-10 in the corresponding experiment, because a simpler pattern is helpful for the device to be easily manufactured.

Table 4-5 Pressure difference vs. the same contact curve (area)

Channel height(μm)	35 (case-10)	35 (case-14)
ΔP_1 (Pa)	286	453

4.1.3 Cutting

In this section, the resultant mean velocities ($\overline{V}_2$) and pressure differences (ΔP_2) for each case are presented in Table 4-6 while the droplet cuts both adjacent electrodes. In this table, “a” “W” and “A” whose means are the same above. P4 is the steady pressure as the droplet finishes the cutting. W is the width of extended rectangle. The illustration of simulations for cutting is shown in Fig. 4-12.

Table 4-6 16 cases of cutting

Case	Arrangement	Channel Height(μm)	a (mm^2)	A (mm^2)	$\overline{V}_2$ (mm/s)	T (s)	P_3 (pa)	P_4 (pa)	ΔP_2 (pa)
1	A2A1A2 W= 80 μm (323)	20	a2=20.024	A2=0.192	38.778	0.010831	1755	1252	503
2		35	0.024	0.192	42.879	0.009795	1063	720	343
3		70	0.024	0.192	0	0	660	491	169
4	A1A2A1 W= 80 μm (232)	20	a2=0.016	A2=0.176	22.997	0.018263	2325	1756	569
5		35	0.016	0.176	42.936	0.009782	996	557	439
6		70	0.016	0.176	0	0	615	435	180
7	A4A3A4 W= 20 μm (323)	35	a4=0.006	A4=0.156	28.260	0.014862	1007	902	105
8	A3A4A3 W= 20 μm (232)	35	a3=0.004	A3=0.152	28.542	0.014715	1017	889	128
9	A6A5A6 W= 50 μm (323)	35	a6=0.015	A6=0.174	42.735	0.009828	1017	707	310
10	A5A6A5 W= 50 μm (232)	35	a5=0.01	A5=0.164	49.657	0.008458	937	694	243
11	A8A7A8 W= 25 μm (656)	20	a8=0.015	A8=0.1725	45.952	0.00914	1758	1431	372
12		35	0.015	0.1725	40.280	0.010427	1049	695	354
13	A7A8A7 W= 25 μm (565)	20	a7=0.0125	A7=0.1675	43.228	0.009716	1720	1396	324
14		35	0.0125	0.1675	34.277	0.012253	1006	757	249
15	A9A9A9 (square)	20	a9=0	A9=0.2500	17.537	0.02395	1339	1124	215
16		35	0	0.2500	33.746	0.012446	1057	861	196

4.1.3.1 Channel height and cutting

According to Eq. (2.24), for square electrode and droplet placed on middle electrode, while channel height (h) is smaller than $75\mu m$, the droplet can be cut [9]. The flames of simulation are shown in Fig.4-13. The h is determined by Eq. (2.24), in which R_2 is 0.25 mm, $\cos\theta_{b2}$ is 80^0 and $\cos\theta_{b1}$ is 115^0, respectively. However, the droplet moves from left electrode to the middle and then cut the droplet apart by both adjacent electrodes. It can observe the droplet can be cut, as shown in Fig. 4-14. But the sizes of cutting droplet on left and right electrodes are different. It may result from the surface curve of droplet that occupies the left and right electrodes are the different. The droplet touches surface curve of the left electrode is larger than right electrode. Deservedly, the pressure difference of the left electrode is larger than right one.

We also make a comparison between square electrode and interdigitated electrode (2323) at channel height $70\mu m$, as shown in Fig.4-15. Unusually, interdigitated electrode (2323) is can't be cut, and it has the larger pressure difference than square electrode to cut droplet. The reason for this phenomenon is that the extended rectangle of 2323 for droplet in cutting process brings a drag force, which makes the pressure difference between droplet and air to get balance, as shown in Fig. 4-16. However, the droplet can be cut as channel height are $35\mu m$ (Fig. 4-15) and $20\mu m$. The equation (2.24) is designed for electrode of square especially, but it is not square in these interdigitated electrodes. Though the equation isn't completely suitable for interdigitated electrodes, it is still a significant parameter in these simulations. Except case-3 and case-6, the phenomenon of cutting appears in all other cases as h is $20\mu m$ or $35\mu m$. So the channel height, $20\mu m$ and

$35\mu m$, will be used in our experiments.

4.1.3.2 Comparison among different cases in cutting

Comparing Table 4-3 with Table 4-6, the similar results can be observed in cutting. The lower channel height is, the larger pressure difference is. For Case-5, -8 and -10 (Table 4-6), they have the same number of electrode rectangle but with different width of extended rectangles; there is the same result with Table 4-3 that the more width of extended rectangle will be caused larger pressure. Finally, for Case-9 and Case-12 (Table 4-6), they have the same total area of extended rectangle but difference numbers of rectangles. The result of pressure difference is alike 4-1.5 that the more numbers of extended rectangles has larger pressure difference.

Due to the numerical results of 4-1.2 and 4-1.3, it shows the interdigitated electrode (2323) can create larger pressure difference than the other designs. So the droplet can move fancily.

4.2 Experimental results

According to discussions above, the design of interdigitated electrode (2323), interdigitated electrode (5656) and square electrode are chosen to create droplet in our experiments and there are eight electrodes in our devices. The Photos of interdigitated electrode (2323) are shown in Fig. 4-17 and Fig. 4-18 which succeed in creating a droplet of 3.2~4 nano-liter surrounding by air. The channel height is $20\mu m$, applied voltage 100 V_{AC}, frequency 3K and offset 50V. There are two processes in our work to create nano-droplet. One is that droplet moves from 1st electrode to 8th and then applies voltage in 1st, 3rd, 7th and 8th electrodes. Another is to create a larger droplet and then use

cutting process to create the droplet (Fig. 4-18). Usually, the second way to create nano-liter droplet is used in interdigitated electrode (5656) and square electrode, as shown in Fig. 4-19 and Fig. 4-20. The volume of droplet, created by interdigitated electrode (5656) and square electrode, are 8.3nl and 4.5nl, respectively. In the experiments, for creating nano-liter droplet has a defect which the droplet volume just can controlled in a scope, such as 3~6 nl.

Although designs of interdigitated electrode are helpful to create nano-liter droplet, causing hydrolysis is easier than square electrode. The phenomenon, it results from applied voltage, droplet thickness and extended rectangles of interdigitated electrodes. The high voltage can hydrolyze DI water to hydrogen and oxygen, because there is a strong electrical field for droplet. In experiment, there are three channel height, $20\mu m$, $35\mu m$ and $70\mu m$. At voltage 100 V_{AC}, the droplet at channel height $20\mu m$ is easier to cause hydrolysis than the others, because the lower channel height has the strong electric field, as shown in Eq. (4-1).

$$E = \frac{V}{h} \tag{4-1}$$

Where E is electric field, applied voltage V and channel height h. However, the hydrolysis phenomenon is also affected by the numbers of extended rectangle. When it comes to the square electrodes shown in Fig. 4-21, the energy stored in the electrode-electrode capacitor is described below

$$W = \frac{1}{2} C V^2 \tag{4-2}$$

The capacitor configuration is known as a parallel-plate capacitor.

$$C = \varepsilon_0 \varepsilon_\gamma \frac{A}{d} = \varepsilon_0 \varepsilon_\gamma \frac{H \cdot L}{d} \tag{4-3}$$

“A” means the area of each electrode as the Fig. 4-22 shows. “H” is the height of electrode and L stands for the length of the electrode. d is the

separation between the electrodes. From these equations mentioned above, the energy is calculated below:

$$W = \frac{1}{2}CV^2 = 0.5 \times 1 \times 8.85 \times 10^{-12} \times \frac{0.5 \times 10^{-3} \times 600 \times 10^{-10}}{20 \times 10^{-6}} \times 100^2 = 6.6375 \times 10^{-14} w$$

And here come interdigitated electrodes (2323). According to the statement which is mentioned above, the area of the capacitor change. The Fig. 4-23 shows the interdigitated electrodes and capacitor distribution chart. By integrating the capacitor, we could find out the total capacitor is:

$$C_{total} = C_1 + C_2 + C_3 + C_4 + C_5 + C_6 + C_7 + C_8 + C_9 \cong \sum_{n=1}^{9} \varepsilon_0 \varepsilon_\gamma \frac{(L_n)}{d} = \varepsilon_0 \varepsilon_\gamma \frac{L'}{d}, L' = \sum_{n=1}^{9} L_n$$

So the energy stored in the capacitor is:

$$W = \frac{1}{2}CV^2 = 0.5 \times 1 \times 8.85 \times 10^{-12} \times \frac{0.96 \times 10^{-3} \times 600 \times 10^{-10}}{20 \times 10^{-6}} \times 100^2 = 1.2744 \times 10^{-13} w$$

As the same method, the energy stored of interdigitated electrodes (5656) is:

$$W = \frac{1}{2}CV^2 = 0.5 \times 1 \times 8.85 \times 10^{-12} \times \frac{1.44 \times 10^{-3} \times 600 \times 10^{-10}}{20 \times 10^{-6}} \times 100^2 = 1.9162 \times 10^{-13} w$$

Obviously, the energy higher than square electrodes causes hydrolysis more easily. In spite of hydrolysis, interdigitated electrodes are still helpful to create nano-liter droplet.

Table 4-7 the hydrolysis energy

Electrode design	Interdigitated (2323)	Interdigitated (5656)	Square
Energy (w)	1.2744×10^{-13}	1.9162×10^{-13}	6.6375×10^{-14}

4.3 Comparison of simulation and experiment

Figure 4-24 shows that simulation of interdigitated electrode (323) compares to experimental photos, in which the applied voltage is 100V AC, dielectric thickness (nitride) $3000\,\mathring{A}$, channel height $20\mu m$, and volume of droplet 5nl. The volumes of droplets are 4.2nl for interdigitated electrode (565) in Fig. 4-25 and 4.5nl for square electrode in Fig.4-26. The other parameters are the same as Fig. 4-24. There are a little different between experimental photos and simulation frames, it results from particles on electrodes, hydrolysis, electrodes of rough surface in experimental devices but smooth surface in simulation and etc. The devices of rough surface is caused by uneven of Au deposition, photolithography develop, dielectric layer deposition and coating Teflon layer. Because the pressure difference of droplet can't be measured in the experiments, the larger pressure difference can make droplet move faster. From the experimental photos, the droplet moving for interdigitated electrodes (2323) and interdigitated electrodes (5656) are faster than square electrodes. Because the CCD camera is 30 frames per second, it is found that the mean velocity of droplet for interdigitated electrode (2323) was 11.36 mm/s, whereas the corresponding prediction was 13.291 mm/s. For 5656 arrangement, the mean experimental and numerical velocities were 11.07 and 11.542 mm/s, respectively. As to square electrode, they were 10.49 and 9.614 mm/s, separately. It proves indirectly that the trends of simulation are accuracy. In spite of a little discrepancy between experiment and simulation, from the comparison of Fig. 4-21, Fig. 4-22 and Fig. 4-23, it is confirmed that the results of simulation have the relative accuracy.

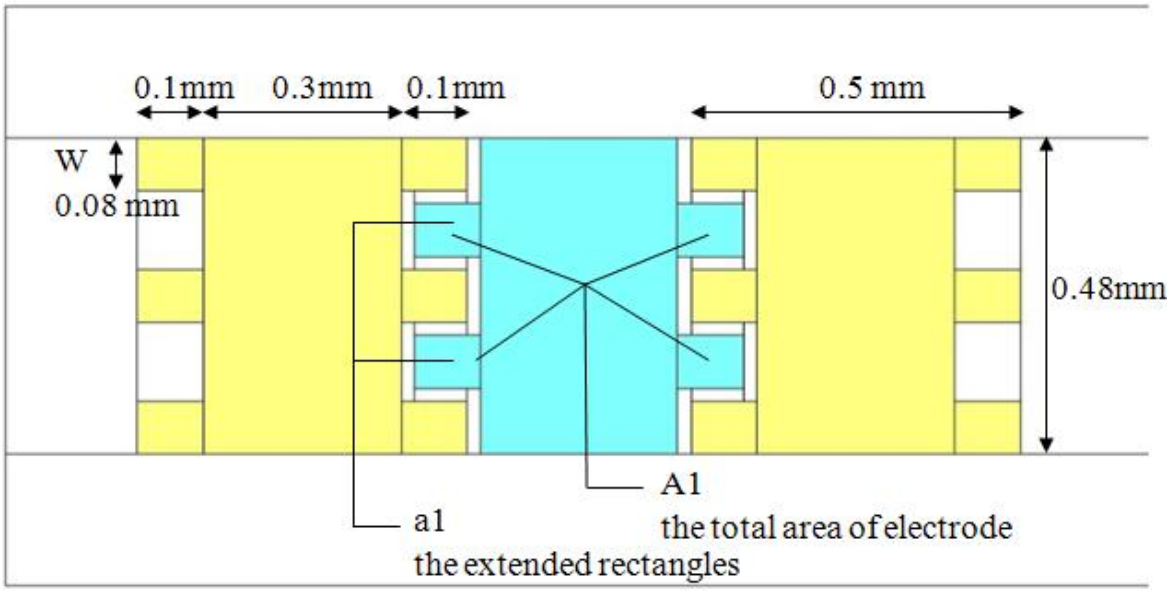

Table 4-3 15 cases of droplet moving simulations

Case	Arrangement	Channel Height(μm)	a (mm^2)	A (mm^2)	$\overline{V}_1$ (mm/s)	T (s)	P_1 (pa)	P_2 (pa)	P_3 (pa)	ΔP_1 (pa)
1	A2A1A2 W= 80 μm (323)	20	a1=0.016	A1=0.176	10.126	0.0316	1896	1023	1755	873
2		35	0.016	0.176	16.024	0.01997	1145	695	1063	450
3		70	0.016	0.176	22.253	0.01438	638	332	660	306
4	A1A2A1 W= 80 μm (232)	20	a2=0.024	A2=0.192	8.056	0.03972	1938	1220	2325	718
5		35	0.024	0.192	18.120	0.01766	1261	661	996	600
6		70	0.024	0.192	23.845	0.01342	706	451	615	255
7	A4A3A4 W=20 μm (323)	35	a3=0.004	A3=0.152	9.656	0.03314	802	660	1007	142

Fig. 4-1 Illustration of Table 4-3

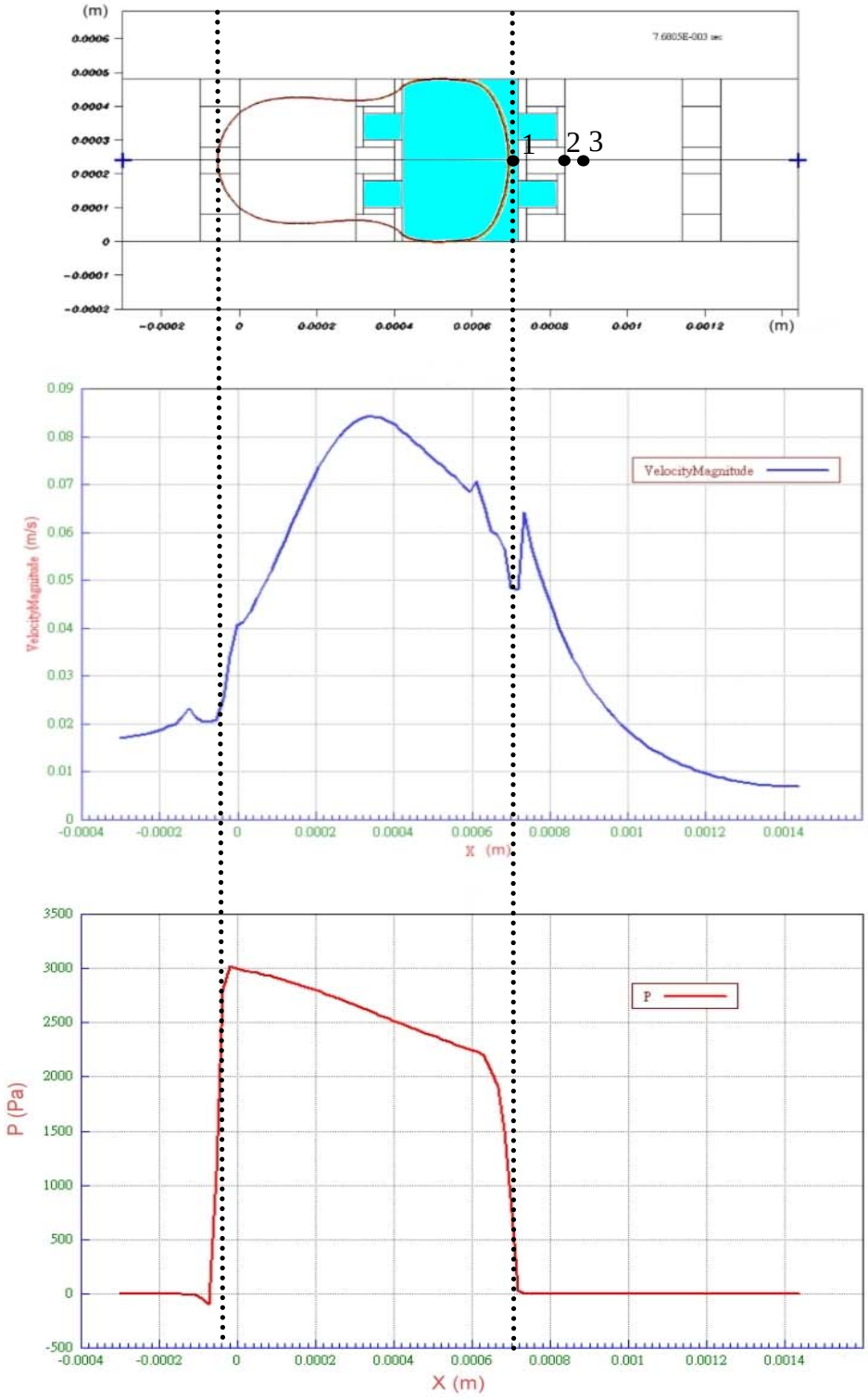

Fig. 4-2 Illustration of velocity and pressure for droplet (case 1)

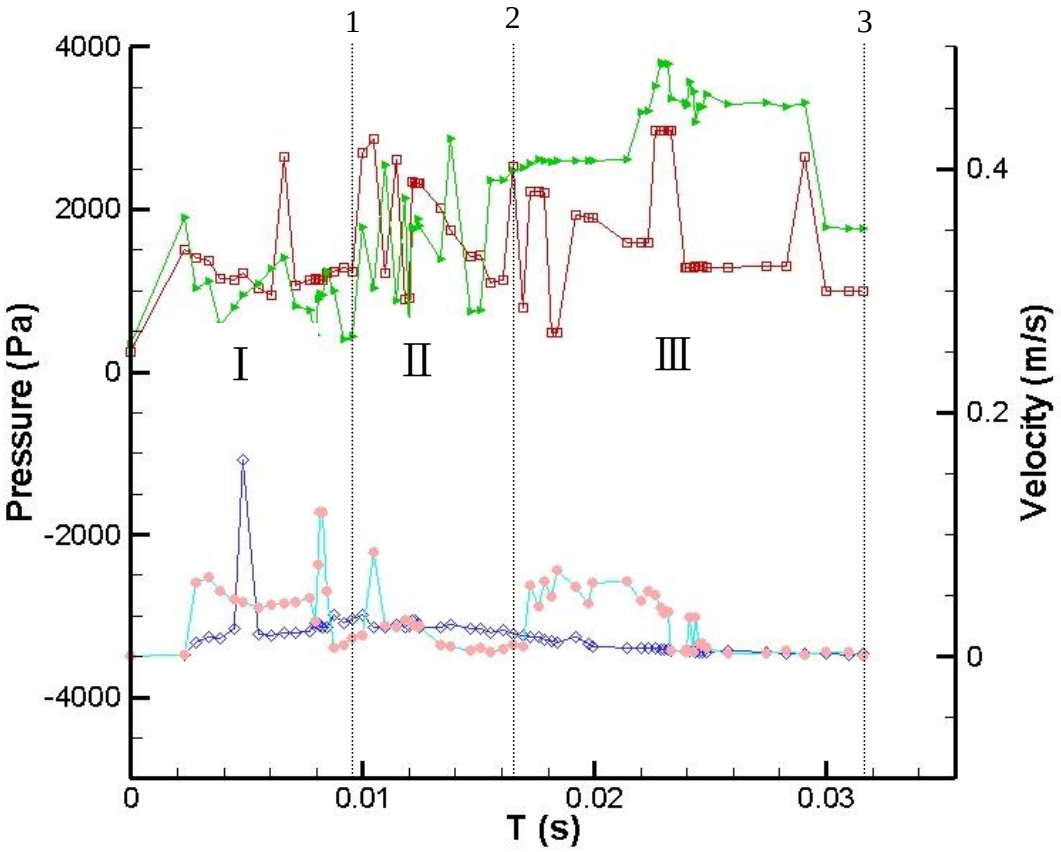

Fig. 4-3 Pressure and velocity vs. time for case 1 (triangle: pressure of head droplet; square: pressure of tail droplet; circle: velocity of droplet head; diamond: velocity of tail droplet)

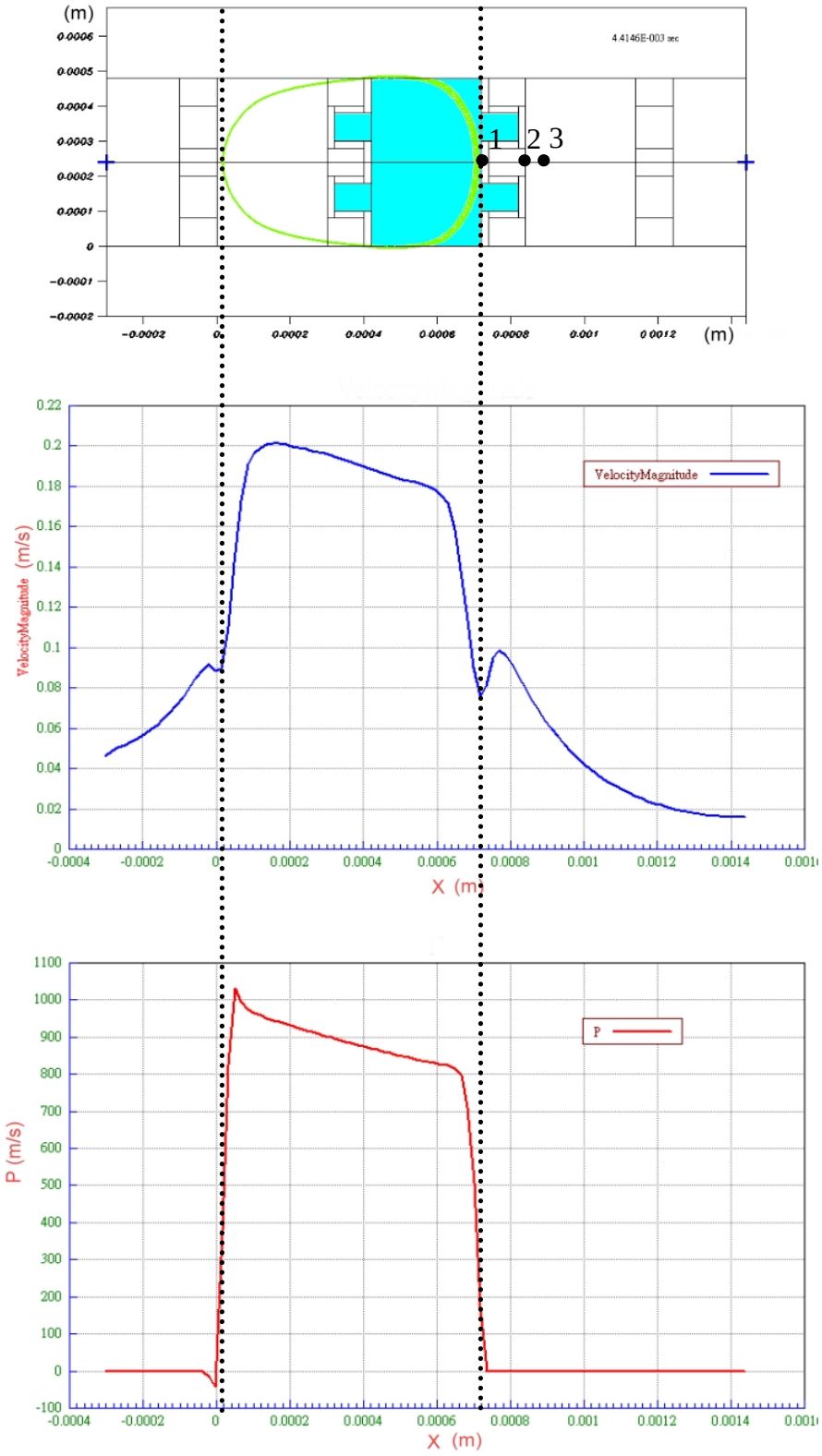

Fig. 4-4 Illustration of velocity and pressure for droplet (case 3)

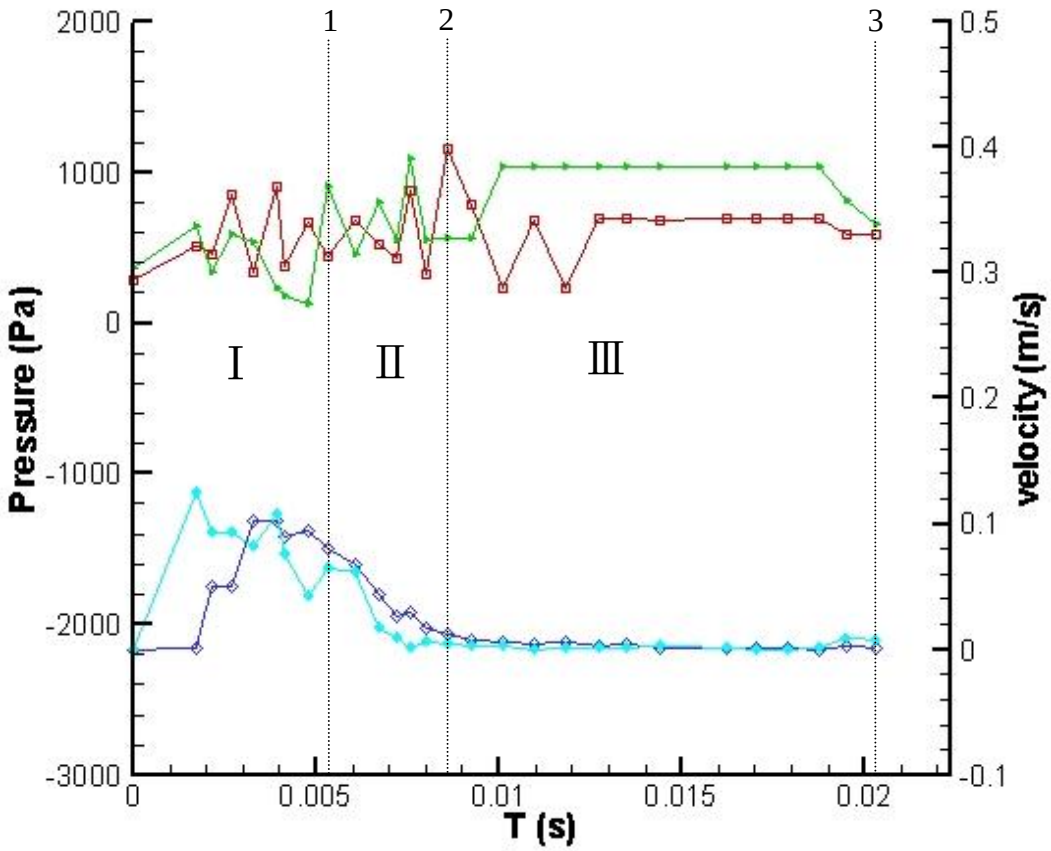

Fig. 4-5 Pressure and velocity vs. time for case 3 (triangle: pressure of head droplet; square: pressure of tail droplet; circle: velocity of droplet head; diamond: velocity of tail droplet)

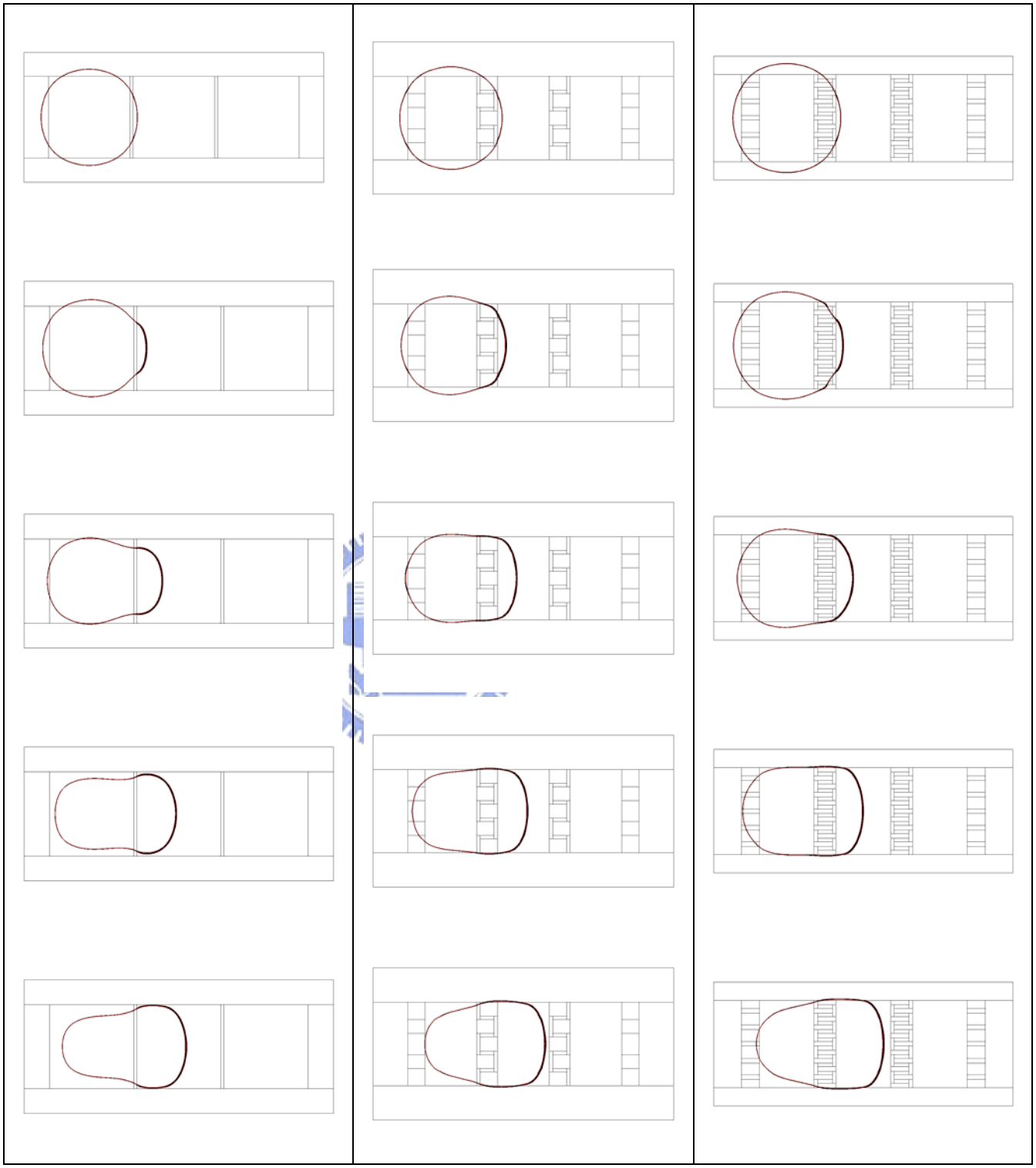

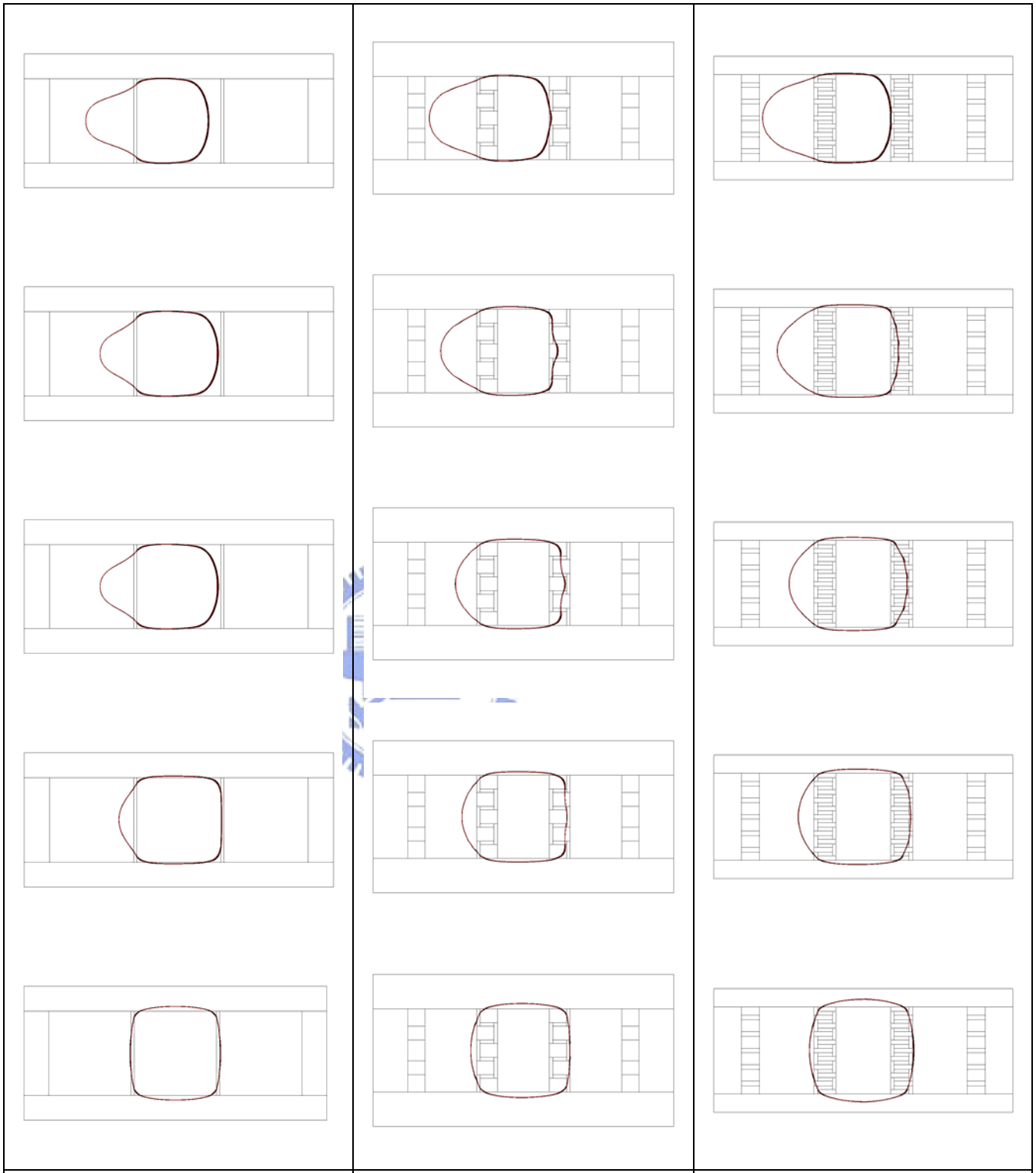

Electrode square 0.5mm X 0.5mm (case 16)	Electrode 232 0.5mm X 0.48mm (case 05)	Electrode 565 0.5mm X 0.475mm (case 14)

Fig. 4-6 Simulations of moving (channel height 35 μm)

	Channel height (35 μm)	Length of black line (mm)	Presure difference (pa)
Case-16	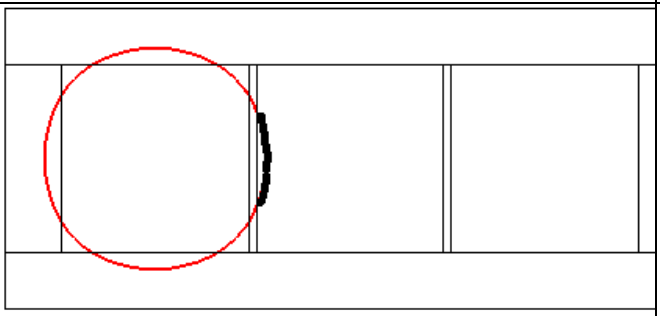	0.2513	192
Case-14	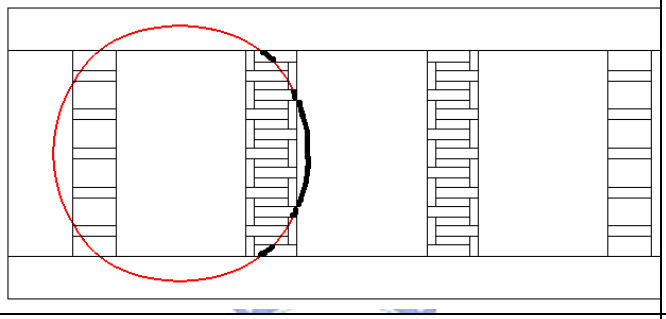	0.4032	453
Case-05	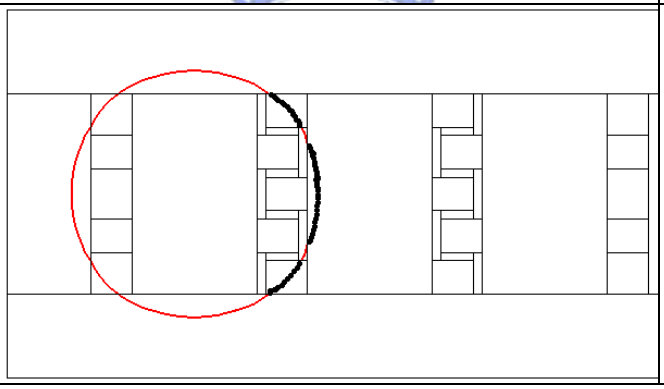	0.4765	600

Fig. 4-7 The contact length of droplet occupying adjacent electrode

	Channel height (35 μm)
Case-16	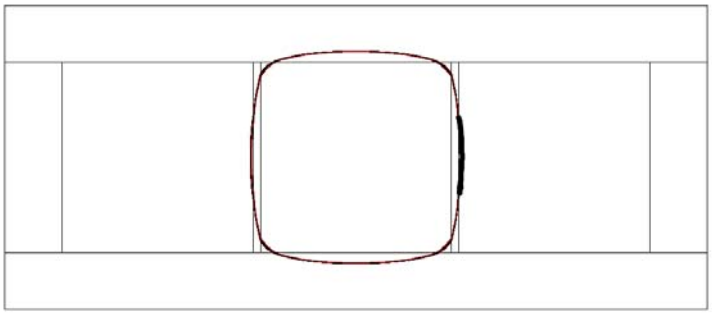
Case-14	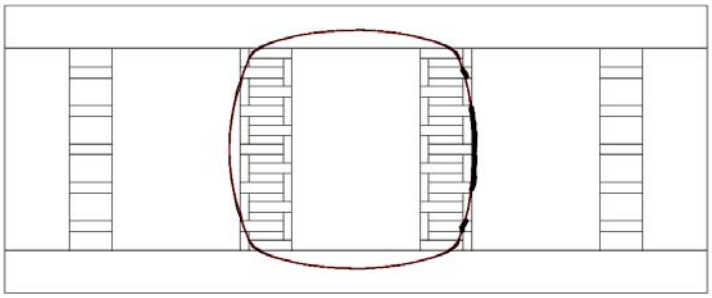
Case-05	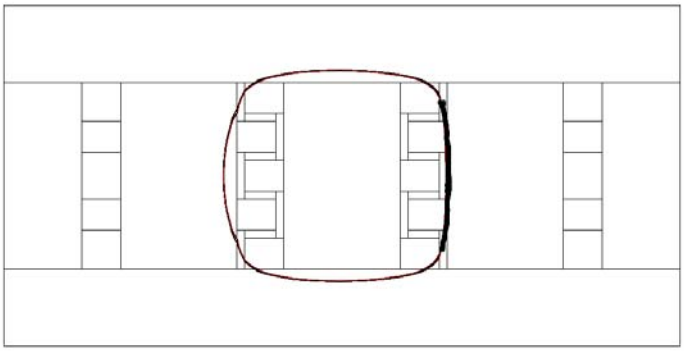

Fig. 4-8 Situation of moving droplet touching the adjacent electrode

	Channel height (35 μm)	Length of black line (mm)	Presure difference (pa)
Case-08	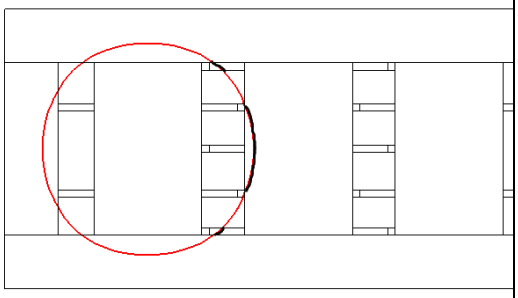	0.3089	240
Case-10	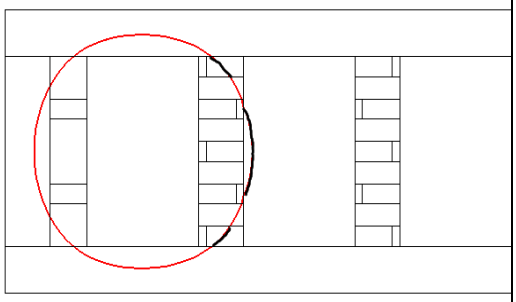	0.3718	286
Case-05	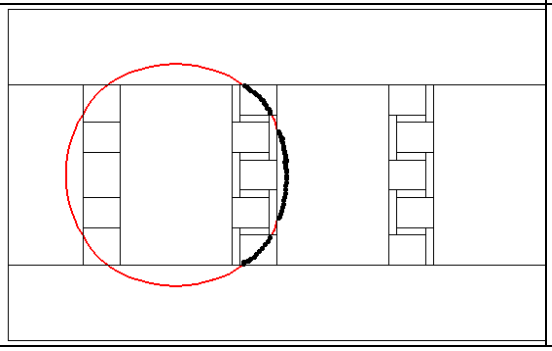	0.4765	600

Fig. 4-9 The contact length of droplet to next electrode for coae-05, 08 and 10 (Table 4-2)

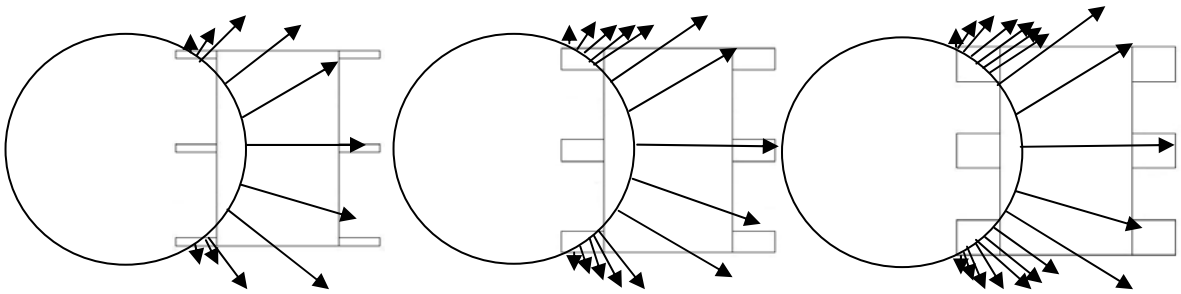

Fig. 4-10 Using tension to illustrate contact curve into adjacent electrode

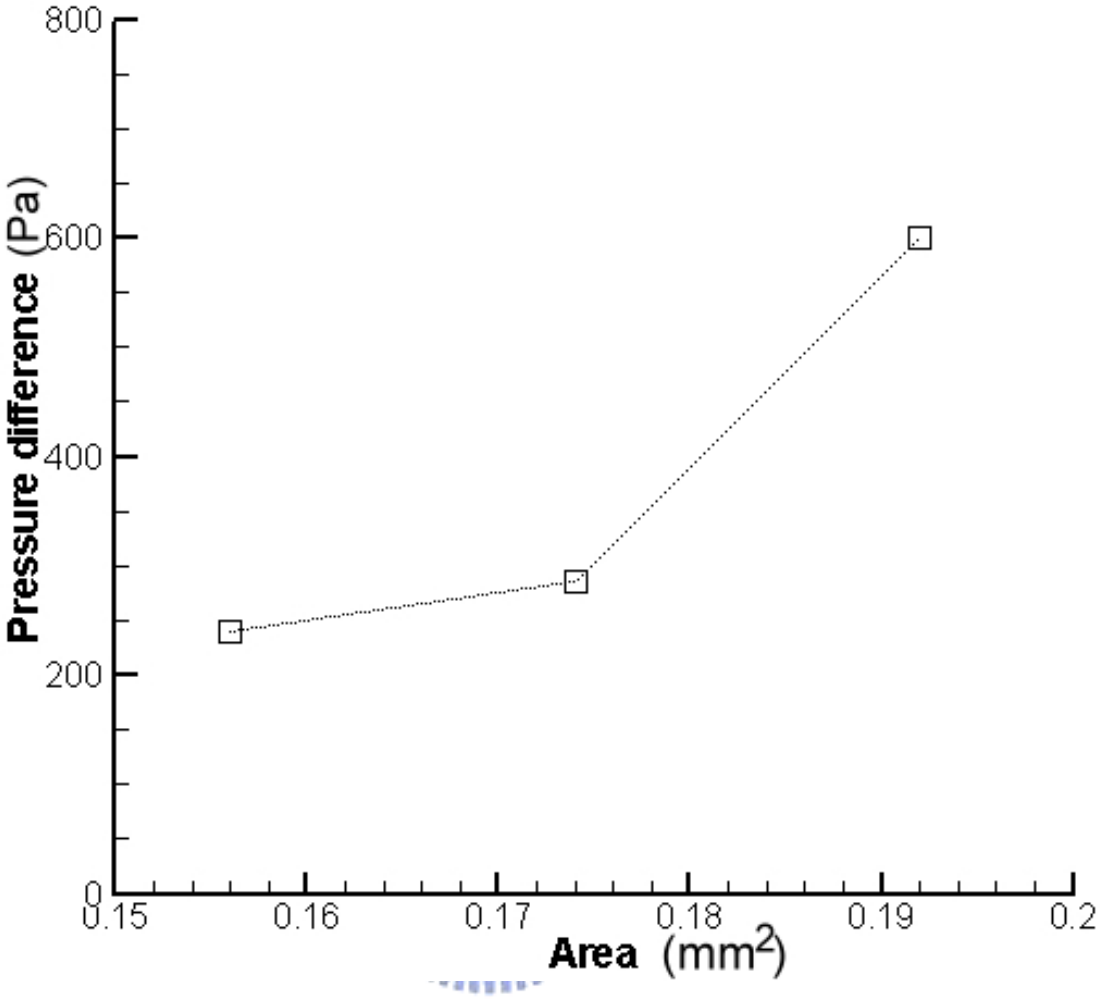

Fig. 4-11 Pressure difference increases with area of electrode

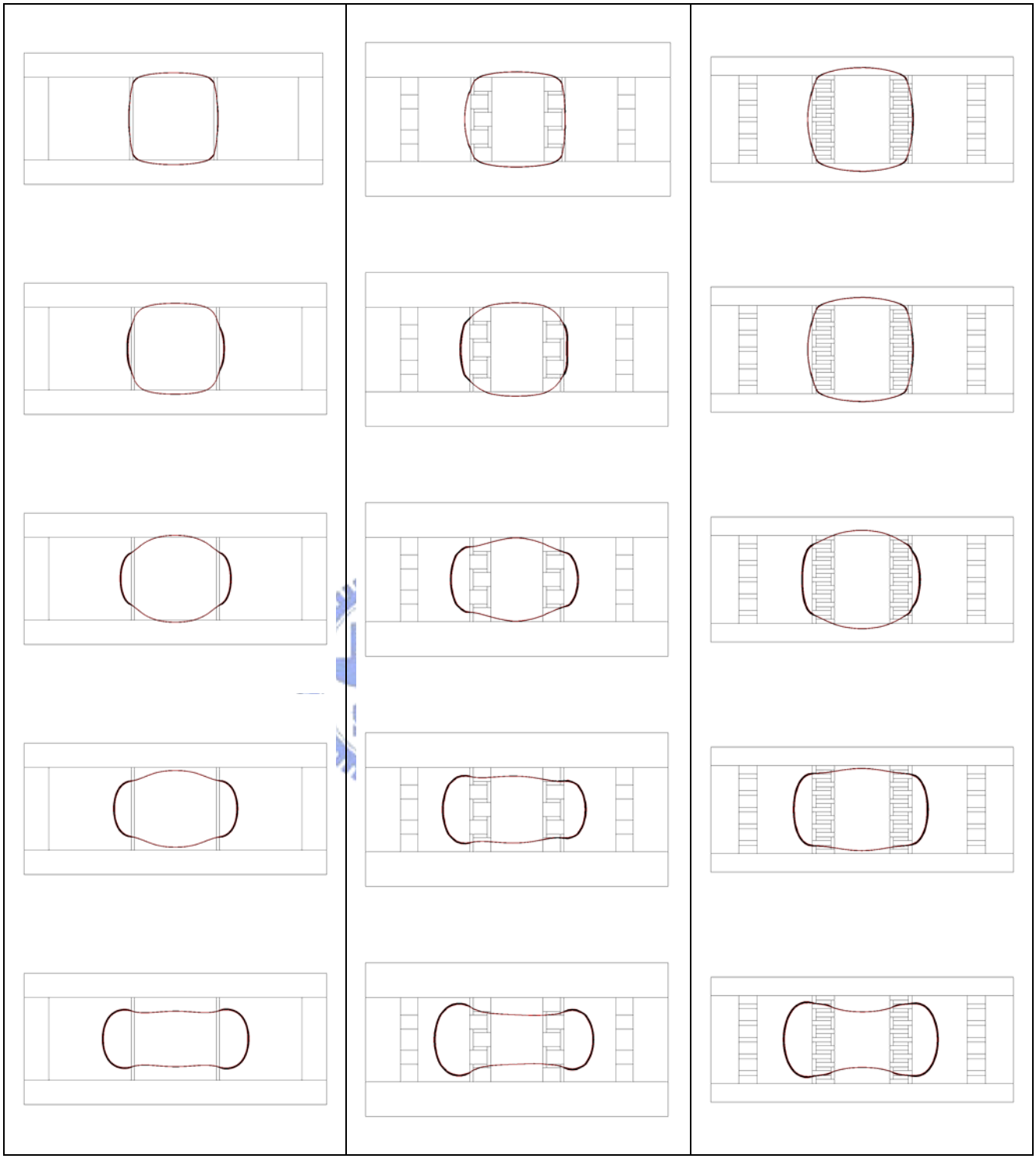

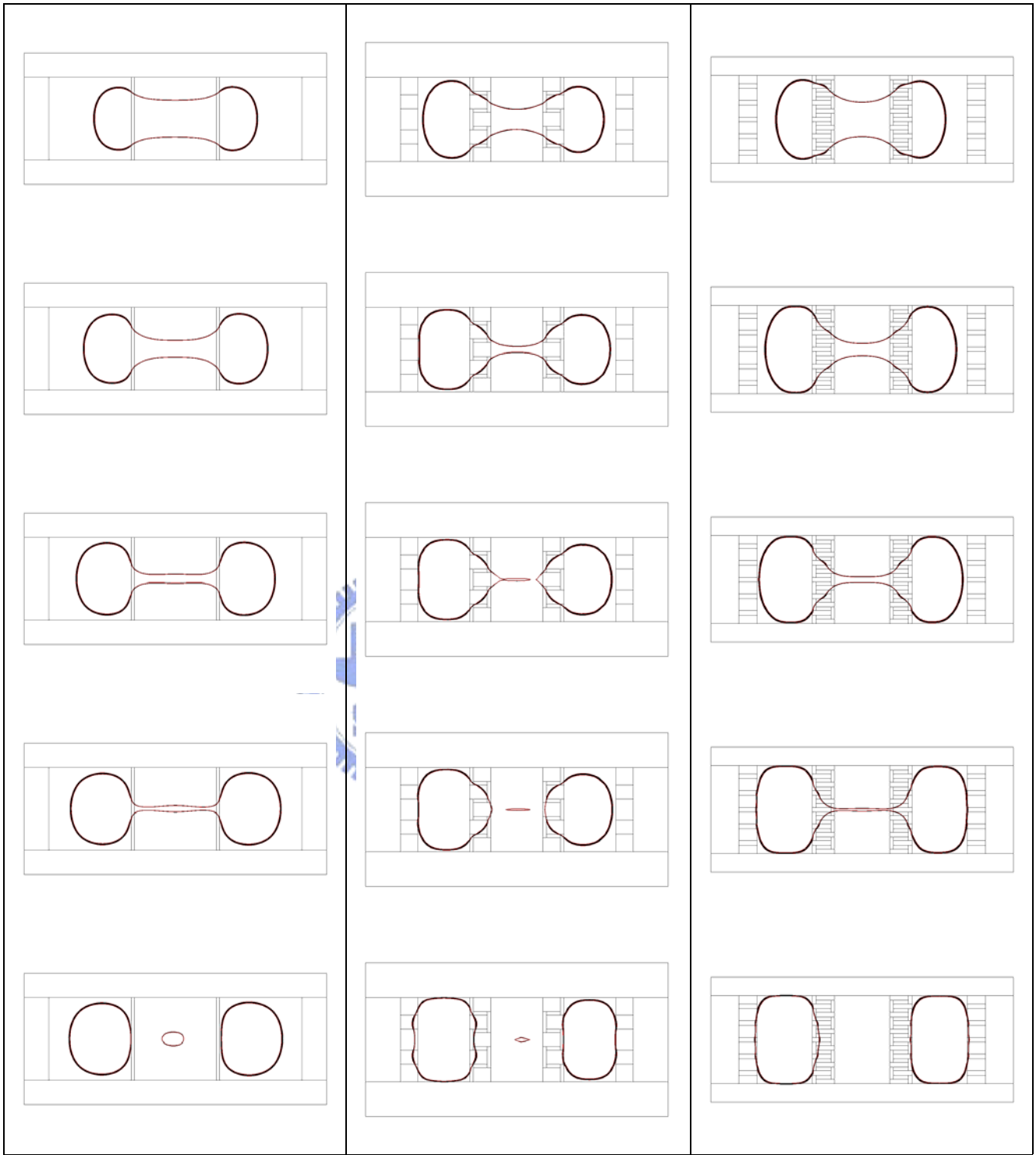

Electrode square 0.5mm X 0.5mm (case 16)	Electrode 232 0.5mm X 0.48mm (case 05)	Electrode 565 0.5mm X 0.475mm (case 14)

Fig. 4-12 Simulations of cutting (continue with Fig. 4-2)

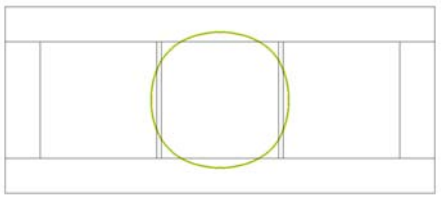

step 1

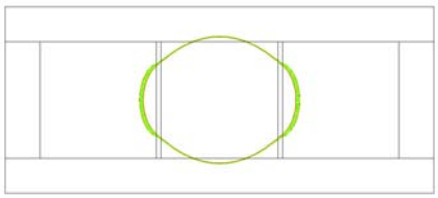

step 2

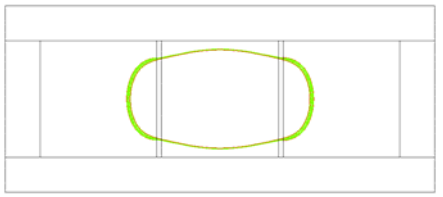

step 3

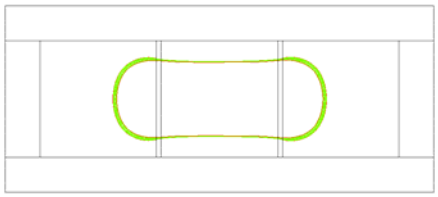

step 4

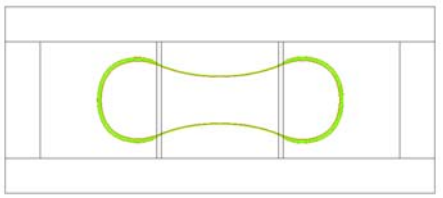

step 5

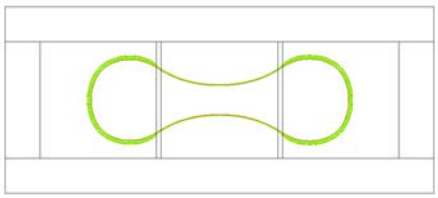

step 6

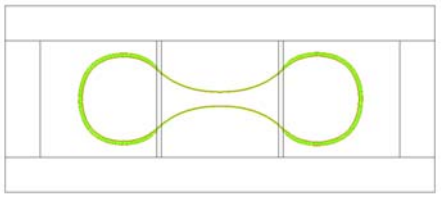

step 7

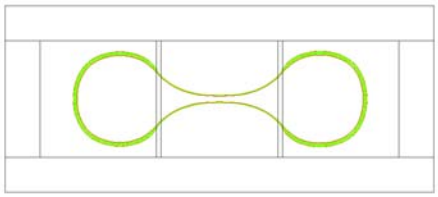

step 8

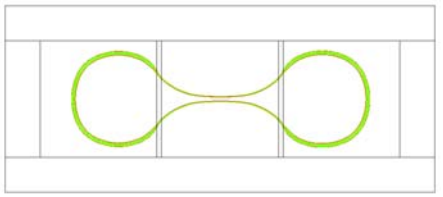

step 9

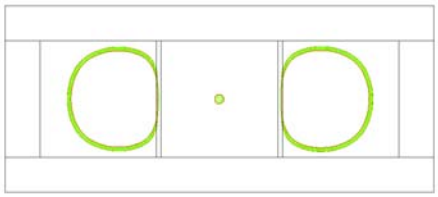

step10

Fig. 4-13 Simulations of cutting for droplet beginning position in middle electrode (channel hright 70 μm)

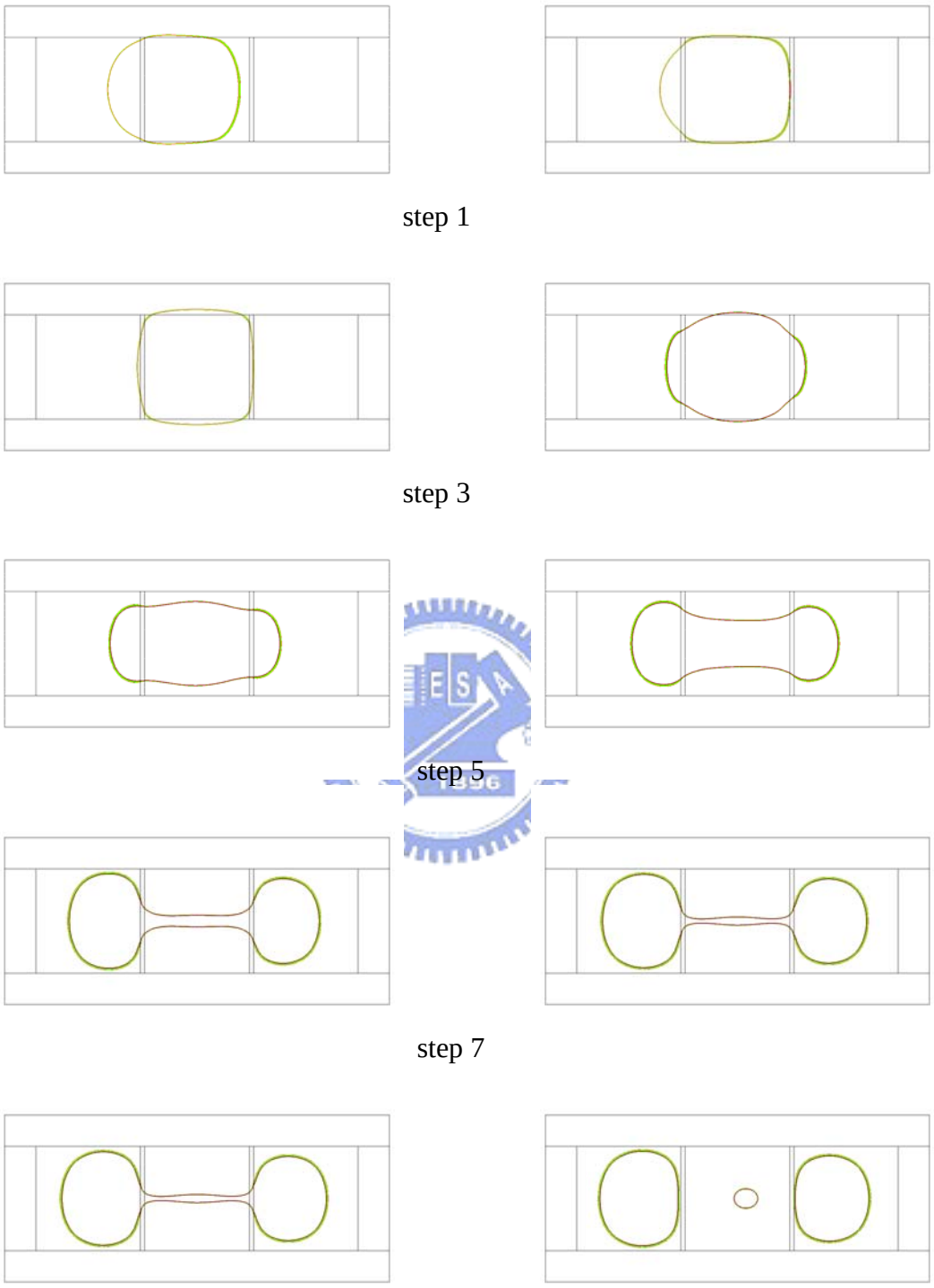

Fig. 4-14 Simulations of cutting for droplet moving from left to middle electrode (channel hright 70 μm)

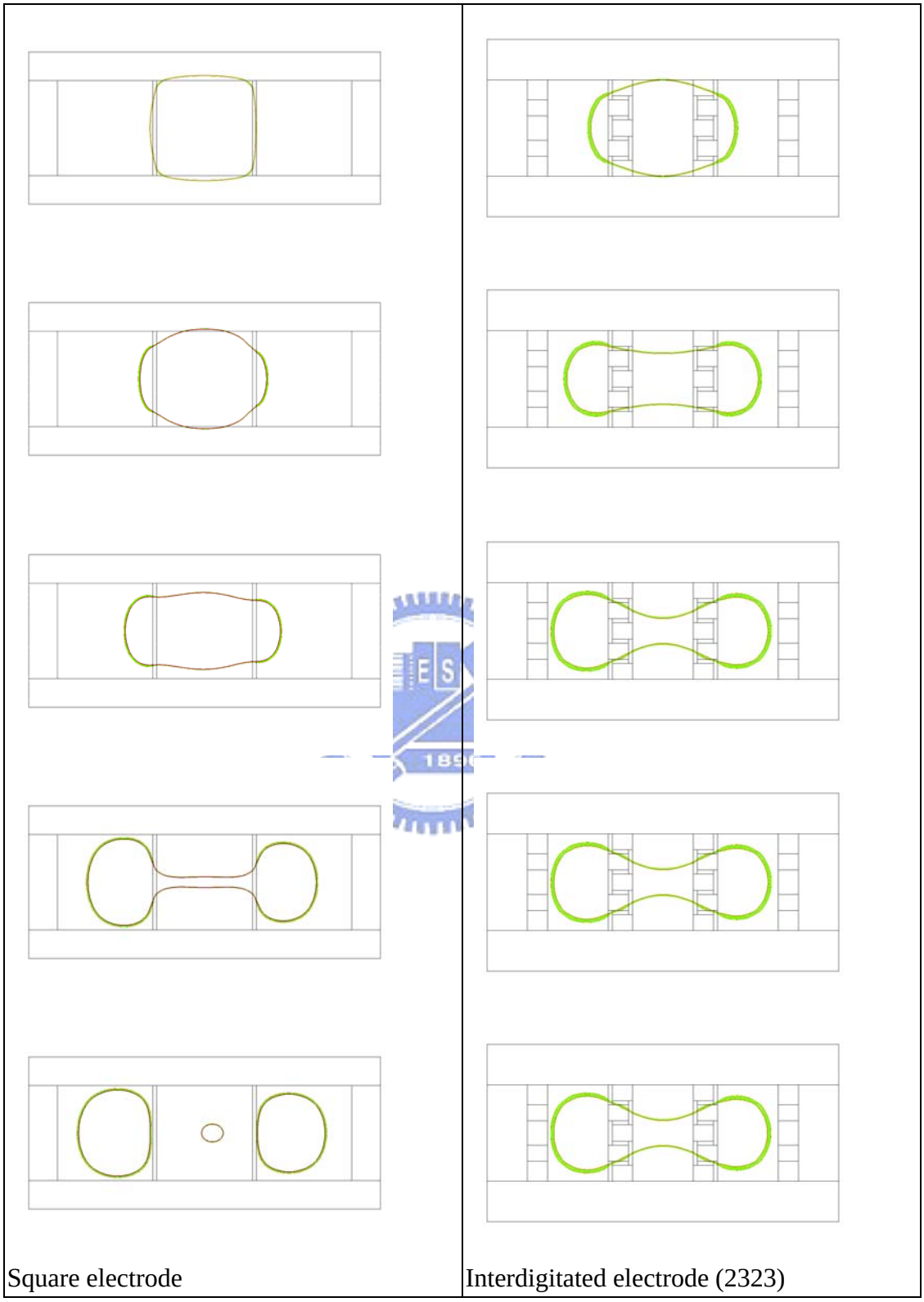

Fig. 4-15 Comparison of cutting for interdigitated electrode and square electrode at channel height 70 μm

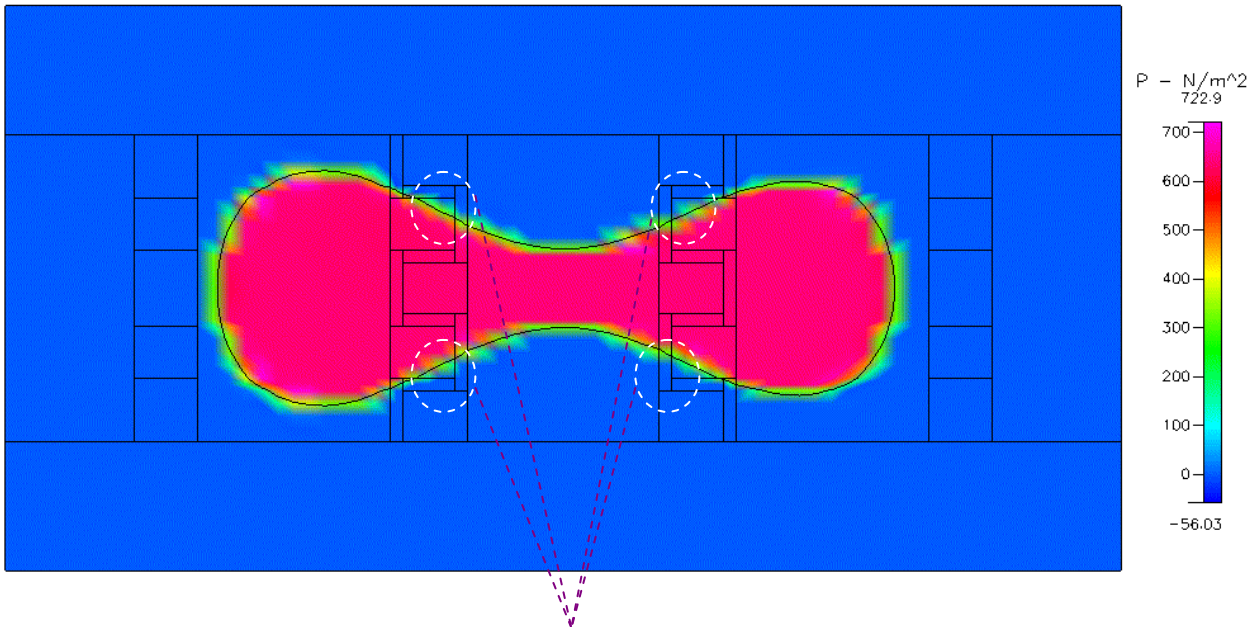

Fig. 4-16 Pressure distribution of interdigitated electrode (232) at channel height 70 μm

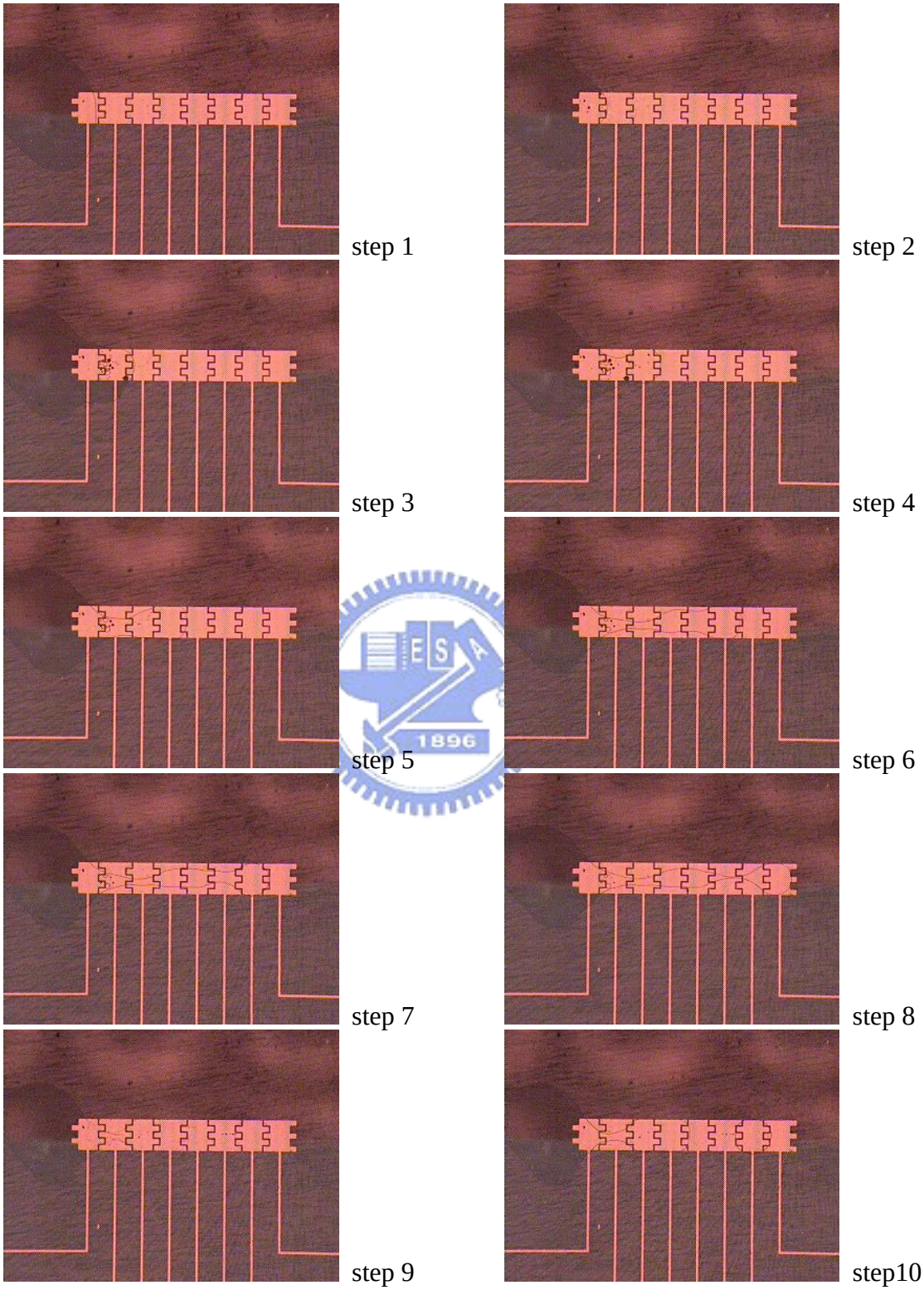

Fig. 4-17 Photos of creating (interdigitated electrode 2323)

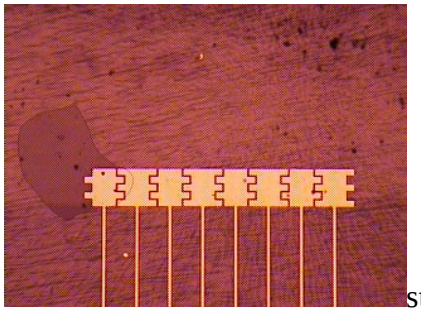
step 1
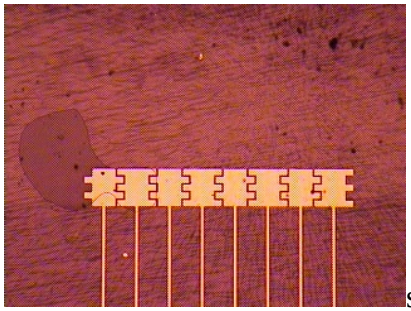
step 2
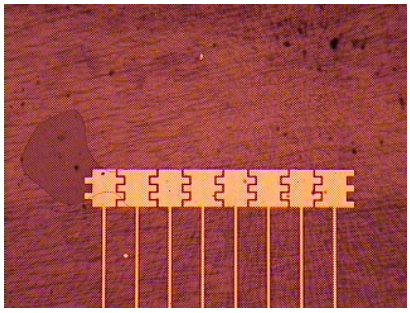
step 3
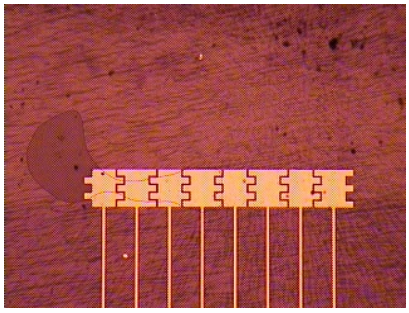
step 4
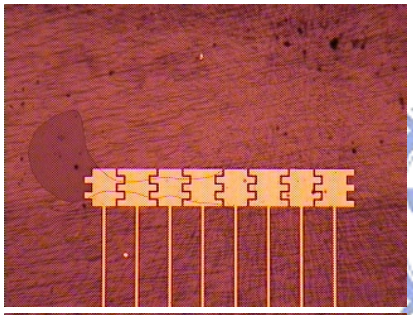
step 5
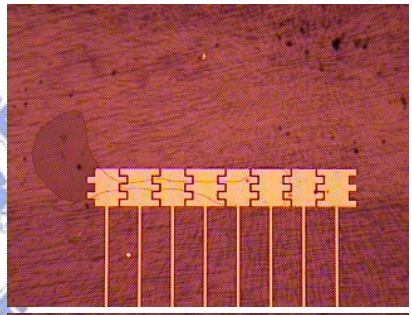
step 6
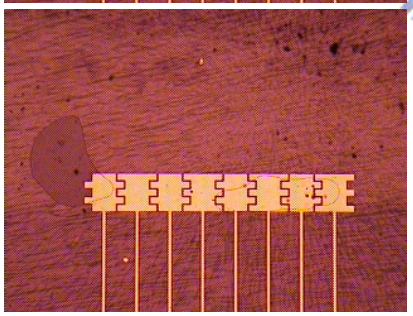
step 7
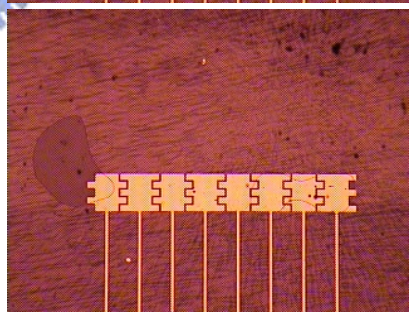
step 8
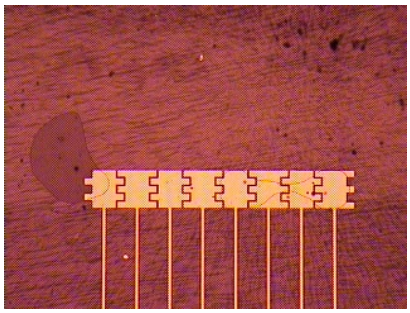
step 9
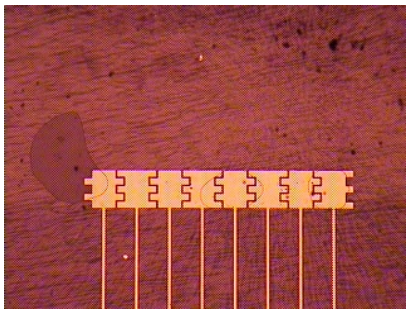
step 10

Fig. 4-18 Photos of creating (interdigitated electrode 2323)

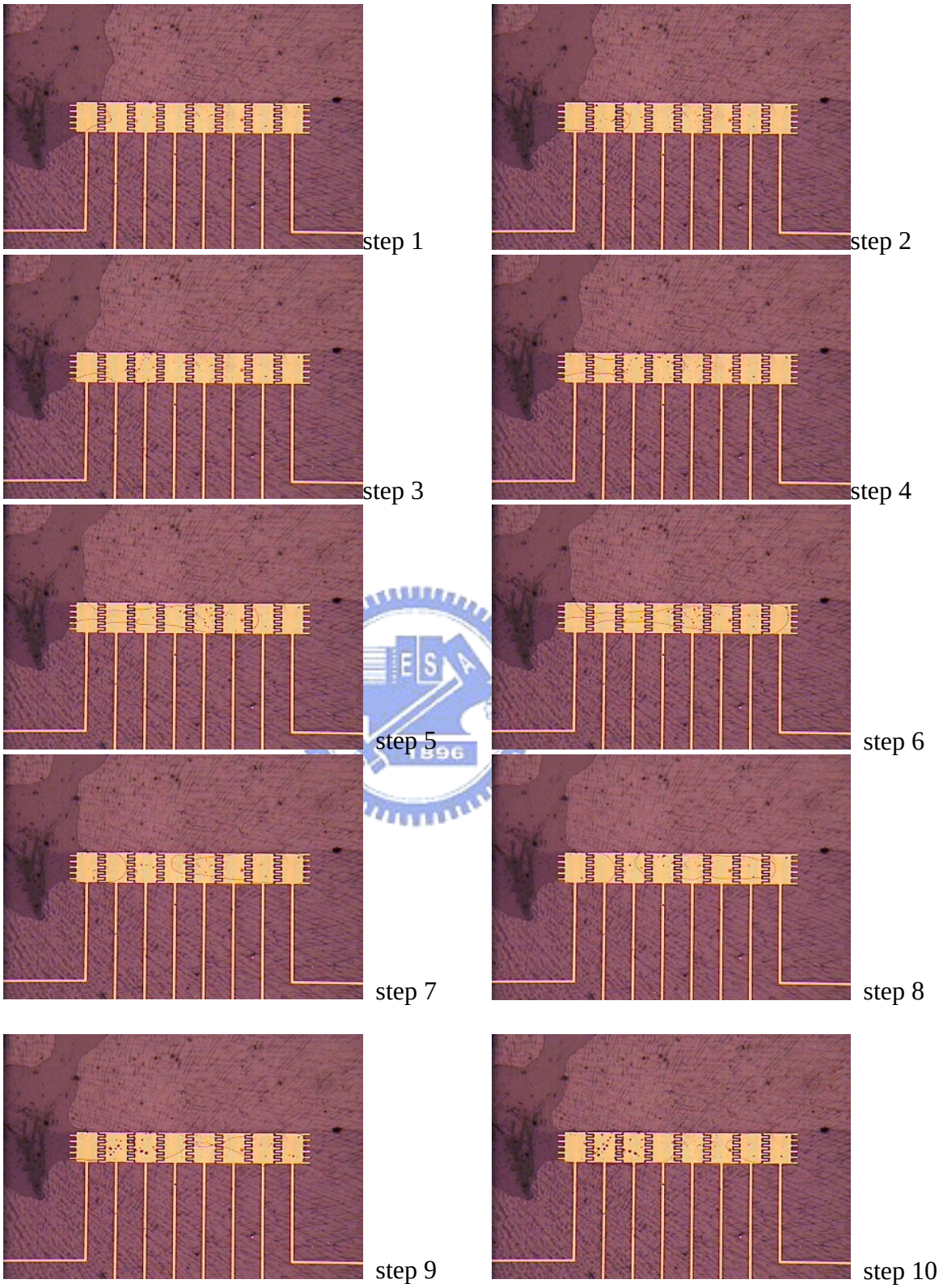

Fig. 4-19 Photos of creating (interdigitated electrode 5656)

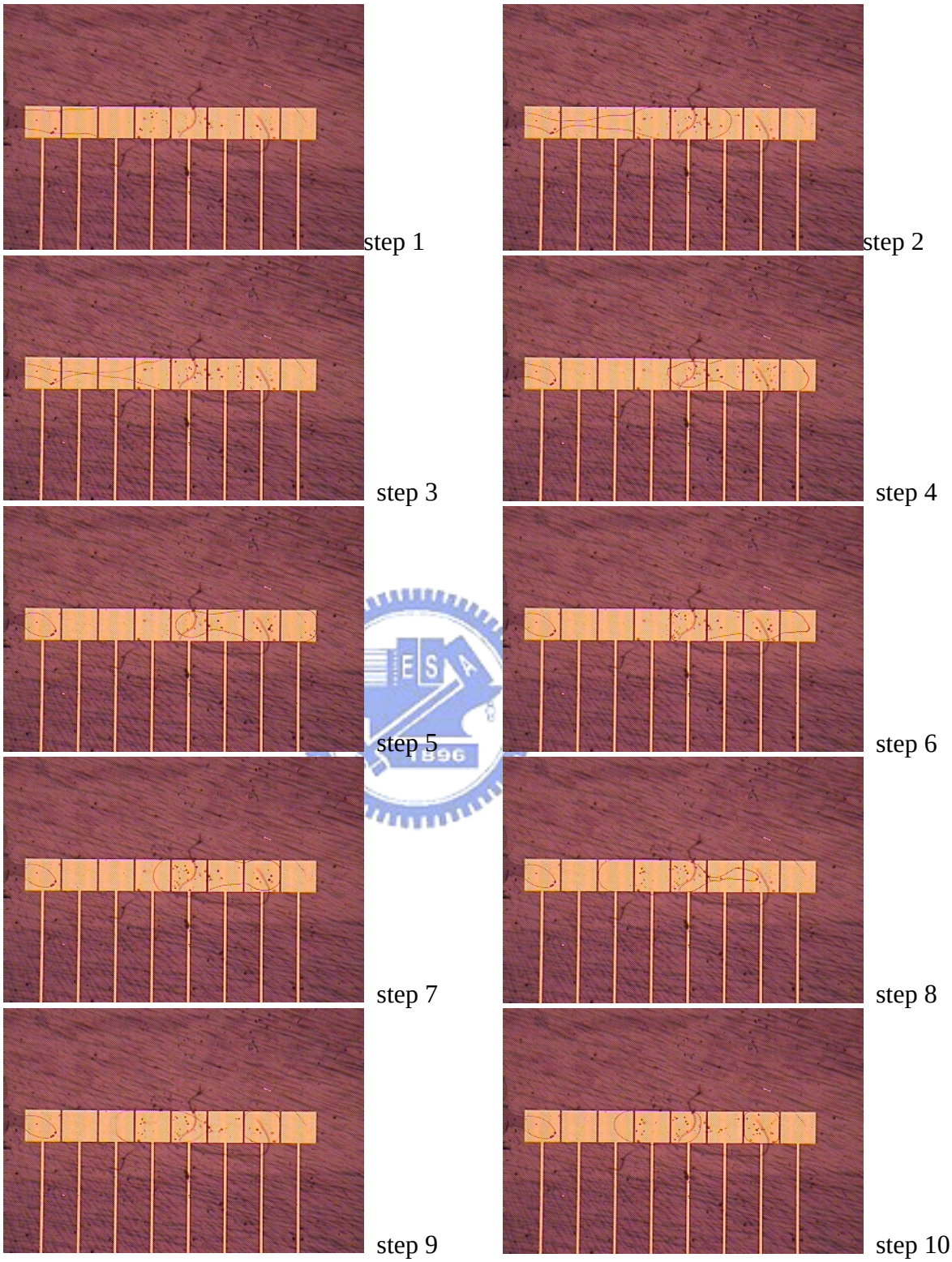

Fig. 4-20 Photos of creating (square electrode)

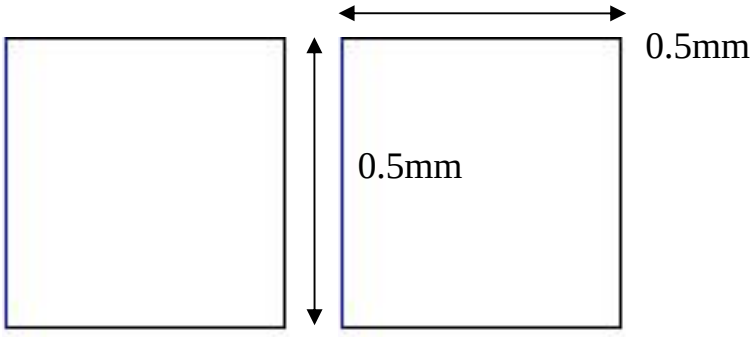

Fig. 4-21 square electrodes

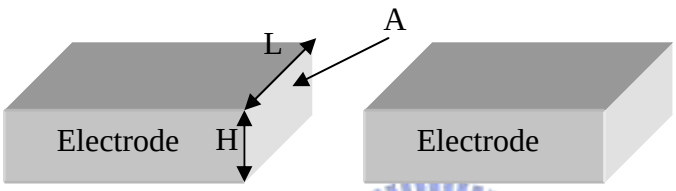

Fig. 4-22 Electrode-Electrode capacitor

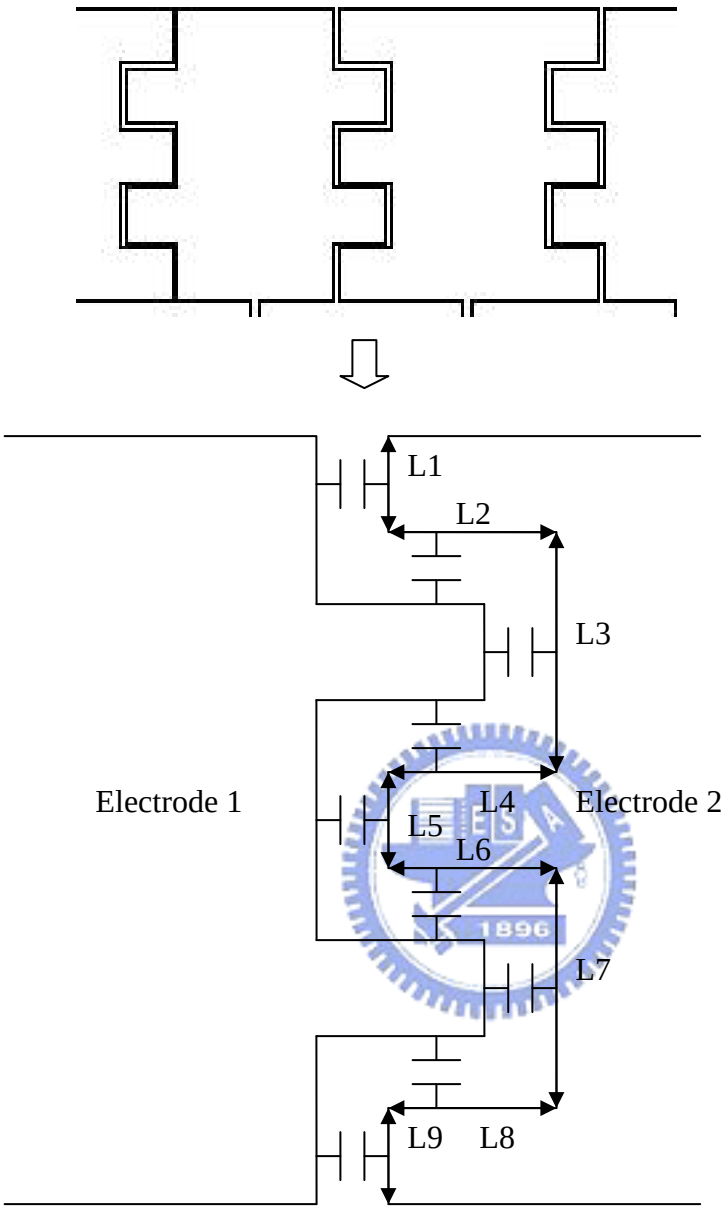

Fig. 4-23 the total capacitor of interdigitated electrodes

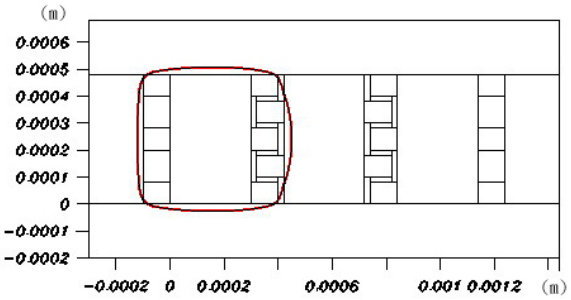

t=0~0.033 s

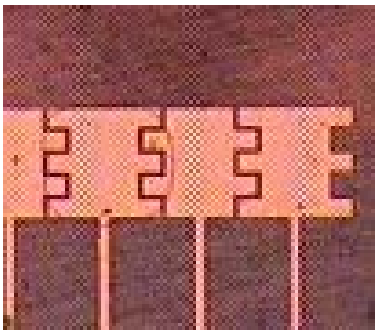

t=0~0.033 s

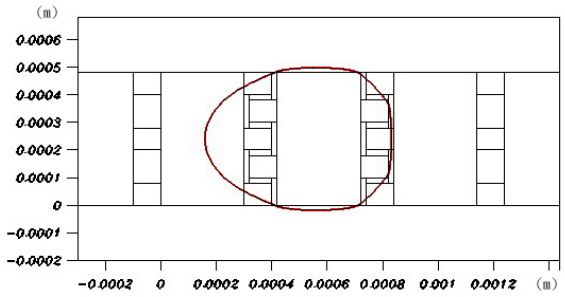

t=0.033~0.066 s

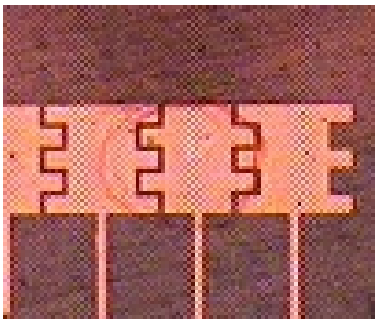

t=0.033~0.066 s

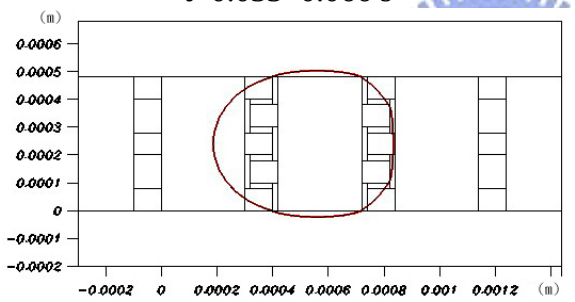

t=0.066~0.099 s

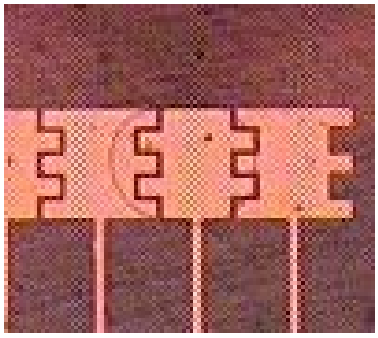

t=0.066~0.099 s

Fig. 4-24 Comparison between simulation flames and experimental photos (interdigitated electrode 2323, channel height 20 μm)

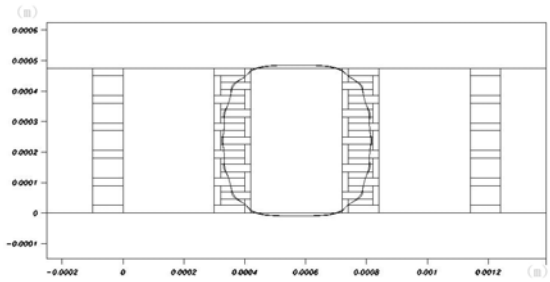

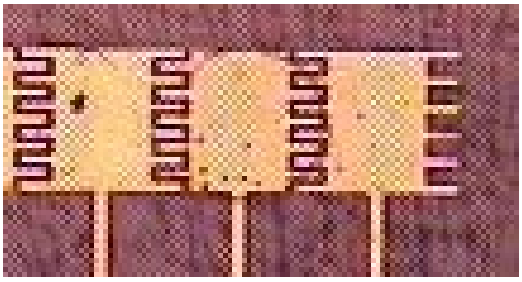

t=0~0.033 s

t=0~0.033 s

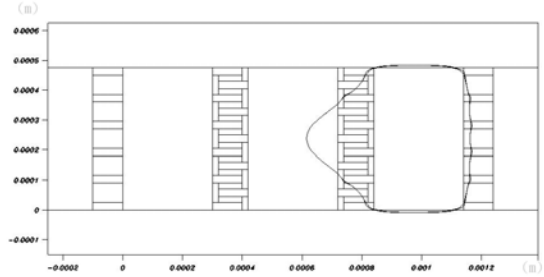

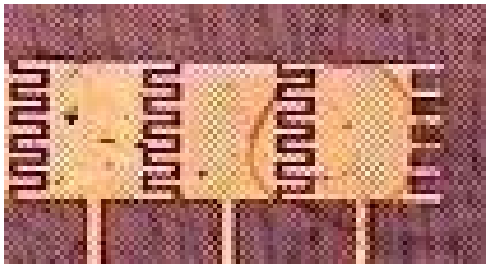

t=0.033~0.066 s

t=0.033~0.066 s

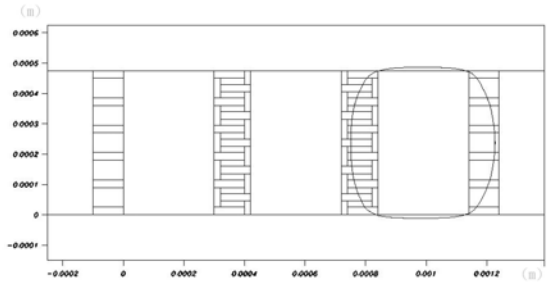

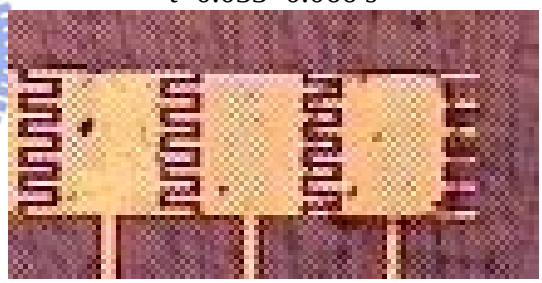

t=0.066~0.099 s

t=0.066~0.099 s

Fig. 4-25 Comparison between simulation flames and experimental photos (interdigitated electrode 5656)

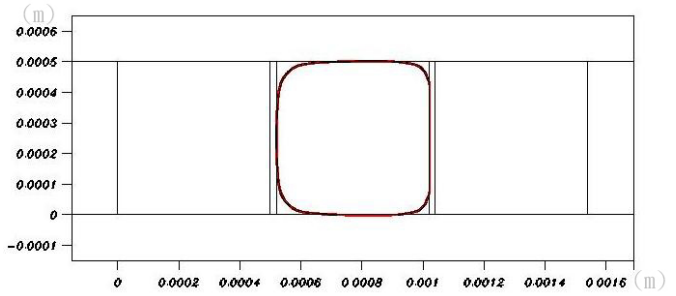

t=0~0.033 s

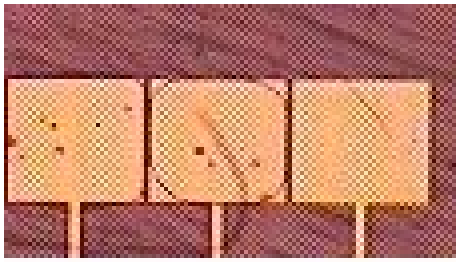

t=0~0.033 s

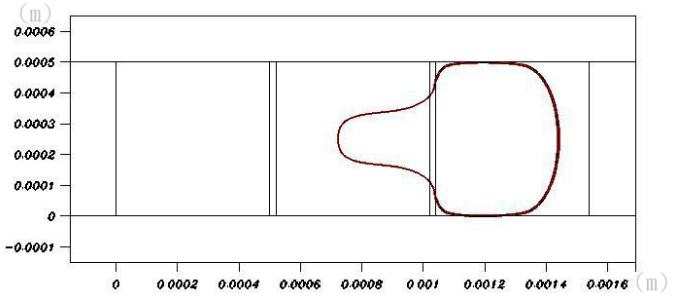

t=0.033~0.066 s

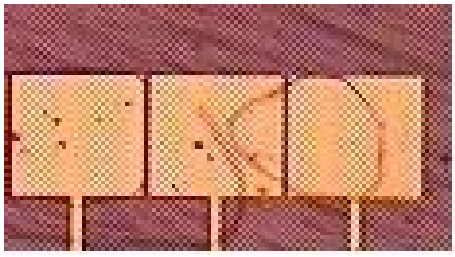

t=0.033~0.066 s

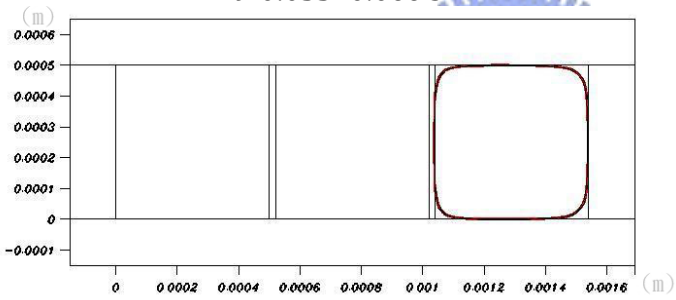

t=0.066~0.099 s

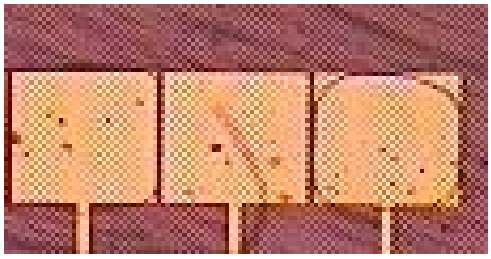

t=0.066~0.099 s

Fig. 4-26 Comparison between simulation flames and experimental photos (square electrode)

CHAPTER 5

Conclusions and Future works

5.1 Conclusions

In this study, the square electrode which the length of electrode $2mm$, channel gap $70\mu m$,applied voltage 40V and volume of droplet $0.3\mu l$,is done firstly. Then based on the experimental results above, the parameters of simulation are found out. However, according to numerical results, we design interdigitated electrodes to create nano-liter. There are 16 cases which are presented in Table 4-3 and Table 4-6, and a comparison is made between them. Based on results of simulation, the design of interdigitated electrodes (2323) can cause larger pressure difference to move the droplet. So we make the devices of square electrodes (0.5mm x 0.5mm), interdigitated electrodes (2323) (0.48mm x 0.5mm) and interdigitated electrodes (5656), to prove the results of simulation. However, the interdigitated electrode (2323) has the largest velocity, 13.219 mm/s in simulation and 11.36 mm/s in experiment for droplet moving. It manifests the designs of interdigitated electrodes are significance.

From the anticipation of CFD-RC+ and results of experiment, it concludes that the more area of electrode is touched by droplet, the larger pressure difference is generated. Therefore, in the experiment, it considers a way to design an electrode that can make the surface curve of droplet to occupy larger area of adjacent electrode, such as interdigitated electrode (2323). Besides, the phenomenon of increasing pressure difference as decreasing channel height is verified by numerical results. From Table 4-3 and Table 4-6, for all

cases, design of interdigitated electrode 2323 (W=80μm) can generate the largest pressure difference at the same channel height. In the experiments, to create a nano-liter droplet for interdigitated electrodes 2323 (W=80μm) is easier than interdigitated electrodes 5656 (W=25μm) and square electrodes.

Because the design of interdigitated electrodes (2323) has larger pressure difference which can move and cut droplet easily. However, the volume of creating droplet is from 2.9nl to 8.5nl in experiments. Therefore, for droplet moving at channel height 20μm, the experimental photos are fit by numerical frames, as shown Fig 4-24, 4-25 and 4-26. It is confirmed that the results of simulation have the relative accuracy.

Finally, we also make a table 5-1 to discuss which electrodes is the best to create nano-liter. According to the experimental operation and numerical simulation, the interdigitated electrode 2323 (W=80μm) is more proper design to create a nona-liter droplet surrounding air.

Table 5-1 Comparison of three different electrodes

	interdigitated electrode (2323)	interdigitated electrode (5656)	Square electrode
Pressure difference for moving, cutting and creating	1	2	3
hydrolysis	2	1	3
Channel height (μm)	20		
Applied voltage (V)	100 AC (offset 50V) 80 AC (offset 40V)		
Electrode shape	Symmetry		
Volume of creating droplet (nl)	2.9~8.5		

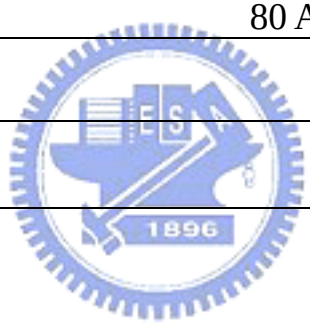

5.2 Future works

There are some improvements for the experiments, such as adding a reservoir, droplet surrounding silicon oil, 2-D control electrodes arrays, designing a new electrode to abbreviate creating process and so on. Because the model of EWOD simulation is established, we can invent more novel electrode to forecast and to create pico-liter droplet by commercial software CFD-ACE+. Otherwise, it maybe simulate other solutions or droplet in different environments, such as organic solvents, isotonic solutions, blood, DI water in silicon oil, particles in droplet and so on. For experiments, the nano-liter droplet is created, but the liquid is DI water. In future work, the other liquids, such as isotonic solutions, created by EWOD devices, can be employed in DNA-chip, protein-chip or other microsystems. Nevertheless, there are many subjects about EWOD can be discussed furthermore.

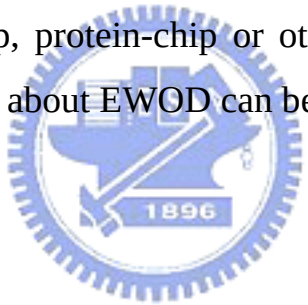

References

1. Shih-Kang Fan, “Digital Microfluidics Cross-Reference EWOD Actuation: Principle, Device and System”, Unversity of California Los Angeles, Degree doctor of philosophy, 2003.
2. Shih-Chyn Lin, “Study of WEOD-based Actuation for Digital Microfluidic System”, National Central University, Degree of master, June 2004.
3. T.A. Mcmahon and J.T. Bonner, On Size and Life, Scuentific American Books, New York, 1983.
4. Lippman G, Relation Entre Les , “Phenomens electriues et capillaries”, Ann. Chim. Phys, 1875: 494-59.
5. Michael G. Pollacka and Richard B. Fairb, “ Electrowetting-based actuation of liquid droplets for microfluidic applications”, Applied Physical Letters Volume 77, Number 11, 2000.
6. Junghoon Lee, Hyejin Moon, Jesse Fowler, Thomas Schoellhammer and Chang-Jin Kim, “Electrowetting and electrowetting-on-dielectric for microscal liquid handling”, Sensors and Actuators A, 95, pp. 259-268, 2002.
7. Neil Fortner and Benjamin Shapiro, “Equilibrium and Dynamic Behavior of Micro Flows Under Electrically Induced Surface Tension Actuation Forces”, Aerospace Engineering, University of Maryland
8. H. J. J. Verheijen, “Reversible Electrowetting and Trapping of Charge: Model and Experiments,” Langmuir, 15, pp. 6616-6620, 1999.
9. Sung Kwon Cho, Hyejin Moon and Chang-Jin Kim, “Creating, Transporting, Cutting, and Merging Liquid Droplets by

Electro-wetting-Based Actuation for Digital Microfluidic Circuits", Journal of Micro-electromechanical Systems, Vol. 12, NO.1. Feb 2003.

10. Sung Kwon Cho and Chang-Jin Kim, "Particle Separation and Concentration Control for Digital Microfluidic Systems", pp. 686–689, Kyoto, Japan, Jan 2003.
11. Vijay Srinivasan, Vamsee K.Pamula and Richard B. Fair, "Droplet-based Microfluidic Lab-on-a-chip for Glucose Detection", Analytica Chimica Acta, 507, pp.145-150, 2004.
12. H. Ren, R.B. Fair and M.G. Pollack, " Automated on-chip droplet dispensing with volume control by electro-wetting actuation and capacitance metering", Sensors and Actuators, B 98, pp.319–327, 2004.
13. Debalina Chatterjee, Boonta Hetayothin, Aaron R. Wheeler, Daniel J. King and Robin L. Garrell, "Droplet-based microfluidics with nonaqueous solvents and solutions", The Royal Society of Chemistry 2006 Lab Chip, 6, pp. 199–206, 2006.
14. Yi-Liang Lin, "Creating Nano-Liter Droplets Based on Digital Microfluidic System", National Cheng Kung University, Degree of master, June 2006
15. Guo-Hua Lin, "Simulation of Creating Nano-Liter Droplets Based on Digital Microfluidic Device", National Chiao Tung University, Degree of master, June 2006.
16. Frank Gindele, Frank Gaul and Thomas Kolling, "Optical systems based on electrowetting", MEMS MOEMS and Micromachining, Proc. Of SPIE Vol. 5455, 2004.
17. S. K. Cho, H. Moon, J. Fowler, S.-K. Fan and C.-J. Kim, "Splitting a Liquid Droplet for Electrowetting-Based Microfluidics", Int. Mechanical Engineering Congress and Exposition, IMECE2001/MEMS-2383, New

York, Nov. 2001

18. Van Doormaal, J. P. and Raithby, G. D., “Enhancements of The SIMPLE Method for Predicting Incompressible Fluid Flows”, Numerical Heat Transfer, Vol. 7, Numerical Heat Transfer, pp.147-163, Apr.-June. 1984.
19. Kothe, D. B., Rider, W. J., Mosso, S. J., Brock, J. S. and Hochstein, J. I., “Volume Tracking of Interfaces Having Surface Tension in Two and Three Dimensions”, Aerospace Sciences Meeting and Exhibit, 34th, 1996.
20. Brackbill, J. U., Kothe, D. B. and Zemach, C. “A Continuum Method for Modeling Surface Tension”, Journal Computational Physics, Vol. 100, pp. 335-354, Issue 2, 1998.
21. C. W. Hirt and B. D. Nichols, "Volume of Fluid (VOF) Method for the Dynamics of Free Boundaries", Journal of Computational Physics, Vol. 39, pp.201-225, 1981.
22. W. J. Rider, D. B. Kothe, S. J. Mosso, J. H. Cerrutti and J. I. Hochstein, "Accurate solution algorithms for incompressible multiphase fluid flows," AIAA Paper, 95-0699, 1995.
23. Noh, W. F. and Woodward, P. R., "SLIC Simple Line Interface Method)." In A.I. van de Vooren and P.J. Zandbergen, editors, Lecture Notes in Physics 59, pp. 330-340 1976.
24. D.L. Youngs, Num. Met., “Fluid Dyn”, Academic Press, New York, 1982, pp. 273–285.
25. W.J. Rider, D.B. Kothe, J. ,”Comput. Phys”, 141 (1998) 112–152.
26. D. Gueyffier, J. Li, A. Nadim, R. Scardovelli, S. Zaleski, J. ,“Comput.Phys”, 152 (1999) 423–456.
27. Van Doormaal, J. P., and Raithby, G. D., “Enhancements of The SIMPLE Method for Predicting Incompressible Fluid Flows”, Numerical Heat Transfer, Vol. 7, No. Heat Transfer, 1984, pp. 147- 163.